ISTANBUL TECHNICAL UNIVERSITY ★ GRADUATE SCHOOL

APPLICATION OF MATRIX PRODUCT STATES FOR FEW PHOTON DYNAMICS AND QUANTUM WALKS IN REDUCED DIMENSIONS

Ph.D. THESIS

Burçin DANACI

Department of Physics Engineering

Physic Engineering Programme

DECEMBER 2021

ISTANBUL TECHNICAL UNIVERSITY ★ GRADUATE SCHOOL

APPLICATION OF MATRIX PRODUCT STATES FOR FEW PHOTON DYNAMICS AND QUANTUM WALKS IN REDUCED DIMENSIONS

Ph.D. THESIS

Burçin DANACI
(509142102)

Department of Physics Engineering

Physic Engineering Programme

Thesis Advisor: Assoc. Prof. Ahmet Levent SUBAŞI

DECEMBER 2021

İSTANBUL TEKNİK ÜNİVERSİTESİ ★ LİSANSÜSTÜ EĞİTİM ENSTİTÜSÜ

MATRİS ÇARPIM DURUMLARI FORMALİZMİNİN DÜŞÜK BOYUTLARDA AZ SAYIDAKİ FOTONLARIN DİNAMİĞİNE VE KUANTUM YÜRÜYÜŞLERİNE UYGULANMASI

DOKTORA TEZİ

Burçin DANACI
(509142102)

Fizik Mühendisliği Anabilim Dalı

Fizik Mühendisliği Programı

Tez Danışmanı: Assoc. Prof. Ahmet Levent SUBAŞI

ARALIK 2021

Burçin DANACI, a Ph.D. student of ITU Graduate School with ID number 509142102, successfully defended the thesis entitled "APPLICATION OF MATRIX PRODUCT STATES FOR FEW PHOTON DYNAMICS AND QUANTUM WALKS IN REDUCED DIMENSIONS", which she prepared after fulfilling the requirements specified in the associated legislations, before the jury whose signatures are below.

Thesis Advisor :	**Assoc. Prof. Ahmet Levent SUBAŞI** Istanbul Technical University	.....
Jury Members :	**Prof. Ali YILDIZ** Istanbul Technical University	.....
	Assoc. Prof. Rıfat Onur UMUCALILAR Mimar Sinan Fine Arts University	.....
	Dr. Juan José GARCIA-RIPOLL Spanish National Research Council	.....
	Assoc. Prof. Cem Özgür SERVANTIE Istanbul Technical University	.....

Date of Submission : 22 October 2021
Date of Defense : 2 December 2021

FOREWORD

I would like to thank my thesis advisor Ahmet Levent SUBAŞI for his guidance and support. I would also like to thank Juan José GARCIA-RIPOLL, who has been very helpful to me during my stay in Madrid and the members of his group "QUINFOG" in CSIC. It was a great opportunity for me to work in such a stimulating environment.

I can't thank enough to Ayşe ERZAN, not only for her teaching and guidance in physics, but also being a great friend and mentor. Knowing her is a great privilege for me, and I feel lucky to have someone like her to look up to.

I am grateful to my friends in İTU physics department, who have been there for me, whenever I needed them. I will miss every moment I shared with them. Maybe except for our never-ending asistant meetings.

I would like to thank the Scientific and Technological Research Council of Turkey (TUBITAK) for the financial support they provided during my stay in Madrid as a visiting researcher in CSIC. I would also like to acknowledge the financial support of Istanbul Technical University Scientific Research Projects Department (ITU BAP No. 40881).

Last but not least, I thank heartfully to my family for their endless love and support.

December 2021

Burçin DANACI
(M.Sc. Physics Engineering)

TABLE OF CONTENTS

Page

ABBREVIATIONS

MPS	**:** Matrix Product States
TLS	**:** Two level system
TEBD	**:** Time evolving block decimation
SVD	**:** Singular value decomposition
USC	**:** Ultra-strong coupling
RWA	**:** Rotating wave approximation
ABC	**:** Absorbing boundary condition
PR	**:** Participation ratio
CPTP	**:** Completely positive trace preserving
BLP	**:** Breuer-Laine-Piilo
RHP	**:** Rivas-Huelga-Plenio
MBL	**:** Many-body localization
DFL	**:** Disorder-free localization
IPR	**:** Inverse participation ratio

SYMBOLS

Ψ	:	Wave function
ρ	:	Reduced density matrix
S	:	von Neumann entropy
$\mathcal{H}$	:	Hilbert space
ε	:	Computational error
$\hat{H}$	:	Hamiltonian
$\hat{W}$	:	Evolution operator
g	:	Interaction strength
ω	:	Frequency
J	:	Hopping parameter
γ	:	Absorption strength
$\hat{I}$	:	Identity operator
θ	:	coin angle
ϕ	:	Phase
$\Theta(x)$	:	Heaviside step function
$\mathcal{N}$	:	BLP measure of non-Markovianity
C	:	Concurrence
$\mathcal{I}$	:	RHP measure of non-Markovianity

LIST OF FIGURES

Page

APPLICATION OF MATRIX PRODUCT STATES FOR FEW PHOTON DYNAMICS AND QUANTUM WALKS IN REDUCED DIMENSIONS

SUMMARY

Numerical simulations of low-dimensional quantum many-body systems have been a very active field in recent years. New techniques have enabled experimental realization of these systems and have shed light to both theoretical and technological developments. However, the numerical simulations of these systems have been challenging due to the exponential growth of the Hilbert space with the system size. In addition, quantum correlations such as entanglement play an important role in many-body systems. Therefore approximate methods have been developed. One of the methods to simulate such quantum systems in one-dimension is the Matrix Product States (MPS) Formalism.

In this thesis, we concentrate on the application of MPS to quantum optical systems and quantum walks. For this purpose, we have developed a pedagogical numerical library which consists of functions responsible for efficient representation of the wave function and its time evolution. We have tested the efficiency of these functions for different parameters.

The quantum optical system we consider is a one-dimensional coupled cavity array interacting with a two-level system. One of the techniques to simulate long time dynamics of a quantum many-body system in a computationally manageable grid is to impose absorbing boundary conditions. We have applied absorbing boundary conditions in the form of an imaginary potential and determined the optimum parameter intervals for efficient simulation. Another objective of this thesis is to examine the photon dynamics and the decay of the two-level system from its excited state for different interaction strengths. We have shown that in the strong interaction regime where rotating wave approximation (RWA) is applicable the results obtained from exact diagonalization and MPS simulations are in perfect agreement. For higher interaction strengths we have used polaron transformation to lower the effective interaction and applied RWA afterwards. We have discussed the differences between the results in terms of photon numbers and the excited-state population of the two-level system.

As part of this thesis we have studied two types of discrete-time quantum walks. Firstly, we have considered a quantum walk with a single phase impurity and investigated the effects of the bound states on its spatial localization and non-Markovianity properties. In Markovian systems there is irreversible flow of information from the system under consideration to its environment, whereas in non-Markovian systems some of this information flows back to the system. Our findings show that there is a strong relation between the localization and non-Markovianity in this model. Secondly, we turned our attention to a quantum walk coupled to a spin chain environment where there is a dynamical spin attached

to each site. Using our MPS algorithm, we have studied the relationship between the quasi-energy spectrum obtained from exact diagonalization of finite systems, dynamical localization, entanglement entropy and spin dynamics of this walk. We have observed that due to the extensive number of conserved quantities it possesses, this model is similar to the disorder-free localization models found in literature, where disorder is induced due to the interaction between the constituents of the system.

MATRİS ÇARPIM DURUMLARI FORMALİZMİNİN DÜŞÜK BOYUTLARDA AZ SAYIDAKİ FOTONLARIN DİNAMİĞİNE VE KUANTUM YÜRÜYÜŞLERİNE UYGULANMASI

ÖZET

Düşük boyutlu, çok parçacıklı kuantum sistemlerinin hesaplamalı benzetimleri son yıllarda son derece aktif olarak çalışılan bir alan haline gelmiştir. Bunun nedeni geliştirilen yeni teknikler sayesinde bu sistemlerin deneysel olarak üretilmesi ile birlikte hem teorik alanda hem de kuantum teknolojilerinde yeni gelişmelere ışık tutmasıdır. Ancak bu sistemlerin Hilbert uzayının boyutu serbestlik derecesi sayısı ile üstel olarak büyümektedir. Bu durum da hesaplamalı benzetimlerinin yapılmasını zorlaştırmaktadır. Bu nedenle yaklaşık yöntemler geliştirilmiştir. Bu yöntemler arasında bir boyutlu çok parçacıklı kuantum sistemlerinin benzetiminde en çok kullanılanlardan biri Matris Çarpım Durumları (Matrix Product States, MPS) Formalizmidir.

Bu tezde MPS Formalizmi kuantum optik sistemlerine ve kuantum yürüyüşlerine uygulanmıştır. Bu amaçla numerik bir kütüphane geliştirilerek bu kapsamda yazılan fonksiyonların farklı parametreler için doğruluğu ve verimliliği test edilmiştir. Bu fonksiyonlar kuantum dalga fonksiyonunun bilgisayardaki temsilinin ve zaman evriminin verimli bir şekilde benzetimini sağlamaktadır.

Kuantum optik sistemi olarak iki seviyeli bir kuantum sistemi ile etkileşen bir boyutlu bağlı kovuk zinciri incelenmiştir. Çok parçacıklı bir kuantum sisteminin uzun süreli dinamiğinin benzetiminin yapılması için geliştirilmiş tekniklerden biri soğurucu sınır koşullarının kullanılmasıdır. Çalışmamızda bu sınır koşulları iki seviyeli sistemden uzaklaştıkça üstel olarak azalan, $\gamma e^{-n/l}$ formunda imajiner bir potansiyel şeklinde uygulanmıştır. Burada γ soğurma kuvveti, l ise soğurma uzunluğudur. Bu parametrelerin farklı değerleri için soğurma bölgesinin dışındaki dalga fonksiyonundaki değişim incelenerek etkin bir benzetim için optimum değer aralıkları belirlenmiştir.

Bu tezin bir diğer amacı da farklı kuvvetlerde etkileşimler için foton dinamiğinin ve iki seviyeli sistemin uyarılmış durumundan taban durumuna bozunmasının araştırılmasıdır. İki seviyeli sistemle kovuk arasındaki etkileşim kuvveti g'nin kovukların dışındaki modlarla etkileşimlerin ihmal edilebilmesini sağlayacak kadar büyük olduğu, ancak foton frekansı ω'ya göre yeterince küçük olduğu ($g < 0.1\omega$) rejime güçlü etkileşim rejimi denmektedir. Güçlü etkileşim rejiminde dönen dalga yaklaşıklığını kullanarak Hamiltonyendeki uyarılma sayısını korumayan terimleri ihmal etmek ve problemi tam köşegenleştirme yöntemiyle çözmek mümkündür. Bu limitte tam köşegenleştirme yöntemi ile elde edilen sonuçlar MPS algoritması ile elde edilen sonuçlarla karşılaştırıldığında her ikisinin de tam olarak örtüştüğü gözlemlenmiştir. Daha yüksek etkileşim kuvvetleri söz konusu olduğunda dönen dalga yaklaşıklığı geçerliliğini yitirir. Ancak orta ölçekli etkileşimlerde polaron dönüşümü yaparak efektif ektileşim kuvvetini düşürmek ve dönüşümden sonra elde edilen

bazda dönen dalga yaklaşıklığı kullanmak mümkündür. $0.1\omega < g < 0.2\omega$ aralığında yaptığımız benzetimler polaron dönüşümü kullanılarak elde edilen sonuçların MPS algoritması ile elde edilen sonuçlarla büyük ölçüde tutarlı olduğunu göstermektedir. Daha yüksek etkileşim kuvvetleri içinse sonuçlar arasındaki farklılıklar artmaktadır.

Bu tezde araştırılan bir diğer kuantum sistemi kesikli zamanlı kuantum yürüyüşüdür. Bu model 1993 yılında klasik rastgele yürüyüşün kuantum karşılığı olarak önerilmiştir. Bir boyutlu klasik rastgele yürüyüşte yürüyüşçü her adımda p olasılığı ile bir yöne, $1-p$ olasılığı ile diğer yöne hareket eder. Kuantum yürüyüşünde ise konum uzayına ek olarak yürüyüşçünün gideceği yönü belirleyen, para durumu olarak niteleyebileceğimiz, iki boyutlu bir serbestlik derecesi bulunmaktadır. Her adımda para atışına karşılık gelen bir operatör para uzayına etkiyerek para durumunu süperpozisyon haline getirir. Sonrasında uygulanan başka bir operatör paranın durumuna bağlı olarak yürüyüşçüyü sağa ya da sola kaydırır. Bu operatör koşullu bir operatör olduğu için para ve konum uzaylarını dolaşık hale getirir. Klasik rastgele yürüyüşün en temel özellikleri konum uzayındaki olasılıkların Poisson dağılımına sahip olması ve yayılma hızının difüzyon şeklinde olmasıdır. Difüzyon yayılmada varyans zamanla doğru orantılı olarak artmaktadır. Kuantum yürüyüşünde ise konum uzayındaki dağılım başlangıç noktası etrafında düz olup zamanla sıfıra yaklaşır, olasılığın en yüksek olduğu noktalar uçlara yakındır ve zamanla sabit hızla yayılırlar. Bu nedenle yayılma balistiktir ve varyans zamanın karesiyle orantılı olarak artar. Kuantum yürüyüşünün klasik rastgele yürüyüşe göre daha hızlı yayılması onu arama algoritmaları açısından daha cazip kılmaktadır. Ancak düzensizlik bu yayılma hızını düşürebilir. Dinamik düzensizlik kuantum girişimlerini ortadan kaldırarak klasik rastgele yürüyüş ile aynılaşmasına ve difüzyon şeklinde yayılmaya sebep olurken statik düzensizlik yayılmanın tamamen durmasına ve yerelleşmeye yol açabilmektedir. Bu tezin amaçlarından biri düzensizliğin etkisini farklı yürüyüş modelleri üzerinde incelemektir.

Bu tez kapsamında iki farklı, kesikli zamanlı kuantum yürüyüşü incelenmiştir. İlki tek bir faz safsızlığı içeren kuantum yürüyüşüdür. Buna göre yürüyüşçü başlangıç noktasından her geçtiğinde ϕ kadar bir faz almaktadır. Bu yürüyüş için konum uzayındaki yerelleşme ile Markovyen olmama özelliği arasındaki ilişki araştırılmıştır. Markovyen sistemlerde incelenen sistemden çevreye tersinmez şekilde bilgi akışı bulunmaktadır. Markovyen olmayan sistemlerde ise bu bilginin bir kısmı sisteme geri akmaktadır. Kuantum yürüyüşünde para uzayı ilgilenilenilen sistem, konum uzayı ise çevre olarak düşünülmektedir. Bu özelliğin incelenmesi için BLP ve RHP ölçütleri kullanılmıştır. Fazın büyüklüğüne bağlı olarak kuazi-enerji spektrumundaki bağlı durumların sayısının ve yerelleşmesinin değiştiği ve bu niceliklerin dinamik yerelleşme üzerinde doğrudan etkisi olduğu gözlemlenmiştir. Bağlı durumların bu özelliklerinin ve simetrilerinin Markovyen olmama özelliği üzerinde de etkili olduğu BLP ve RHP ölçütleri aracılığıyla gösterilmiştir. Bu bulgular bu model için yerelleşme ve Markovyen olmama özelliği arasında güçlü bir ilişki olduğuna işaret etmektedir.

İncelenen ikinci kuantum yürüyüşü faz safsızlığı yerine yürüyüşün her noktasında dinamik bir spin bulunan yürüyüş modelidir. Yürüyüşçü, bir noktadan geçtiğinde bu noktadaki spin döndürülür ve spinin açısı kadar bir faz alır. Düğüm noktalarında veya kenarlarında yerel spinler bulunan ağ yapılarındaki kuantum yürüyüşlerine benzer şekilde bu modelde de yerel spinler para uzayına etkimemektedir. Hamiltonyen ve seçtiğimiz başlangıç durumu öteleme açısından değişmezdir, ancak

buna rağmen yürüyüşçü ile yerel spinler arasındaki faza bağlı etkileşimden dolayı yerelleşme meydana gelmektedir. Bu nedenden ötürü bu model literatürde daha önce çalışılmış, "düzensizlik bulunmayan" yerelleşme (disorder-free localization) modellerinin kesikli-zamanlı versiyonu olarak düşünülebilir. Bu modelin yaygın korunmuş niceliklere sahip olması evrim problemini statik düzensizlik yürüyüşüne indirgemektedir. Seçtiğimiz başlangıç durumu bütün olası spin düzensizliği konfigürasyonlarının süperpozisyonu olduğundan yürüyüşçünün konum uzayındaki olasık dağılımı bütün olası spin konfigürasyonları üzerinden ortalama alarak elde edilebilmektedir.

İncelediğimiz ikinci kuantum yürüyüşü modelinde fazın büyüklüğüne bağlı olarak iki farklı yerelleşme rejimi gözlemlenmiştir. Faz yeterince küçük olduğunda zayıf etkileşim altındaki üç-boyutlu Anderson yerelleşmesi ve çok-parçacık yerelleşmesi modellerinde olduğu gibi, yerelleşmenin en fazla olduğu durumların spektrumun band kenarlarının yakınlarında yoğun olarak bulunduğu gözlemlenmiştir. Bunun sonucunda çalıştığımız orta-ölçekli zaman evrimi sonucunda yürüyüşçü başlangıç noktası etrafında kısmen yerelleşmektedir. Faz büyüdükçe band aralığı daralır ve faz yaklaşık olarak $\pi/4$ değerini aldığında band aralığı tamamen kapanır. Fazın daha büyük değerleri için yürüyüşçünün tamamen yerelleştiği ve yerelleşme uzunluğunun örgü aralığı ile aynı mertebede olduğu gözlemlenmiştir.

Spin dinamiğinin ve spin zincirinin farklı bölmeleri arasındaki dolanık entropisinin hesaplanması için MPS algoritması kullanılmıştır. Elde edilen sonuçlar dolanıklık entropisindeki zamana bağlı artışın fazın büyüklüğü ile ilişkili olduğunu göstermektedir. Orta ölçekli zaman aralığında yapılan benzetimlerde küçük fazlar için yürüyüşçünün kısmi yerelleşmesinin sonucunda dolanıklığın yayılım davranışının kenarlara doğru lineer, başlangıç noktası etrafında ise lineerden daha yavaş olmak üzere iki fonksiyonun toplamı şeklinde olduğu görülmektedir. Faz açısı büyüdükçe lineer yayılım daha fazla baskılanır ve lineerden daha yavaş olan yayılım baskın hale gelir. Dolanıklık entropisinin yayılımının bu şekilde baskılanması daha önce çalışılmış bazı düzensizlik bulunmayan yerelleşme ve çok-parçacık yerelleşmesi modelleriyle benzerlik göstermektedir.

1. INTRODUCTION

With the improving technologies, it has become possible to control and manipulate quantum systems at the level of single particle. These improvements paved the way for the development of new quantum devices and raised interest in theoretical and experimental research in related fields, such as quantum optics, quantum information and quantum computation. Experimental techniques developed in the last decades allow us to explore quantum many-body systems and the new physical regimes they exhibit [1].

One of the main challenges in the simulations of quantum many-body systems is the exponential growth of the Hilbert space with increasing system size. Therefore, efficient and approximate methods are needed in the treatment of these problems. Some of the most widely used algorithms in the simulations of quantum many-body problems are based on tensor networks [2, 3]. The efficiency of tensor networks relies on the fact that low-energy states of one-dimensional physical systems with short-range interactions generally have low entanglement [3, 4]. Hence, they can be applied to a wide range of physical systems. In one-dimension, one of the most commonly used tensor network methods is the Matrix Product States (MPS) formalism [2, 3, 5–10].

Another challenge encountered both in numerical and experimental studies is the environmental effects. In realistic quantum setups, the interactions between the system of interest and its surrounding environment are inevitable. These interactions destroy some of the quantum properties, yielding decoherence of the principal system. With the improvements in quantum technologies and increasing need of quantum setups, the theory of open systems [11] has become of great interest. Main motivation of these studies is to control and manipulate environmental effects in quantum setups. The developing experimental techniques has made it possible to construct elaborately structured environments, such as optical lattices with trapped ions or cold atoms [12–17]. These setups have made it possible for us to observe memory effects such as non-Markovianity and to study different types of localization. The simplest

environment can be thought as a bosonic bath, which yields a Markovian evolution in most cases, where there is a continuous flow of information from the principal system to its environment. Thanks to the developing experimental techniques it has become possible to realize more elaborate interactions with structured environments. These setups enable us to observe memory effects such as non-Markovianity, where some of the information flows back from the environment to the principal system. Another possible outcome of a structured environment is the dynamical localization of the wave function. Localization may be useful for secured storage of quantum memory [18] and in search algorithms such as detecting impurities on a grid [19].

One of the most commonly used models describing interactions between a principal system and its environment is the spin-boson model [11, 20, 21]. Light-matter interactions can also be described by this model. Here, the matter is considered as a two-level system (TLS) and the photonic modes of light are modeled as a bosonic environment. In the experiments, photonic modes are either confined in optical cavities [22–28] or they propogate in waveguides [29–33]. Most of the experiments are carried out in the strong coupling regime, where the evolution is Markovian and confined to a subspace with fixed number of excitations. Higher coupling strengths which give rise to non-Markovianity and many-body effects have been reached, in recent experiments [34–42]. Quantum optical systems have proven to be very useful for observing new phases of matter and studying many-body physics [1]. They are also promising tools for quantum information processing [43].

Quantum walks have been proposed almost three decades ago [44] as the quantum counterpart of classical random walks and they attracted considerable attention in the first place due to their quadratically faster spreading rates compared to those of their classical analogues [45, 46]. The subject has gained its place in quantum computation as a substantial field of research on both theoretical and experimental sides [45]. It turned out that quantum walks are versatile models for quantum computation, not only due to their role in the development of new quantum algorithms [47–54]but also for providing a concrete framework for universality [55]. They also provide a powerful framework for simulating physical systems [56,57], quantum state transfer [58–62] and for examining topological quantum matter [63–67]. Quantum walks can be realized in various experimental setups, including ultracold atoms in optical lattices [12], trapped

ions [13,14], nuclear magnetic resonance schemes [68,69], photons in a fibre loop [70], beam splitter arrays [71] and waveguide lattices [72].

In this thesis, we mainly concentrate on a one-dimensional tensor network family, namely, MPS, and their applications to quantum optical systems and quantum walks. The fundamental aspects of the MPS and the numerical library we have developed to implement MPS algorithms are explained in Chapter 2. In Chapter 3 interaction between light and a two-level system on a coupled cavity array is considered. We compare MPS results to those obtained from the exact diagonalization in strong and perturbative coupling regimes. We study the effects and optimum parameters of absorbing boundary conditions in strong coupling regime. We study two different quantum walk problems and analyse localization properties due to decoherence. Chapter 4 is devoted to the relation between localization and non-Markovianity for a quantum walk with a single phase impurity. In Chapter 5, we extend this quantum walk model to incorporate a spin-chain environment and study the connection between localization, entanglement and spin properties using MPS. We summarize our results and discuss our future outlook in Chapter 6.

2. MATRIX PRODUCT STATES

This chapter is devoted to the Matrix Product States (MPS) formalism and the numerical library we have developed. We discuss the fundamentals of the MPS formalism such as MPS representation of quantum states and the time-evolving block decimation (TEBD).

Tensor networks have become very popular in the simulations of low-dimensional quantum many-body systems. One of the reasons of this popularity is their efficiency in terms of computational and memory resources. Simulation of quantum many-body systems is challenging due to the fact that the Hilbert space grows exponentially with the system size. However, physically relevant states that are accessible via a realistic evolution constitute only a small portion of the Hilbert space. For a given initial state, majority of the states are not reachable within a reasonable evolution time [2, 3]. Another factor restricting the size of the effective Hilbert space for many physical systems is the locality of interactions. When the interactions between different components of a system are local, the entanglement entropy of the low-energy eigenstates of gapped Hamiltonians obey the area-law [2–4, 10]. This means that the entanglement entropy does not scale with the system size, but scales with the size of the boundary between two partitions. The number of states having this property are very limited compared to the immense size of the Hilbert space and tensor network algorithms target these states with low entanglement. Hence, these algorithms have proven to be efficient methods to simulate low-energy quantum states of many-body systems obeying the area-law. Another advantage of the tensor network representation is its structure. A tensor network can be thought as a network of quantum correlations, therefore it makes some of the intrinsic features of a state, such as the structure of the entanglement between its constituents, directly accessible [3]. Tensor networks also feature a diagrammatic representation.

In this thesis we focus on MPS [2, 3, 5–10], which is a family of one-dimensional tensor networks. We have developed a numerical library in Python to implement our

MPS algorithms. The library includes codes to obtain the MPS representation for any given state both in general and in canonical forms. The latter are more efficient for certain computational tasks. It also includes functions to compute expectation values of operators and to apply the TEBD method. The library can be accessed online [73].

2.1 Singular Value Decomposition and Entanglement Entropy

In MPS representation, the quantum state is represented with a one-dimensional array of tensors, where each tensor is associated with local degrees of freedom. The tensors are obtained using singular value decomposition (SVD) [74].

Let us first consider SVD of a system into two components A and B and let $|\Psi\rangle$ be a pure state of the composite system AB,

$$|\Psi_{AB}\rangle = \sum_{i,j} \psi_{ij} |i_A\rangle |j_B\rangle , \tag{2.1}$$

where $|i_A\rangle$ and $|j_B\rangle$ are orthonormal bases for A and B, respectively. Using SVD, the coefficient matrix ψ can be decomposed into three matrices, such that $\psi = USV^\dagger$, and the state can be rewritten as

$$|\Psi_{AB}\rangle = \sum_{i,j} \sum_{\alpha=1}^{\chi} U_{i\alpha} \Lambda_{\alpha\alpha} V^*_{\alpha j} |i_A\rangle |j_B\rangle , \tag{2.2}$$

Here, U has orthonormal columns (the left singular vectors) and $V^\dagger$ has orthonormal rows (the right singular vectors). Λ is a diagonal matrix which assumes the singular values of ψ, $\sigma_\alpha = \Lambda_{\alpha\alpha}$, as its diagonal elements, preferably in descending order. The number of non-zero singular values, χ, for a given partition is called the Schmidt rank.

The squares of the singular values are the eigenvalues of the reduced density matrix, ρ, of either subsystem, i.e. the partition to the left or right of a given bond. Therefore, the von Neuman entropy, $S(\rho_A) = -\mathrm{Tr}[\rho \log \rho]$, becomes

$$S = -\sum_{\alpha=1}^{\chi} \left[\sigma_\alpha^2 \log \sigma_\alpha^2\right] . \tag{2.3}$$

Note that the eigenvalues σ_α satisfy the normalization condition $\sum_\alpha \sigma_\alpha^2 = 1$.

2.2 MPS Representation

The above procedure can be repeated successively for systems with multiple components. Let us now consider a one-dimensional system with L sites, each having d degrees of freedom associated with them. The quantum state of such a system can be written as

$$|\Psi\rangle = \sum_{i_1,\ldots,i_L}^{d} \psi_{i_1,\ldots,i_L} |i_1,\ldots,i_L\rangle . \tag{2.4}$$

To obtain an MPS representation of the state, the first step is to isolate either the leftmost or rightmost block, i.e. combining the tensor S with U or V, respectively, and to apply SVD to this new block. This procedure is repeated until the block size is reduced to a single site. The resulting MPS is in the form

$$\begin{aligned} |\Psi(n)_{\text{canonical}}\rangle \quad = \quad & \sum_{i_1\ldots i_L}^{d} \sum_{\alpha_1\ldots\alpha_{L-1}} \\ U^{i_1}_{\alpha_1} U^{i_2}_{\alpha_1\alpha_2} \quad \ldots \quad & U^{n-1}_{\alpha_{n-2}\alpha_{n-1}} A^{i_n}_{\alpha_{n-1}\alpha_n} \left(V^{\dagger}\right)^{i_{n+1}}_{\alpha_n\alpha_{n+1}} \ldots \left(V^{\dagger}\right)^{i_{L-1}}_{\alpha_{L-2}\alpha_{L-1}} \left(V^{\dagger}\right)^{i_L}_{\alpha_{L-1}} |i_1\ldots i_L\rangle \end{aligned} \tag{2.5}$$

(See Fig. 2.1 for a schematic representation of an MPS in general form). Here, U and $V^{\dagger}$ matrices are left and right orthonormal, respectively, and the state is said to be canonical with respect to site n. The physical indices are $i_n = 1,\ldots,d$ and the virtual indices are $\alpha_n = 1,\ldots,D_n$, where d is called the physical dimension, and D_n are called bond dimensions. We restrict ourselves to open-boundary conditions. Therefore, the first and last tensors have only single bond index.

The efficiency of the MPS formalism can be seen by comparing sizes of the original Hilbert space and the effective space MPS lives in. The dimension of the Hilbert space of the original state is $\dim(\mathcal{H}) = d^L$. On the other hand, the Hilbert space of the matrix product state has the dimension of $\sum_{n=0}^{L-1} dD_nD_{n+1}$, where D_0 and D_L are set to one. If there exists an upper limit, $D_{\max}$, for the bond dimensions, $\dim(\mathcal{H}_{\text{MPS}}) \leq dLD^2_{\max}$.

Note that the MPS representation in Eq. (2.6) is not unique, in the sense that the state could be made canonical with respect to any site. This freedom provides an efficient way of manipulating the MPS state and computing the expectation values [10]. For example, on-site expectation values can be calculated using the canonical form pivoted

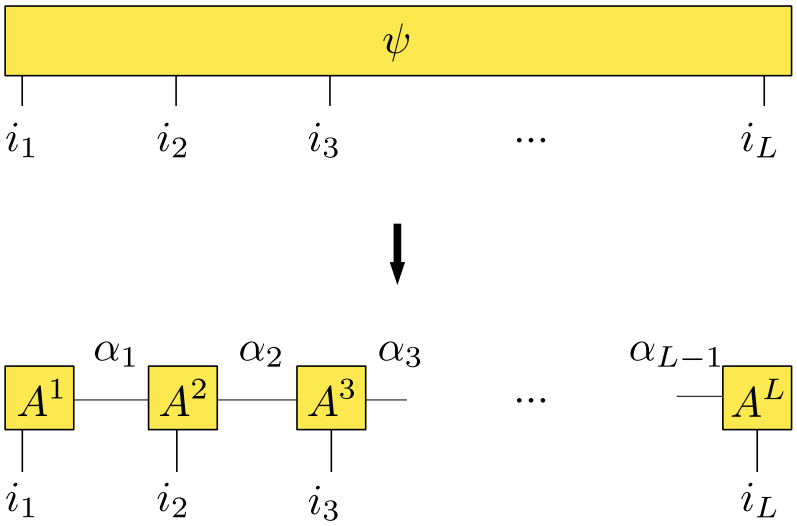

Figure 2.1 : Tensor network representation of a quantum state $|\Psi\rangle$ in Eq. 2.4, in general form.

on that site as the tensors to the left and right of the site reduce to identities when contracted.

2.3 Truncation Process

The size of the effective Hilbert space of an MPS is limited by the maximum of Schmidt rank, χ_{max} (see Eq. (2.2)), over all possible partitionings. For a maximally entangled state, χ_{max} grows exponentially with the system size. On the other hand, for a generic many-body pure-state generated by a unitary evolution and local interactions, χ_{max} increases polynomially with system size [75]. The size of the effective Hilbert space can be reduced further by truncating the singular values.

Truncation can be done in two ways; by assigning a maximum bond dimension D_{max} or a truncation tolerance, δ. In the former case, maximum number of non-zero singular values kept at each truncation is limited to D_{max} and only when $\chi \leq D_{\text{max}}$, all the singular values are kept. In the latter case, maximum number of singular values are eliminated ensuring that sum of the squares of the eliminated singular values do not exceed δ and adjusting D_{max} accordingly. In our algorithm, we use the truncation tolerance for the truncation of the singular values. In this section, we show the computational error due to the truncation procedure, for two randomly generated MPS.

Let us rewrite Eq.(2.2) in a more compact form which is called Schmidt decomposition,

$$|\Psi\rangle = \sum_{\alpha=1}^{\chi} \sigma_\alpha |A_\alpha\rangle |B_\alpha\rangle , \tag{2.6}$$

where $|A_\alpha\rangle \equiv U_{i\alpha} |i_A\rangle$, $|B_\alpha\rangle \equiv V^*_{\alpha j} |j_B\rangle$ and $\sigma_\alpha \equiv \Lambda_{\alpha\alpha}$.

The Schmidt rank is restricted by the dimensions of the components A and B, so that $\chi = \min(d_A, d_B)$. For example, if the system is a chain of N spin 1/2 particles and it is split in half, then $\chi = 2^{N/2}$.

Truncation aims to reduce the number of singular values so that $D \leq \chi$, After applying truncation procedure, T, between the two components, the state becomes

$$T |\Psi\rangle = \sum_{\alpha=1}^{D} \sigma_\alpha |A_\alpha\rangle |B_\alpha\rangle . \tag{2.7}$$

We quantify the computational error by the 2-norm distance between the original and the truncated state, which is obtained by summing the squares of the eliminated singular values as

$$\varepsilon_{\mathbf{2-norm}} \equiv \frac{1}{C} || \, |\Psi\rangle - T |\Psi\rangle \, ||^2 = \frac{1}{C} \sum_{r=D+1}^{\chi} \sigma_r^2 \equiv \varepsilon_\sigma . \tag{2.8}$$

Here, C is the 2-norm of the original state which can be obtained by summing the squares of all the singular values, so that $|| \, |\Psi\rangle \, ||^2 = \sum_{r=1}^{\chi} \sigma_r^2 = C$. For a given tolerance, δ, singular values with $r > D$ are eliminated such that the condition $\varepsilon_\sigma < \delta$ is satisfied.

For a system of multiple components, as in Eq. (2.4), the truncation procedure is carried out for each bond successively. In this case, an exact value for the total error cannot be computed theoretically. However, the triangle inequality provides an upper bond for the error.

Let T_n denote truncation on the $n^{\mathbf{th}}$ bond. After applying the above truncation process to each bond successively, the total error is upper-bounded as

$$\begin{aligned} || \, |\Psi\rangle - T_{N-1} T_{N-2} \dots T_1 |\Psi\rangle \, || \leq || \, |\Psi\rangle - T_1 |\Psi\rangle \, || + || T_1 |\Psi\rangle - T_2 T_1 |\Psi\rangle \, || + \\ \cdots + || T_{N-2} \dots T_1 |\Psi\rangle - T_{N-1} T_{N-2} \dots T_1 |\Psi\rangle \, ||. \end{aligned} \tag{2.9}$$

Each term on the right-hand side of this equation can be computed from Eq. (2.8).

We test Eqs. (2.8) and (2.9) for two randomly generated quantum states. For each system, we first generate a random MPS representation, normalized to unity

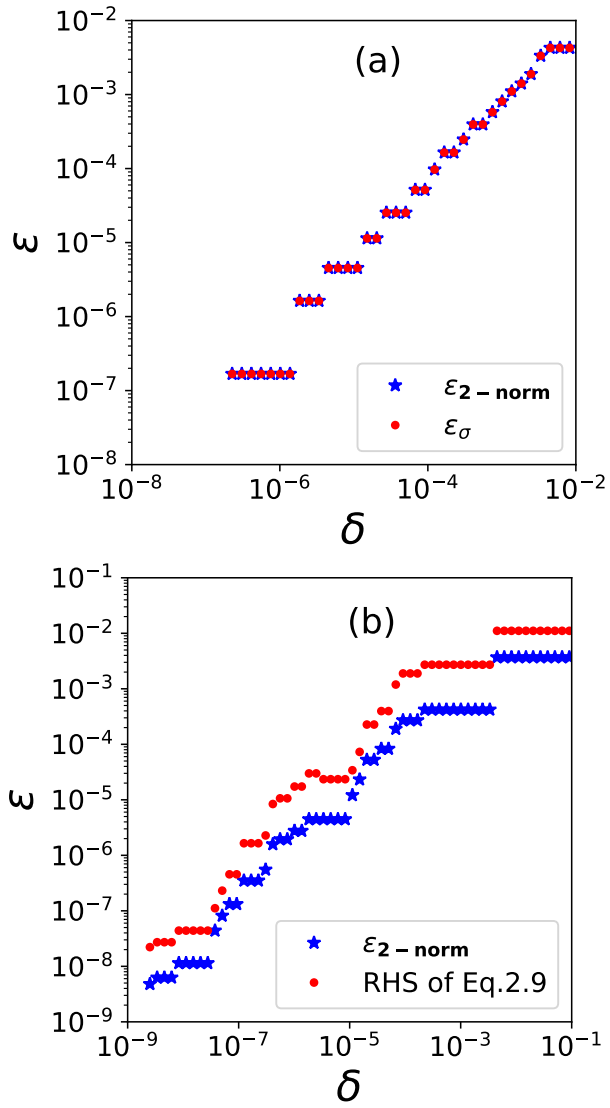

Figure 2.2 : Dependence of the truncation error, ε, on the truncation tolerance, δ, for an initial MPS of two sites, with dimensions $d = 20$ and $D = 100$ (a) and an initial MPS of 10 sites, with dimensions $d = 2$ and $D = 10$ (b). The blue marks show the 2-norm error computed using Eq. (2.10). The red marks represent the RHSs of Eqs. (2.8) (a) and (2.9) (b).

with relatively large bond dimensions and compare it with the resulting MPS after truncation. For comparison, we compute the numerical error, using the overlap between the original state and the truncated state, as

$$\varepsilon_{\mathbf{2-norm}} = \left| 1 - \frac{\langle \Psi | T | \Psi \rangle}{C} \right| \tag{2.10}$$

which is equivalent to the 2-norm distance between the two states given in Eq.(2.8). We compute how this value changes as a function of the truncation tolerance and compare it to its predicted value obtained from the RHS of Eq. (2.8).

The first system is a two-site system where there is a physical dimension $d = 20$ associated with each site. We consider an initial MPS with bond dimension $D = 100$. Since truncation is carried out on a single bond, the numerical error is determined by the RHS of Eq. (2.8). Fig. 2.2 (a) shows this equality holds for any truncation tolerance we used in our computation. We made the same comparison for a system of $L = 10$ sites with dimensions $d = 2$ and $D_{\max} = 10$ (see Fig. 2.2 (b)). In this example truncation is carried out for each bond successively. Here, we observe that the numerical error in 2-norm is always upper bounded by the value obtained from eliminated singular values, as expected. For both systems, the errors increase with truncation tolerance, in general. For an infinite-size system, this increase is linear, whereas for finite systems, discrete nature of singular values yields a ladder-like increase as both examples show.

2.4 Time-Evolving Block Decimation

2.4.1 Suzuki-Trotter decomposition

In our algorithm, we use Time-Evolving Block Decimation [76] to evolve the MPS states. This method makes use of Suzuki-Trotter decomposition [77, 78] to approximate the time evolution operator $\hat{W}$ for a nearest-neighbor interaction Hamiltonian. These are the Hamiltonians that can be written in the form,

$$\hat{H} = \sum_{j=1}^{L-1} \hat{h}_{j,j+1}, \tag{2.11}$$

with pairwise operators $\hat{h}_{j,j+1}$ acting on two neighboring sites. Each of these operators can consist of both on-site and bond operators. As a simple example consider a tight-binding model with on-site energies, ω_j and hopping terms, $t_{j,j+1}$. Each of the operators in the above sum can be written as

$$\hat{h}_{j,j+1} = \left(\frac{\omega_j}{2}\hat{a}_j^\dagger \hat{a}_j\right) + \left(\frac{\omega_{j+1}}{2}\hat{a}_{j+1}^\dagger \hat{a}_{j+1}\right) + \left(t_{j,j+1}\hat{a}_j^\dagger \hat{a}_{j+1} + \text{h.c.}\right), \tag{2.12}$$

where a and $a^\dagger$ are annihilation and creation operators, respectively. Since each one of the on-site operators, except the first and the last, appear twice in the summation in Eq. (2.11), they are divided by two. On the other hand, the first and the last on-site operators appear only once, in $\hat{h}_{1,2}$ and $\hat{h}_{L-1,L}$, respectively. Therefore, we need to add two on-site terms $\hat{h}_1 = \left(\frac{\omega_1}{2}\hat{a}_1^\dagger \hat{a}_1\right)$ and $\hat{h}_N = \left(\frac{\omega_N}{2}\hat{a}_N^\dagger \hat{a}_N\right)$, to the corresponding summands, so that $\hat{h}_{1,2} \to \hat{h}_{1,2} + \hat{h}_1$, and $\hat{h}_{N-1,N} \to \hat{h}_{N-1,N} + \hat{h}_N$.

If we group the pairwise operators for even and odd bonds j as

$$\hat{H}_{\text{even}} = \sum_{j \text{ even}} \hat{h}_{j,j+1} \tag{2.13}$$

$$\hat{H}_{\text{odd}} = \sum_{j \text{ odd}} \hat{h}_{j,j+1} \tag{2.14}$$

so that $\hat{H} = \hat{H}_{\text{even}} + \hat{H}_{\text{odd}}$, the operators $\hat{h}_{j,j+1}$ within each group commute with each other. Therefore, $\hat{H}_{\text{even}}$ and $\hat{H}_{\text{odd}}$ can be exponentiated individually as

$$e^{-i\Delta t \hat{H}_{\text{even (odd)}}} = e^{-i\Delta t \sum_{j \text{ even (odd)}} \hat{h}_{j,j+1}} = \prod_{j \text{ even (odd)}} e^{-i\Delta t \hat{h}_{j,j+1}}. \tag{2.15}$$

Since $\hat{H}_{\text{even (odd)}}$ commutes with the commutator $[\hat{H}_{\text{even}}, \hat{H}_{\text{odd}}]$, the evolution operator can be obtained using the Baker-Campbell-Hausdorff formula

$$\hat{W}^{\text{exact}}(\Delta t) = e^{-i\Delta t \hat{H}} = e^{-i\Delta t \hat{H}_{\text{even}}} e^{-i\Delta t \hat{H}_{\text{odd}}} e^{-i\Delta t^2/2 \left[\hat{H}_{\text{even}}, \hat{H}_{\text{odd}}\right]}. \tag{2.16}$$

The last term can be approximated as

$$e^{-i\Delta t^2/2 \left[\hat{H}_{\text{even}}, \hat{H}_{\text{odd}}\right]} \approx \hat{1} - i\Delta t^2/2 \left[\hat{H}_{\text{even}}, \hat{H}_{\text{odd}}\right]. \tag{2.17}$$

If we approximate the evolution operator as

$$\hat{W}^{\text{TEBD}}(\Delta t) = e^{-i\Delta t \hat{H}_{\text{even}}} e^{-i\Delta t \hat{H}_{\text{odd}}}, \tag{2.18}$$

the error per time step between the exact and the approximate evolution operators is of second order in Δt

$$\hat{W}^{\text{exact}}(\Delta t) = \hat{W}^{\text{TEBD}}(\Delta t) + O(\Delta t^2). \tag{2.19}$$

An evolution for a longer time interval T, is divided into $T/\Delta t$ number of smaller intervals and the operator $\hat{W}^{\text{TEBD}}(\Delta t)$ is applied at each time step. The accumulated error becomes $\frac{T}{\Delta t} O(\Delta t^2) = O(\Delta t)$. Hence, this approximation is called first-order TEBD. Higher order approximations can be used to reduce the error. For instance, the second-order TEBD is obtained by symmetrizing the decomposition in Eq. (2.18) as

$$\hat{W}^{\text{TEBD2}}(\Delta t) = e^{-i\Delta t/2 \hat{H}_{\text{even}}} e^{-i\Delta t \hat{H}_{\text{odd}}} e^{-i\Delta t/2 \hat{H}_{\text{even}}}, \tag{2.20}$$

which has an error per time step of third order in Δt

$$\hat{W}^{\text{exact}}(\Delta t) = \hat{W}^{\text{TEBD2}}(\Delta t) + O(\Delta t^3). \tag{2.21}$$

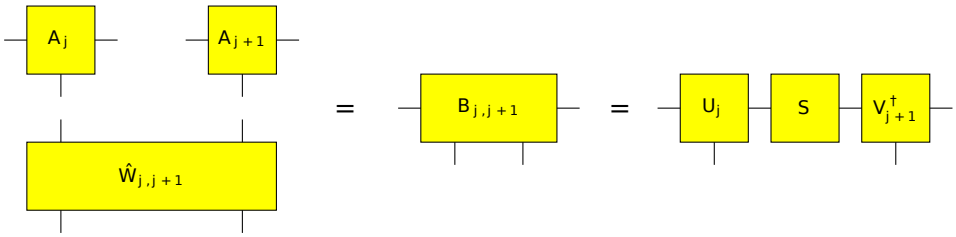

Figure 2.3 : Contraction of two neighboring MPS tensors, A_j and A_{j+1}, with the two-site evolution operator $\hat{W}_{j,j+1}$.

2.4.2 Contraction of tensors and orthonormalization

During the time evolution, each term $\hat{W}_{j,j+1} = e^{-i\Delta t \hat{h}_{j,j+1}}$ in Eq. (2.15) is applied individually on a pair of neighboring sites A_j and A_{j+1}. This is done by contracting the three tensors as shown in Fig. 2.3. The resulting tensor (B in the figure) is a two-site tensor. It is split back into two tensors by applying SVD as $B = USV^\dagger$ (See Sec. 2.1) and combining S with either U or V. The former (latter) leaves the rightmost (leftmost) tensor in right (left) orthonormal form. The remaining tensor is brought to the same form by another SVD.

During this procedure, truncation of the singular values is carried out as explained in Sec. 2.3, to restrict the increase in the bond dimension.

2.4.3 Time evolution algorithm

The steps of our time evolution algorithm, starting from an initial MPS, are as follows:

1. Obtain two-site evolution tensors, $\hat{W}_{j,j+1} = e^{-i\hat{h}_{i,i+1}\Delta t}$ in Eq. (2.15) and group them as $\hat{W}^{\text{even}}_{j,j+1}$ and $\hat{W}^{\text{odd}}_{j,j+1}$, for j even or odd, respectively.

2. Bring the initial MPS into canonical form with respect to a site, which we call n_{center}. This site should be one of the neighboring sites which the first two-site evolution tensor will act on in the following step. Since we choose to apply $\hat{W}_{1,2}$ first, we bring the MPS in canonical form with respect to site $n_{\text{center}} = 1$.

3. Sweep from left to right by successively applying $\hat{W}^{\text{odd}}_{j,j+1}$ to the tensors, A_j and A_{j+1} simultaneously and split the resulting tensor into two left-orthonormal tensors as explained in Sec. 2.4.2. Note that each time a tensor is brought to left-orthonormal form, n_{center} moves to the right by one site until the rightmost site is reached.

4. Similar to step (3), sweep from right to left by successively applying $\hat{W}^{\text{even}}_{j,j+1}$ to the corresponding MPS tensors, followed by right orthonormalization. At the end of the sweep n_{center} becomes one again due to the orthonormalization processes.

5. Repeat steps (3) and (4) successively at each time step.

2.5 Computational Error

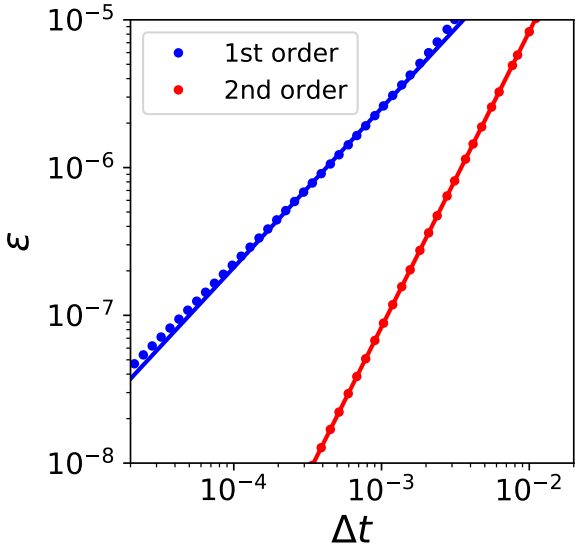

Figure 2.4 : 2-norm error (see Eq. (2.22)) as a function of time step interval, Δt, obtained from the MPS algorithm using the first order (blue dots) and second order (red dots) Suzuki-Trotter decompositions. Continuous lines are linear fits in log-log scale with slopes 1.08 and 2.00 for the 1st and 2nd order expansions, respectively.

In this section, we consider how the computational error changes with increasing time-step interval for the tight-binding model with random nearest-neighbor interactions, $t_{j,j+1}$, and random site-based frequencies, ω_j (see Eq. (2.12)).

We consider an initial MPS having 10 sites with the dimensions $d = 2$ and $D = 10$. We choose a value close to the machine precision for the truncation tolerance, $\delta = 10^{-16}$. The state is evolved for a total time interval of $T = 0.1$. We compute the 2-norm error between the evolved MPS state, $|\Psi_{\mathbf{MPS}}\rangle$, and the final state, $|\Psi_{\mathbf{exact}}\rangle$, exactly evolved using the vectorial form of the initial state and matrix form of the Hamiltonian as

$$\varepsilon = ||\,|\Psi_{\mathbf{exact}}\rangle - |\Psi_{\mathbf{MPS}}\rangle\,||^2. \tag{2.22}$$

The results are shown in Fig. 2.4. As seen from Eq. (2.19), the error in the first order Suzuki-Trotter decomposition after a single time step is on the order of $(\Delta t)^2$. After

$T/\Delta t$ time steps, the accumulated error is on the order of Δt. Whereas for second order decomposition, the accumulated error after the same number of steps scales as $(\Delta t)^2$. Our simulations yield results consistent with these predictions. As the time step interval increases, the error in 2-norm increases as $t^{1.08}$ for the 1st order decomposition, and as $t^{2.00}$ for the 2nd order decomposition.

3. ATOM - PHOTON INTERACTIONS ON COUPLED CAVITY ARRAYS

The interaction between light and matter has been an important field of research both for its applications in quantum technologies and for its potential of shedding new light on fundamental physics problems at the quantum level. Until recently, the interaction strengths reached in experiments were limited to weak and strong coupling regimes, where the coupling between light and matter is relatively small compared to their bare energies. Due to the advances in the control and manipulation of quantum systems, ultra-strong coupling (USC) regime has been reached. Most of the experiments with USC have been performed in the perturbative regime where the coupling strength is less than one fifth of the photon frequency [34–40]. The non-perturbative USC regime has been reached recently using superconducting qubits coupled to a transmission line [41] and to a microwave resonator [42]. Another important achievement has been the emulation of Dicke physics, which involves cooperative interaction of multiple qubits with a photonic field, at room temperature [79]. These experiments in the USC regime have presented novel phenomena, such as the existence of both atomic and photonic excitations in the ground state and their entangled nature, chaotic regimes, Bloch-Siegert shift in the resonance frequency [80], asymmetric Fano resonance and inelastic Raman processes [81].

One of the main challenges in the simulations of quantum optics problems is the exponential growth of the Hilbert space with increasing system size. Therefore, approximate methods are necessary in the treatment of these problems. In the weak and the strong coupling regimes, the rotating wave approximation (RWA) limits the solutions to the excitation number invariant subspaces and the problem can be solved analytically [11, 82, 83]. In the perturbative regime, RWA can be applied after an optimized polaron transform [84, 85]. However, beyond the perturbative regime, these approximations break down and numerical methods such as tensor network algorithms are needed.

Another challenge is the study of long-time dynamics of unbounded quantum systems on a numerical grid. To make the grid small enough for efficient simulation, it is necessary to impose artificial boundary conditions. When the problem admits propagating wave solutions, the reflection from the boundaries can disrupt the dynamics in the interior region. Absorbing boundary conditions (ABC) are used to minimize such reflections. These boundary conditions need to fulfill the requirements such as being well-posed so that they are unique and stable, the numerical solution should be bounded and all the incident waves should be destructed to prevent any reflection [86]. Here, the form and the parameters such as those of an imaginary potential to do simulations should be chosen carefully. This potential should not affect the evolution outside of the absorbing region. One of the drawbacks is the loss of quantum correlations. For example, in a many-body system, when a particle is absorbed through a non-Hermitian process, the norm of the wave function decreases and the loss of information is irreversible [87]. Another drawback is that the waves which have wavelengths longer than the absorbing region are reflected from the boundary [88].

In this chapter, we investigate the interactions between a quantum emitter and a one-dimensional coupled cavity array (CCA). We study the photon dynamics in the strong coupling and perturbative USC regimes. We analyze the effects of the ABC and show the optimum intervals for the related parameters. Finally, we compare the results obtained by exact diagonalization to those obtained using the TEBD algorithm.

3.1 Spin-Boson Model in the Strong Coupling Regime

The spin-boson model describes a two-level system (TLS) interacting with a bosonic environment. It is the simplest dissipative model describing many different phenomena such as energy transfer [89, 90] and decoherence [91] in quantum optical systems, tunneling in condensed media [20, 92], charge transfer [93], quantum phase transitions [94, 95], electronic transport in biological complexes [96] and quantum simulators [97]. Depending on the application, TLS can be modeled by any pseudo-spin $\frac{1}{2}$ system, such as a quantum dot or a superconducting qubit, where only two energy levels are coupled to the bosonic environment.

The Hamiltonian of a spin-boson model can be written as

$$\hat{H} = \frac{\Delta}{2}\sigma^z + \sum_{kj} \bar{H}_{kj} a_k^\dagger a_j + \sigma^x \sum_k \left(g_k a_k^\dagger + \text{H.c.} \right), \tag{3.1}$$

where we set $\hbar = 1$. Here, σ^x and σ^z are the Pauli operators acting on the TLS and Δ is the excitation energy of the TLS. $a_k^\dagger$ and a_k are the creation and annihilation operators of the bosonic mode k, respectively.

$\bar{H}_{kj}$ are matrix elements of a bi-linear Hamiltonian which describes a simple model for the bosonic environment. The bosonic environment we consider is an optical CCA. Here, the spatial profiles of the cavity modes overlap yielding photon hopping between adjacent cavities [1, 98, 99]. Therefore, the array can be modeled by the tight-binding Hamiltonian. In the case of a one-dimensional homogeneous CCA, this Hamiltonian becomes $\sum_n \left(\omega a_n^\dagger a_n + J(a_n^\dagger a_{n+1} + \text{H.c.}) \right)$. Here ω is the energy of the photonic excitations and J is the hopping parameter between adjacent cavities.

The last term describes the interaction between the TLS and the photonic modes, in accordance with the quantum Rabi model [100, 101]. Here g_k is the interaction strength between the TLS and the k^{th} mode. Normally, the interactions between photons and atoms are very weak and last for a very short duration. Therefore, the interactions are enhanced by trapping atoms in nanophotonic structures in the laboratory. Depending on the relative strength of these interactions, different methods are used to solve Eq. (3.1).

3.1.1 Rotating wave approximation

We first consider the strong coupling regime, where interaction strengths, g_k, are much higher than the decoherence rate [1], although, they are still too small compared to the bare energies of the photons and the TLS. Most of the techniques for manipulating interactions at a single photon level are developed for this regime [102, 103] and they have paved the way for optical transistors [104–106], single-photon routers [107], one-photon lasers [108], qubit-mediated entanglement [109] and efficient photo-detectors [110].

In the strong coupling regime, rotating wave approximation (RWA) is used for solving Eq. (3.1). [11, 82, 83]. Within this approximation the counter rotating terms which do not conserve the excitation number such as $\sigma^+ a_k^\dagger$ and $\sigma^- a_k$ are neglected. When the

RWA is applied, the interaction between the TLS and a single cavity mode is described by the Jaynes-Cummings model [111], and the interaction term in Eq. 3.1 reduces to $g\left(\sigma^- a_N^\dagger + \sigma^+ a_N\right)$.

In this section, we consider a TLS interacting with the cavity mode at the last site, N, in the strong coupling regime where $g \leq 0.1\omega$. Here, the spin-boson Hamiltonian in Eq. 3.1 takes the form

$$\hat{H}_{\text{RWA}} = \frac{\Delta}{2}\sigma^z + \sum_n \left(\omega a_n^\dagger a_n + J(a_n^\dagger a_{n+1} + \text{H.c.})\right) + \left(g\sigma^- a_N^\dagger + \text{H.c.}\right). \tag{3.2}$$

For small coupling the ground state of this Hamiltonian is the vacuum state where there are no bosons and the TLS is not excited. In the single-excitation subspace, the operator $C = \frac{1}{2}\sigma^z + \sum_n a_n^\dagger a_n$ is a constant equal to $\frac{1}{2}$ (ground state has $C = -\frac{1}{2}$ so that the difference between the states is 1). Therefore we can shift the energy by $\frac{\omega}{2}$, i.e. subtract from the above Hamiltonian ωC, and rewrite it in the single-excitation subspace as

$$\hat{H}_{\text{RWA}} = \frac{\delta}{2}\sigma^z + \sum_n J\left(a_n^\dagger a_{n+1} + \text{H.c.}\right) + \left(g\sigma^- a_N^\dagger + \text{H.c.}\right) \tag{3.3}$$

where $\delta = \Delta - \omega$ is called the detuning.

3.1.2 Absorbing boundary conditions

ABC can be applied in the form of an imaginary potential [112],

$$i\Gamma = i\sum_n \gamma_n a_n^\dagger a_n \tag{3.4}$$

so that the effective Hamiltonian becomes

$$\hat{H}_{\text{eff}} = \hat{H} - i\Gamma. \tag{3.5}$$

Here, γ_n approaches zero at the exterior of the absorbing region. The length and strength of the absorbing region should be chosen carefully, so that within the absorbing region all the incident waves are absorbed and outside of this region the imaginary potential does not have any effect on the evolution via the Hermitian part of the effective Hamiltonian.

3.1.3 Exact diagonalization

In CCAs, the size of the Hilbert space grows exponentially with the system size. However, when there are conserved quantities, the Hamiltonian can be blocked diagonalized in an appropriate basis. An exact diagonalization method can be used to solve such a system. The Hamiltonian in Eq. (3.3) is block diagonal in the basis with fixed number of excitations. Therefore, the states with different number of excitations do not mix during the time evolution. If the evolution is restricted to the single-excitation subspace, the wave function at any time can be written as a superposition with coefficients c_n and d so that

$$|\Psi\rangle = \sum_n c_n a_n^\dagger |g\rangle \otimes |vac\rangle + d\sigma^+ |g\rangle \otimes |vac\rangle. \tag{3.6}$$

In the Heisenberg picture, the time dependent creation, annihilation and Pauli operators satisfy

$$\frac{da_n^{(\dagger)}}{dt} = i[\hat{H}, a_n^{(\dagger)}],\ \frac{d\sigma^\pm}{dt} = i[\hat{H}, \sigma^\pm]. \tag{3.7}$$

For the Hamiltonian in Eq. (3.3), these equations become linear in $a_n^{(\dagger)}$ and $\sigma^\pm$. Therefore they can be written in matrix form

$$\frac{d\vec{A}}{dt} = -i\mathbf{M}\vec{A}, \tag{3.8}$$

where the vector is $\vec{A} = (a_1, \ldots, a_N, \sigma^-)$. The solution is

$$\vec{A} = e^{-i\mathbf{M}t}\vec{A}(t=0). \tag{3.9}$$

The ABC given in Eq. (3.4) acts on the position space as a damping factor, so that

$$\vec{A} = e^{-i\mathbf{M}t-\Gamma t}\vec{A}(t=0). \tag{3.10}$$

Here,

$$\mathbf{M} = \begin{pmatrix} \omega & J & & & & 0 \\ J & \omega & J & & & \\ & J & \omega & \ddots & & \\ & & \ddots & \ddots & J & \\ & & & J & \omega & g \\ 0 & & & & g & \Delta \end{pmatrix} \tag{3.11}$$

and

$$\Gamma = \begin{pmatrix} \gamma_1 & 0 & & & & 0 \\ 0 & \gamma_2 & 0 & & & \\ & 0 & \gamma_3 & \ddots & & \\ & & \ddots & \ddots & 0 & \\ & & & 0 & \gamma_N & 0 \\ 0 & & & & 0 & 0 \end{pmatrix} \tag{3.12}$$

are sparse matrices. Therefore, numerical simulations can be performed efficiently.

3.1.4 Results

In this section, we study photon dynamics in the strong coupling regime, where RWA is valid, and restrict our attention to the time evolution in the single-excitation subspace (see Eq. (3.3)).

The CCA is described by the tight-binding model which is diagonal in momentum basis. Therefore, the free-photon dispersion relation, shown in the top panel of Fig. 3.1, is

$$E_k = \omega + 2J\cos(ka), \tag{3.13}$$

where a is the lattice spacing. Since we omit ω in Eq. (3.3), we set it to zero for our simulations in the strong coupling regime. Around the middle of the band, where $k = \pm\pi/(2a)$, the dispersion is approximately linear (dashed red lines in the top panel of Fig. 3.1). In contrast, the dispersion is parabolic near the band edges. Similarly, the density of states is nearly constant around the middle of the band, whereas it diverges near the band edges [113].

Now we consider coupling between a TLS system and the free-photon environment. Here, we consider a semi-infinite chain where the TLS is coupled to the cavity at the edge. Due to the coupling, the TLS decays from its excited state into the photonic environment. We simulate this phenomenon using a time evolution starting from an initial state, where the TLS is in its excited state and photons are in the vacuum state, so that

$$|\Psi_0\rangle = |e\rangle \otimes |vac\rangle. \tag{3.14}$$

The middle and bottom panels of Fig. 3.1, show the decay of the excited state's population of the TLS, P_e. In the linear dispersion regime, where $\delta = 0$ and the TLS is in resonance with the cavities (middle panel), P_e decays exponentially with time and

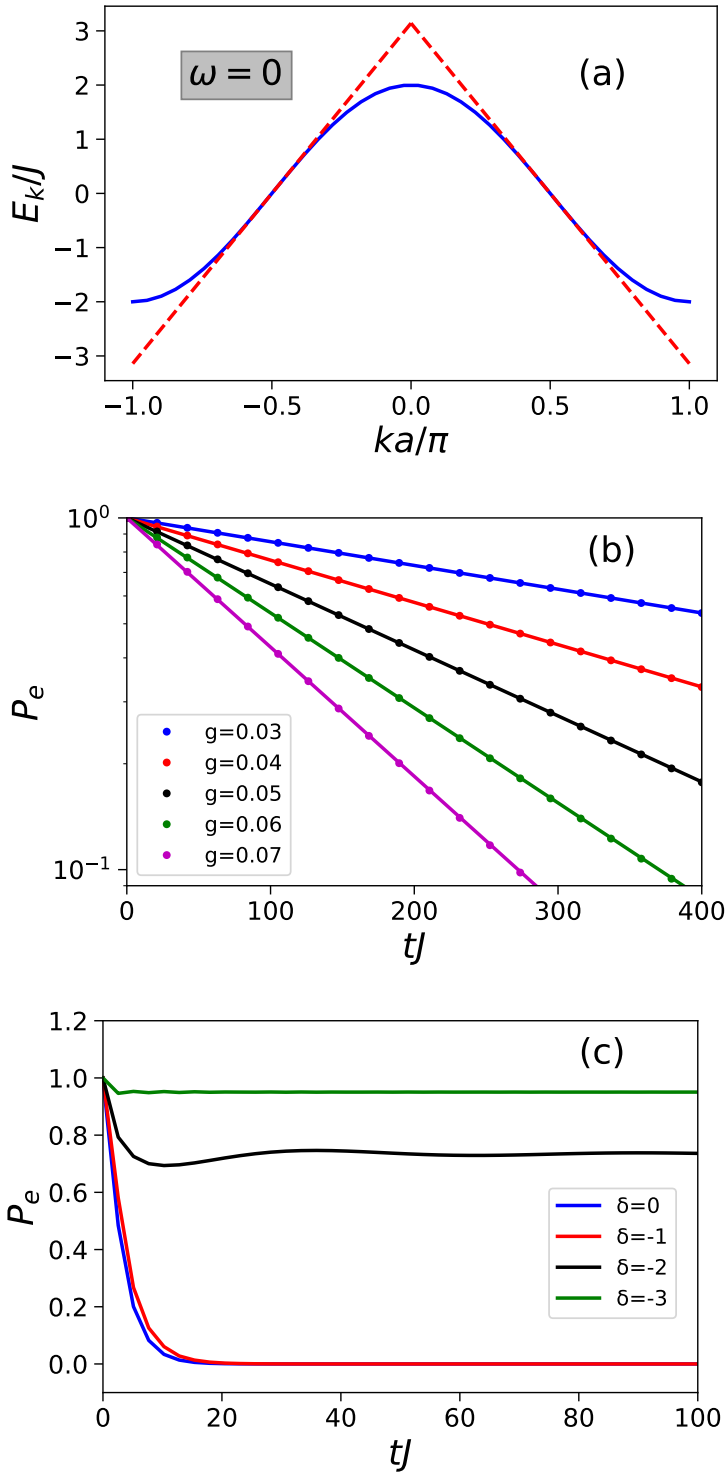

Figure 3.1 : The dispersion relation (see Eq. (3.13)) is shown by blue continuous curve and the linear fits at $ka = \pm\pi/2$ are shown by red dashed lines (top panel). The population of the excited state of the TLS, P_e, as a function of time for different coupling strengths g at the detuning $\delta = 0$ (middle panel). Here, the dots represent the numerical results and the continuous lines represent the exponential fits. P_e as a function of time for different δ at $g = 0.4$ (bottom panel).

the decay rate grows as g^2 [114–117]. Perfectly exponential decay of P_e in this time scale shows that for a long enough chain, where there are no reflected waves affecting the TLS, dynamics is purely Markovian.

The band structure of the bosonic environment affects the spontaneous emission of the TLS as well. We can observe this effect by changing the detuning. The bottom panel of Fig. 3.1 shows the decay of P_e for different detunings at coupling $g = 0.4$. The exponential decay of P_e occurs when the detuning, δ, lies within the band. The decay gets slower as δ approaches to the band edges due to the decreasing group velocity of the photons as seen by the blue ($\delta = 0$) and red curves ($\delta = -1$). When the detuning is far away from the band edge as seen by the green curve ($\delta = -3$), most of the excitation remains in the TLS. At the band edges, as seen by the black curve ($\delta = -2$), fractional decay occurs, where excitations decay partially into the bosonic environment and remain partially in the TLS [113].

3.1.4.1 Reflecting boundary conditions

In this section we present our results for reflecting boundary conditions considering a lattice of 1000 sites where the TLS is coupled to the last cavity. The initial state is the same as before (see Eq. (3.14)). We first turn our attention to the case in which $\delta = 0$, so that the TLS is in resonance with the cavity. To examine the photon dynamics, we compute the expectation value of the photon number for each site, $\langle a_n^\dagger a_n \rangle$ as a function of time.

As the TLS decays, it transfers its energy to the photonic field. When the detuning is zero, the emitted photons move with the frequency ω and a constant group velocity. Since the TLS decays more slowly as the coupling strength gets smaller, for small coupling strengths where RWA is valid, the lattice length should be long enough to observe the whole time evolution. Otherwise the unphysical reflections will affect the results.

In Fig. 3.2, we show the time evolution of the photon number expectations at $g = 0.04$. For the parameters we have chosen, a lattice of 1000 sites is not sufficient to observe the whole evolution. At around $t = 500$ (in the units of J^{-1}) the photons reach the left boundary, get reflected and they reach the initial site before the TLS completely decays

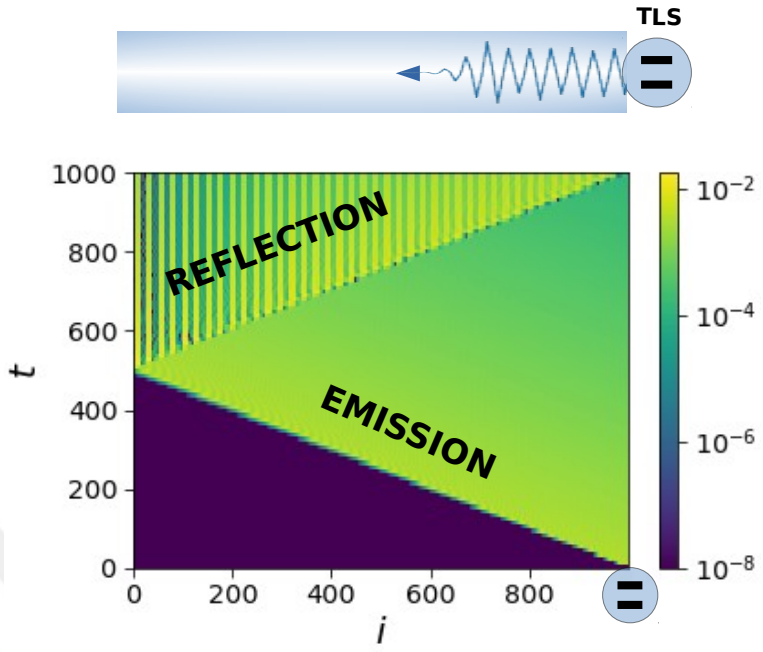

Figure 3.2 : The expectation value of the photon number for each site as a function of time, for $g = 0.04$, $\delta = 0$, and a lattice of 1000 sites without an absorbing boundary condition.

to its ground state. As a result, the dynamics throughout the lattice is highly disrupted due to the reflected waves.

3.1.4.2 Absorbing boundary conditions

Next, we consider ABC in the form of Eq. (3.4), where γ_n is an exponentially decaying function of position, $\gamma_n = \gamma e^{-n/l}$. Here γ and l correspond to absorption strength and absorption length, respectively. We aim to find the optimum parameters, so that distortion due to ABC in the interior region is minimum. For this reason, we consider two CCAs with lengths 1000 and 2000 sites, the former having ABC on the left boundary. Both of the arrays are coupled to a TLS at the rightmost site as before. We let the two systems evolve starting from the same initial state, which is given in Eq. (3.14), and compare the final states at $t = 1500$. We compute the error due to the distortion based on the difference between the expectation values of the photon numbers of the last 500 sites, $\Delta N = \sum_{n=500}^{1000} \left| \langle a_n^\dagger a_n \rangle_\Psi - \langle a_{n+1000}^\dagger a_{n+1000} \rangle_{\tilde{\Psi}} \right|$, where Ψ and $\tilde{\Psi}$ correspond to the final states of the time evolutions on the lattices of 1000 and 2000 sites, respectively. We divide this difference by the loss due to the absorption,

$\mathcal{L} = 1 - \sum_{n=1}^{1000} \langle a_n^\dagger a_n \rangle_\Psi$, to obtain distortion error per an absorbed photon, so that

$$\varepsilon = \frac{\Delta N}{\mathcal{L}} = \frac{\sum_{n=500}^{1000} \left| \langle a_n^\dagger a_n \rangle_\Psi - \langle a_{n+1000}^\dagger a_{n+1000} \rangle_{\tilde{\Psi}} \right|}{1 - \sum_{n=1}^{1000} \langle a_n^\dagger a_n \rangle_\Psi}. \tag{3.15}$$

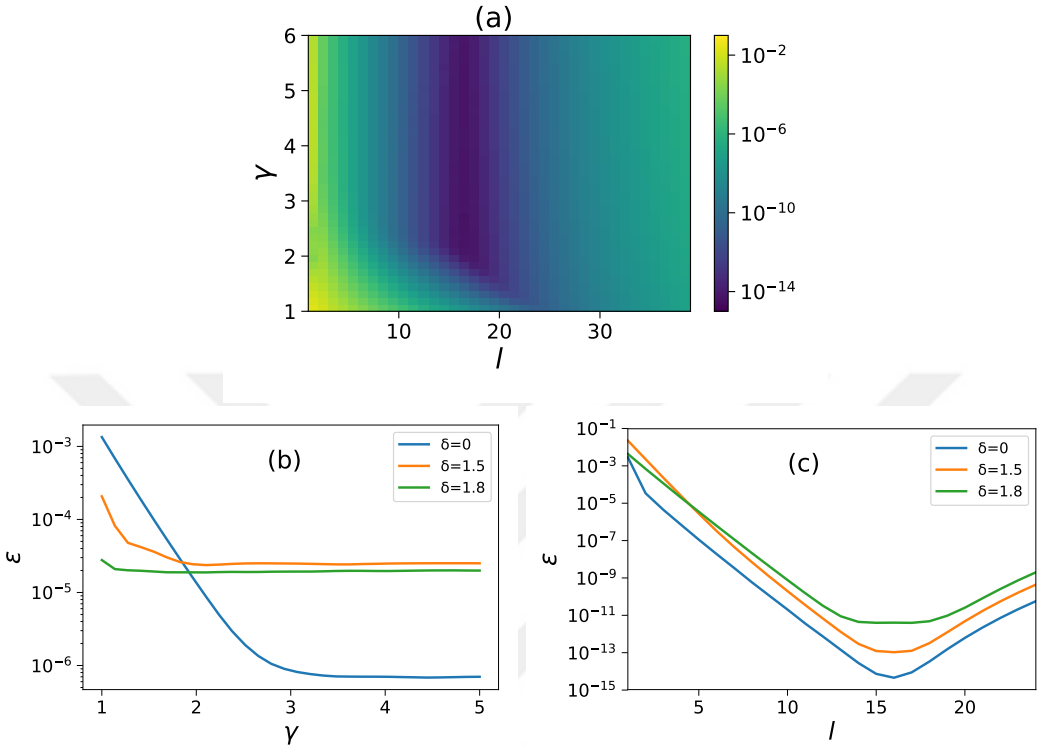

Figure 3.3 : Error due to distortion, ε, (see Eq.3.15) as functions of the absorption strength, γ, and the absorption length, l, at $\delta = 0$ (a). ε as a function of γ when $l = 4$ (b) and as a function of l when $\gamma = 4$ (c), for different values of δ.

In Fig. 3.3 (a), we examine how the distortion error, ε, changes with the absorption strength γ and the absorption length l for the linear dispersion regime ($\delta = 0$) and for an evolution time of $t = 1500$. The other parameters and the initial state are the same as in Sec. 3.1.4.1. In the region where $\gamma < 3$ and $l < 20$, ε is inversely proportional to $\gamma \times l$. When $\gamma \gtrsim 3$, ε is not affected very much by γ, therefore the error mostly depends on l. For sufficiently high values of γ, ε becomes minimum when $15 < l < 20$. ε becomes larger when absorption length gets smaller, since only the waves with wavelengths considerably smaller than the absorbing region are absorbed [88]. The increase in ε when l exceeds 20 is due to the limited size of the array. Increasing l further causes absorption of the photons in the interior region. For instance, let us consider the absorption on the middle site, $n = 500$, when $l = 40$. This site is about $12 \times l$ sites away from the boundary, therefore the magnitude of the imaginary potential drops to one millionth of γ. This yields an error more than 10^{-7}.

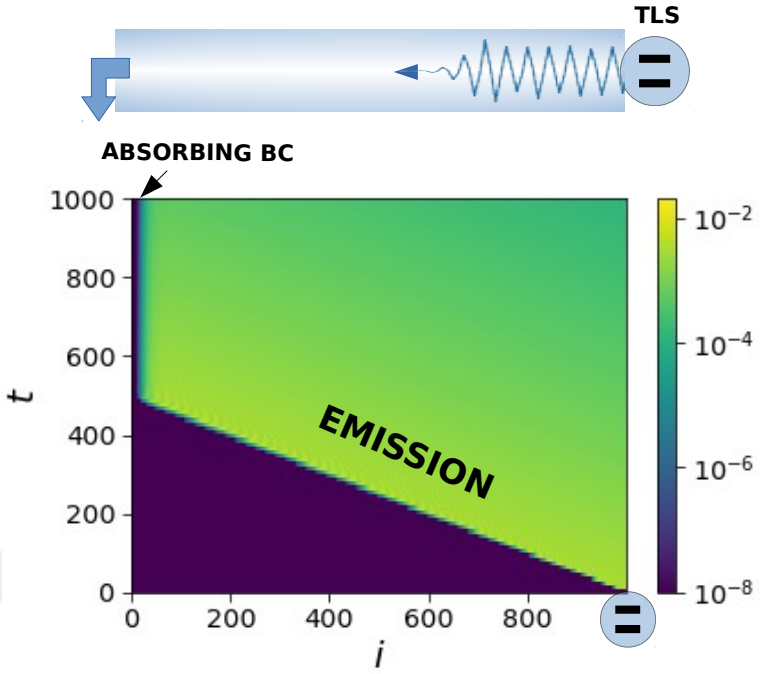

Figure 3.4 : The expectation value of the photon number for each site as a function of time, for $g = 0.04$, $\delta = 0$, and a lattice of 1000 sites with an absorbing boundary having parameters $\gamma = 4$ and $l = 10$.

Next, we study the relationship between ε and the detuning, δ, for different values of γ and l. Fig. 3.3 (b) shows ε as a function of γ for $l = 4$. Change in the detuning does not affect the overall behavior of ε, that is as γ is increased ε decreases first, and converges to a constant value. The constant value where the error settles down for large γ increases as δ increases from 0. This shows that as the photons slow down more distortion occurs, for $\gamma \gtrsim 2$.

Fig. 3.3 (c) reveals a similar relationship between the distortion error and the detuning with respect to the change in l. ε increases with increasing detuning for nearly all values of l. This may be due to the varying wavelengths of the photons near the band edges. As we mentioned before, the waves with wavelengths comparable to l are reflected [88] and as the detuning increases, more waves are reflected.

We next show the time evolution for ABC with parameters, i.e. $\gamma = 4$ and $l = 10$. We consider the same initial state and evolution parameters as in Fig. 3.2 and show the evolution of the photon dynamics in Fig. 3.4. As shown in the figure, for $\delta = 0$,

photons are fully absorbed, and in the interior region there are no reflecting waves disrupting the dynamics.

3.1.4.3 Simulations with Suzuki-Trotter decomposition

Finally, we consider the simulation of this model using Suzuki-Trotter decomposition and analyze the computational error (see Sec. 2.4.1). To eliminate the effect of the truncation, the evolution is restricted to the single-particle subspace, where the maximum value of the bond dimension is 2. We use the exact diagonalization method as before, with two major differences. Instead of exponentiating the full Hamiltonian, we first split it into $\hat{H}_{\text{even}} = \sum_{j\ \text{even}} \hat{h}_{j,j+1}$ and $\hat{H}_{\text{odd}} = \sum_{j\ \text{odd}} \hat{h}_{j,j+1}$ as in Eqs. 2.13 and 2.14, respectively. Secondly, we divide the evolution time, t, into small time intervals, δt and exponentiate $\hat{H}_{\text{even}}$ and $\hat{H}_{\text{odd}}$ separately as in Eqs. 2.18 and 2.20, for the first and second order Suzuki-Trotter decomposition, respectively. At each time step, we follow the same procedure as in Sec. 3.1.3, for each exponential factor in Eqs. 2.18 or 2.20, and apply them to the single-particle wave function consecutively.

As explained in Sec. 2.4, Suzuki-Trotter decomposition yields computational error depending on Δt, due to the non-commuting terms in the Hamiltonian. Here, we test TEBD in strong coupling regime with absorbing boundary conditions and determine the optimum time interval, Δt, for the MPS algorithm.

Here, we consider the effective Hamiltonian in Eq. 3.5, where $H_{\text{eff}} = H - i\Gamma$ with H being the H_{RWA} in Eq. (3.3). The time evolution is on a lattice of 100 sites for a total time of $t = 100$. The other parameters are the same as the system shown in Fig. 3.4. We compute the 2-norm error, $\varepsilon = ||\,|\Psi_{\mathbf{exact}}\rangle - |\Psi_{\mathbf{MPS}}\rangle\,||^2$, given in Eq. (2.22). As shown in Fig. 3.5, increase of the error with the time step interval is similar to our previous results (see Fig. 2.4) obeying a power law, $\varepsilon \sim \Delta t^a$, where the power a is 0.94 and 2.00 for first and second order expansions, respectively. Fig. 3.5 also shows that Δt can be increased up to 0.01 without causing significant order.

3.2 Spin-Boson Model in the Perturbative Coupling Regime

We now turn our attention to the USC regime. Although RWA is not valid in this regime, when g is small enough, as in the intermediate coupling regime, the problem can be solved by applying RWA after an optimized polaron transformation [84,85,118].

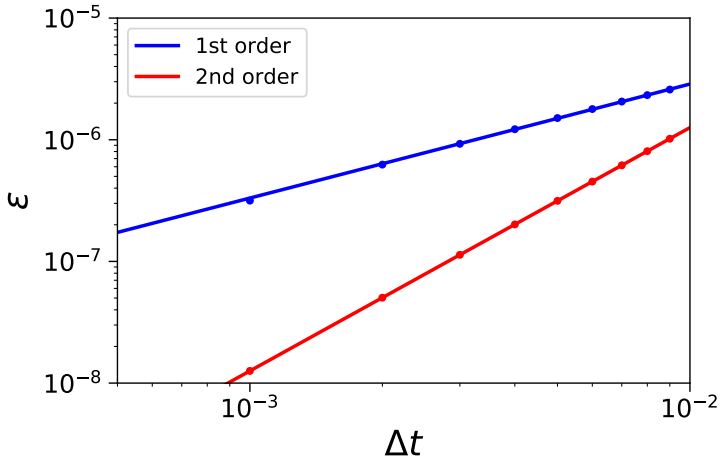

Figure 3.5 : The computational error as a function of time step interval in the first and second order Suzuki-Trotter decomposition, for a lattice of 1000 sites with an absorbing boundary having parameters $\gamma = 4$ and $l = 10$. The dots represent the numerical results and the continuous lines represent the fitting functions, $\varepsilon \sim \Delta t^a$, with the powers $a = 0.94$ and $a = 2.00$ for the first and second order expansions, respectively.

In the transformed basis, the coupling strength between the TLS and the cavity is renormalized to a smaller value. Therefore, we can apply RWA in this new basis.

3.2.1 Polaron Transformation

The method we describe here is inspired by the polaron concept [119] which was developed to explain how conduction electrons or holes move in a polar semiconductor or ionic crystal. As these particles move they induce polarization in the surrounding area creating a virtual phonon field. As a result, the particles get "dressed" by the phonon field, forming quasiparticles called polarons. The strong entanglement between the particles and the phonons makes the problem hard to solve in this basis. However, with an appropriate transformation, i.e. Lee-Low-Pines transformation [120], the reference frame is changed to the frame co-moving with the particle and the phononic part of the wavefunction can be factored out [121].

A similar approach can be used for the intermediate coupling strengths of the spin-boson model. In this regime, the counter rotating terms in the Hamiltonian in Eq. (3.1) become significant. Therefore, the ground state is no longer the vacuum but a dressed state comprised of the TLS and the photon cloud bound to it [81]. Since these dressed states contain the major part of the TLS-photon interaction, the effective coupling between the TLS and the dressed state is reduced. Hence, if the

Hamiltonian is transformed to the basis of these dressed states, the problem can be solved perturbatively in the intermediate coupling regime [118].

The transformation operator is

$$U_p = \exp\left[\sigma^x \sum_k f_k (a_k - a_k^\dagger)\right] \equiv \exp\left[\sigma^x (B - B^\dagger)\right] \tag{3.16}$$

with the collective mode

$$B = \sum_k f_k a_k. \tag{3.17}$$

Here, f_k are real coefficients. This transformation operator is similar to the displacement operator, $U = \exp\left[\sum_k f_k (a_k - a_k^\dagger)\right]$, [122], except that it has a spin dependence. The effect of the operator U_p is to displace the bosonic modes in the positive or negative direction depending on the spin state creating a coherent state of photons. With this approach the photons at each cavity can be treated as a mean field.

With the correct choice of f_k, the collective mode B becomes the bosonic field dressing the TLS, similar to the phonons in condensed matter systems. Hence, the optimum values of the coefficients f_k are determined variationally.

The operators transform as

$$U_p^\dagger \sigma^z U_p = \sigma^z U_p^2 = e^{-2\sum_k f_k^2} \sigma^z e^{-2\sigma^x B^\dagger} e^{2\sigma^x B}, \tag{3.18}$$

$$U_p^\dagger a_k U_p = a_k - f_k \sigma^x, \tag{3.19}$$

and the transformed Hamiltonian becomes

$$\hat{H}_p = U_p^\dagger \hat{H} U_p = \frac{\tilde{\Delta}}{2} \sigma^z e^{-2\sigma^x B^\dagger} e^{2\sigma^x B} + \sum_{kj} \bar{H}_{kj} a_k^\dagger a_j + \sigma^x \sum_k G_k (a_k + a_k^\dagger) + E_p. \tag{3.20}$$

where

$$\tilde{\Delta} = \Delta \exp\left(-2\vec{f}^\dagger \vec{f}\right). \tag{3.21}$$

and

$$G_k = g_k - \sum_j \bar{H}_{kj} f_j \tag{3.22}$$

are the renormalized transition frequency of the TLS and the coupling strength, respectively. The constant term in the transformed Hamiltonian is

$$E_p = \sum_k \left(\sum_j \bar{H}_{kj} f_j f_k - 2 g_k f_k \right). \tag{3.23}$$

It has been shown that the ground state of the Hamiltonian in Eq. (3.20) is close to vacuum, for intermediate coupling strengths [123–125]. Therefore, the ground state energy can be approximated as $E_p - \frac{\tilde{\Delta}}{2}$, and its minimization with respect to f yields the self consistency relation

$$\vec{f} = \frac{1}{\bar{H} + \tilde{\Delta}} \vec{g}. \tag{3.24}$$

Combining the above equation with Eq. (3.22) yields the reduced coupling strength

$$G_k = \tilde{\Delta} f_k. \tag{3.25}$$

The Hamiltonian in Eq. (3.20) has terms projecting to the multi-excitation subspaces. These terms can be eliminated by expanding the exponentials in Taylor series and keeping the first two terms as follows

$$e^{-2\sigma^x B^\dagger} e^{2\sigma^x B} \simeq 1 + 2\sigma^x (B - B^\dagger) - 4B^\dagger B. \tag{3.26}$$

Using $\sigma^z \sigma^x = i\sigma^y$ and replacing Eqs. (3.25) and (3.17) in the transformed Hamiltonian, H_p, yields

$$\hat{H}_{polRWA} = \frac{\tilde{\Delta}}{2}\sigma^z - 2\tilde{\Delta}\sigma^z B^\dagger B + \sum_{kj} \bar{H}_{kj} a_k^\dagger a_j + \tilde{\Delta}[(\sigma^x + i\sigma^y)B + (\sigma^x - i\sigma^y)B^\dagger] \tag{3.27}$$

or equivalently

$$\hat{H}_{polRWA} = \frac{\tilde{\Delta}}{2}\sigma^z(1 - 4B^\dagger B) + \sum_{kj} \bar{H}_{kj} a_k^\dagger a_j + 2\tilde{\Delta}[\sigma^+ B + \sigma^- B^\dagger], \tag{3.28}$$

where we omit the constant term E_p. Note that this Hamiltonian conserves the total number of excitations in the transformed Hilbert space. So keeping the first two terms in the Taylor expansions in Eq. (3.26) is equivalent to applying rotating wave approximation to the Hamiltonian in Eq.(3.20) and keeping the terms projecting to the single-excitation subspace.

3.2.2 Results

In this section, we compare the results of time evolution via RWA, polaron transformation and MPS algorithm, for arbitrary coupling strengths. As discussed in Sec. 3.1, the Hamiltonian of a 1-D CCA coupled to a TLS with an arbitrary coupling strength can be written as

$$\hat{H} = \frac{\Delta}{2}\sigma^z + g\sigma^x(a_0 + a_0^\dagger) + \omega \sum_n a_n^\dagger a_n + J \sum_n (a_n^\dagger a_{n+1} + \text{H.c.}), \tag{3.29}$$

where we set $\Delta = \omega = 1$ and $J = 0.5$.

We consider an array of length $N = 120$ sites and an evolution time of $t = 96$ (in units of ω^{-1}). The initial state is the same as before (see Eq. (3.14)). We evolve the state using RWA with and without polaron transformation and compare the final states with the ones obtained from the MPS algorithm. Note that in the simulations using polaron-transformed Hamiltonian, we transform the initial state as $|\Psi_0\rangle \rightarrow U^\dagger|\Psi_0\rangle$ and project it to the single-particle subspace, as well. This projection causes a decrease in the 2-norm of the state, therefore we normalize the final state after the evolution.

We also transform the operators, σ^z and $a_n^\dagger a_n$ to obtain the excited-state population of the TLS and the site-based photon numbers, respectively. After the transformation we project them onto the single-excitation subspace as

$$U_p^\dagger \sigma^z U_p \simeq e^{-2\Sigma_k f_k^2} \left[\sigma^z + \sigma^+ B - \sigma^- B^\dagger - 4\sigma^z B^\dagger B\right] \tag{3.30}$$

and

$$U_p^\dagger a_n^\dagger a_n U_p \simeq (a_n^\dagger a_n + |f_n|^2) - \sigma^+ f_n a_n - \sigma^- f_n a_n^\dagger. \tag{3.31}$$

In the MPS representation, each cavity and the TLS is represented by a tensor and the product of these tensors constitutes the wave function as explained in Sec. 2.2. The tensor corresponding to the TLS has a physical dimension, $d = 2$ due to the two states of the TLS. For the other MPS tensors, the d is the upper limit of the number of photons found in the corresponding cavity. For example, in the single-excitation subspace since each cavity has two possible states, which are the vacuum and one photon states, $d = 2$. However, when the coupling strength g is increased beyond the strong coupling regime where RWA is valid, multiple photon states contribute to the evolution. In our simulations, we increased g up to 0.4 and set $d = 7$ for efficient representation of the evolved states. We choose the time-step interval as $\Delta t = 0.005$ and the truncation tolerance as $\delta_{\textbf{trunc}} = e^{-12}$. The details of the algorithm are discussed in Ch. 2.

The site-based photon numbers, $P(n)$, and the decay of the excited-state population of the TLS, P_e, for three different coupling strengths are shown in Fig. 3.6. When the coupling is small, the results obtained from MPS and RWA (without applying polaron transformation) are in complete agreement (blue and black curves, respectively, in Fig. 3.6 (a) and (b). As the coupling strength gets higher, the MPS simulations yield

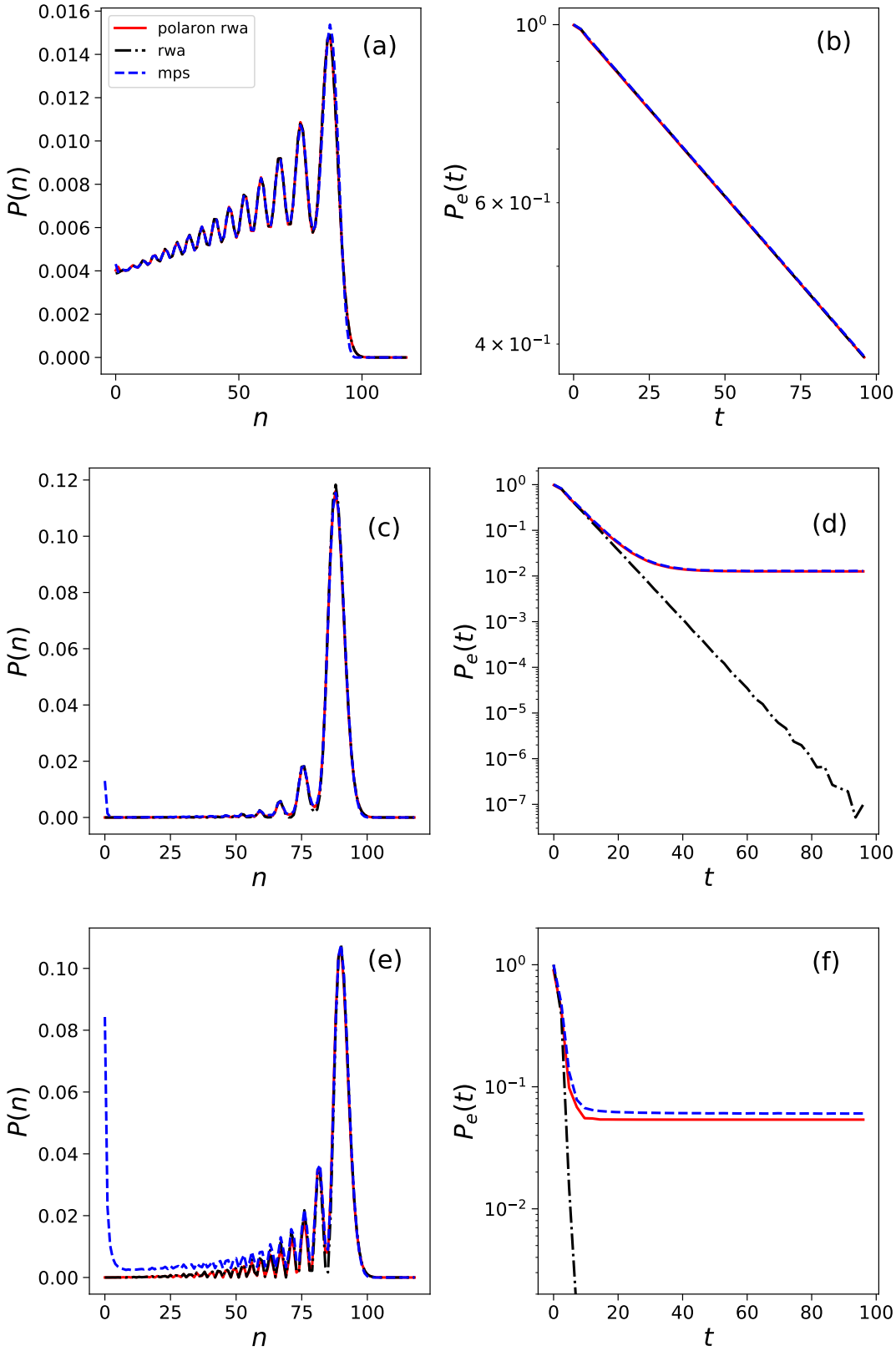

Figure 3.6 : The site-based photon numbers (left panel) at $T = 96$ and the decay of the excited state population (right panel) for $g = 0.05\omega$ (top row), $g = 0.2\omega$ (middle row) and $g = 0.4\omega$ (bottom row).

higher photon numbers near the TLS, whereas the photon numbers obtained from RWA with and without the polaron transform are approximately the same for all coupling strengths (See Fig. 3.6 left panel). The difference in MPS results may be due to the photon cloud bound to the TLS as observed in dressed states. Although the polaron transformation aims to capture the same effect, our results do not reflect this due to our numerical method. We have eliminated the terms projecting to multi-excitation subspace to limit the size of the effective Hilbert space. A computation taking into account states with higher number of excitations may yield more consistent results with the ones obtained from MPS simulations.

For $g = 0.2\omega$, P_e obtained from the MPS and the evolution with polaron transformation are in good agreement (See Fig. 3.6 (d)). They both yield slower decay compared to the exponential decay resulting from RWA without the polaron transformation. In the latter case, the excitation of the TLS is completely transferred to the photons and P_e converges to zero. However, P_e obtained from both the MPS and evolution with the polaron transformation converge to the same non-zero value. For higher coupling strengths, the MPS result deviates from the result obtained using polaron transformation in the long-time limit, converging to a higher value (See Fig. 3.6 (f)).

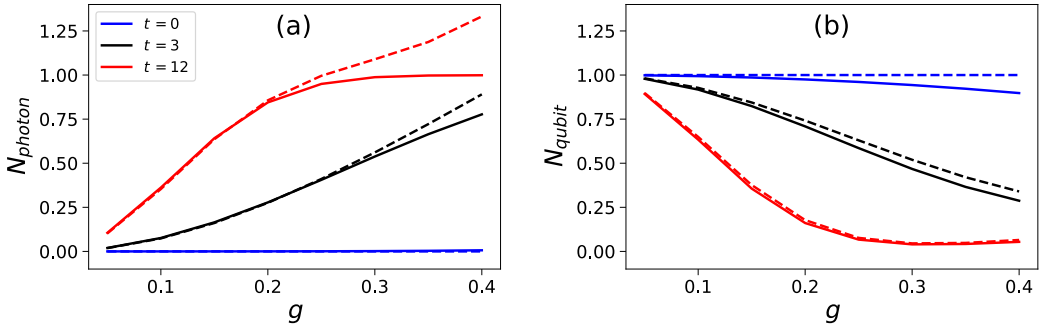

Figure 3.7 : Number of photonic (a) and qubit (b) excitations as a function of g, for different times t. The dashed curves represent MPS results, whereas continuous curves represent results obtained using polaron transform.

Fig. 3.7 shows the number of excitations as a function of g at different time steps. Here, the dashed curves represent MPS results, whereas continuous curves represent results obtained using RWA with polaron transformation. Initial values for the polaron transformation results (blue continuous curves) indicate the effects of the polaron transformation only. For the photonic excitations (Fig. 3.7 (a)), the initial number of excitations are approximately zero for all the coupling strengths as expected. As the

time evolution proceeds the two results deviate from each other for $g > 0.2\omega$ and the deviation becomes more significant for larger times. In contrast, the initial difference in P_e resulting from the two methods (Fig. 3.7 (b)) becomes significant for coupling strengths $g > 0.2\omega$. However, the results approach to each other in time and coincide at $t = 12$ (see dashed and continuous curves in Fig. 3.7 (b)).

3.3 Summary

In this chapter, we studied few photon dynamics in a 1-D CCA and compared our results obtained by different methods.

One of our main objectives is to implement an efficient absorbing boundary condition to simulate long-time dynamics. Studying an unbounded quantum system on a numerical grid in the long-time limit is computationally challenging due to the limited memory of computers. One of the methods to make the grid small enough for efficient simulation is to implement absorbing boundary conditions. We have introduced a simple ABC in the form of an imaginary potential with two parameters, namely absorption strength and absorption length. We have studied the optimum intervals for these parameters which cause minimum distortion in the interior region of a CCA in the strong coupling regime. Our simulations have shown that in the linear dispersion regime, the distortion error decreases as the product of absorption strength and absorption length increases, for small absorption parameters. However, for sufficiently large absorption strengths, the distortion error due to the absorption depends mostly on the absorption length. This shows that in this parameter regime, the main cause of distortion is the reflection of the waves with wavelengths comparable to or longer than the absorption length [88]. Similarly, the distortion error increases with the detuning, in general, due to the varying wavelengths of the photons near the band edges.

Another objective of this chapter is applying the Matrix Product States Formalism to a 1-D CCA. For this reason, we first calibrated the time step interval, Δt, and tested the Suzuki-Trotter decomposition for the spin-boson model in the strong coupling regime and under ABC. We have analyzed the computational error due to Δt by evolving the same initial state using exact diagonalization with and without Suzuki-Trotter decomposition and comparing the 2-norm difference between the final states for different values of Δt. We have found that the scaling between Δt and

the computational error is similar to the the tight-binding model with random nearest neighbor interactions that we have shown in the last chapter (See Fig. 2.4). Namely, the error increases linearly with Δt for the first order Suzuki-Trotter decomposition and quadratically for the second order.

Finally, we have applied our MPS algorithm to this model in different coupling regimes and compared our results obtained from RWA with and without polaron transform. We focused our attention on the decay of the TLS from its excited state, $P_e(t)$, and the resulting site-based photon numbers, $P(n)$. For small enough coupling strengths where RWA is applicable, $g < 0.1\omega$, $P(n)$ obtained from three different methods are in good agreement and $P_e(t)$ decays exponentially with the same rate for all three methods. For the intermediate coupling strengths, $0.1 < g/\omega < 0.2$, $P_e(t)$ obtained from both the MPS algorithm and RWA with polaron transformation decays slower compared to the results obtained from RWA without polaron transformation, and it converges to a non-zero value. $P(n)$ obtained from all three methods is the same in general, except the MPS algorithm yields higher photon numbers in the vicinity of the TLS. This is consistent with the assumption that in the intermediate coupling strengths a polaron-like dressed state composed of the TLS and the surrounding photonic cloud is formed. Although RWA approximation with the polaron transformation yields the same $P_e(t)$ as the MPS algorithm, it fails to capture the effect of the dressed state on $P(n)$. This may be due to the elimination of the terms projecting to multiple-excitation subspaces in Eq. (3.20). Keeping more terms after the polaron transformation may improve the results. As g is increased further, the behaviors of $P(n)$ and $P_e(t)$ do not change for the simulations using RWA with and without polaron transformation in general. In contrast, MPS results deviate more from the RWA results in the sense that the photonic cloud around the TLS expands over a broader region and $P_e(t)$ converges to a higher value.

4. QUANTUM WALK WITH A SINGLE PHASE IMPURITY[1]

In this chapter, we analyze non-Markovianity for the discrete-time quantum walk along a line with a single impurity at the origin. In particular, we examine the relationship between non-Markovianity and emerging bound states depending on the impurity's phase angle. In Sec. 4.1, we briefly discuss the motivation behind studying open quantum systems and the emerging interest in revealing the connection between localization and non-Marvoianity. We review the quasi-energy spectrum and sublattice symmetry of the discrete-time quantum walk in Sec. 4.2. We then move on to the quantum walk with a single phase impurity. We find the bound states by a transfer matrix approach and examine their properties in Sec. 4.3. In Sec. 4.4, we compare the localization of the bound states and the dynamical localization resulting from the time evolution. We point out the differences between the outcomes of the two non-Markovianity measures, which are based on state distinguishability and system-ancilla entanglement, in relation with the emergence of bound states in Sec. 4.5. We present a discussion of our results and conclude in Sec. 4.6.

4.1 Introduction

The theory of open quantum systems provides the necessary means to study and characterize the dynamics of quantum systems that are interacting with their surrounding environments [11]. It is well known that although closed systems evolve in time unitarily, dynamics of open quantum systems is no longer unitary due to the coupling to their environments. Such an interaction between the principal open system and the environment typically results in decoherence of the principal system, resulting in the loss of characteristic quantum properties such as coherent phase relations. From the standpoint of dynamical memory effects, time evolution of open quantum systems can be classified as exhibiting Markovian (memoryless) or non-Markovian behaviour.

[1]This chapter is based on the paper Danacı, B., Karpat, G., Yalçınkaya, İ. and Subaşı, A. (2019). Non-Markovianity and bound states in quantum walks with a phase impurity, *Journal of Physics A: Mathematical and Theoretical*, *52*(22), 225302.

As a consequence of the increasing experimental control over quantum systems and the development of reservoir engineering techniques in recent years, the study of quantum non-Markovianity has become a significant line of research [126, 127]. Various methods have been introduced for quantifying and characterizing the non-Markovian behaviour in the dynamics of open quantum systems. Among others, the approaches based on the information dynamics between the open system and its environment have become prominent [128–132]. The motivation behind these approaches is when information flows from the environment back to the system throughout the dynamics, the future states of the open system might depend on its earlier states.

The connection between localization and non-Markovianity has been studied in different settings, such as atomic impurities embedded in a disordered coupled cavity array [133], in a quasi periodic Fermi lattice [134] and in a Bose Hubbard lattice [135]. These studies show that non-Markovian memory effects emerge as excitations localize in the vicinity of the impurity. In quantum walks, non-Markovian effects can be analyzed without considering an extra external environment. Similar to the coin throw in classical random walks, an internal degree of freedom, so-called "coin", determines the direction of the quantum walk. Non-Markovianity can be studied focusing on the coin space reduced dynamics where the spatial degree of freedom is traced out [136]. In that case, the position space itself is treated as the environment of the coin space. Even though this reduced dynamics is known to be non-Markovian for the standard quantum walk, the presence of decoherence in the form of broken links wipes out the non-Markovian behaviour and gives rise to a Markovian process. On the other hand, it has also been shown that the non-Markovian behaviour can be enhanced when the walker is subjected to some specific static or dynamic disorder [137].

Despite their superiority over random walks in spreading rates [45, 46] leading to faster computational algorithms [47], quantum walks have also attracted considerable attention in terms of their non-diffusibility features in the presence of disorder such as quantum-to-classical transition [138], dynamical localization [139, 140], and the emergence of bound states [141, 142]. While rolling back to the classical behavior is attributed to wiping out coherence in the system due to dynamical disorder, it is the static disorder that leads to dynamical localization in quantum walks. The former disorder scheme manifests itself as a time-dependent evolution operator,

whereas the latter resembles a random potential for the quantum walker described by a unitary operator [143–149]. Since these disorder models break either the temporal or the spatial symmetries, any emergent non-diffusibility in quantum walks is typically associated with a lack of some symmetry in the dynamics [150–154]. Other examples of non-diffusibility have been observed in quantum walks coupled to spin environments [155, 156]. In this chapter, we consider a quantum walk with a static phase impurity [141, 142] and study its localization and non-Markovianity properties.

4.2 Discrete-time Quantum Walk

Analogous to the classical random walk, the discrete-time quantum walk depicts the unitary evolution of a particle on a lattice where the direction of the movement is determined by an internal degree of freedom, namely, the coin [44]. At each time step, an operator $\hat{C}$ acting solely on the coin state is followed by a coin-state-conditioned translation operator $\hat{T}$ acting on the total coin-position Hilbert space $\mathcal{H}_c \otimes \mathcal{H}_p$. Although $\hat{C}$ can be chosen from $SU(2)$, without loss of generality, one may constrain the coin operator to be a rotation around the x-axis [157], so that

$$\hat{C} = \exp\left(-i\theta\hat{X}\right) \otimes \hat{I}_N. \tag{4.1}$$

Here, $\hat{X}$ is the Pauli-X operator acting on the coin space and $\hat{I}_N$ is the identity operator acting on the the N-dimensional position space. We will fix the coin angle to be $\theta = \pi/4$ throughout the thesis. The conditional translation operator shifts the position of the walker one site to its right or left depending on the coin state as given by

$$\hat{T} = \sum_{c,n} |c\rangle\langle c| \otimes |n + (-1)^c\rangle\langle n|, \tag{4.2}$$

where $c \in \{0, 1\}$ refer to the eigenstates of the Pauli-Z operator $\hat{Z}$ spanning the coin space and $n \in \mathbb{Z}$ labels the N position states. Thus, the evolution operator describing a single time step is written as $\hat{W} = \hat{T}\hat{C}$. After t steps, the final state becomes

$$|\Psi_t\rangle = \hat{W}^t|\Psi_0\rangle = \sum_{c,n} a_{c,n}(t)|c, n\rangle, \tag{4.3}$$

where $|\Psi_0\rangle$ is an arbitrary initial state at $t = 0$ and $a_{c,n}(t)$ are the probability amplitudes corresponding to coin state $|c\rangle$ and position state $|n\rangle$. Consequently, the probability of finding the quantum walker at position n and step t is calculated by $P_n(t) = \sum_c |a_{c,n}(t)|^2$.

4.2.1 Quasi-energy spectrum

The walk can also be considered as a stroboscopic simulation of a quantum evolution generated by an effective Hamiltonian $\hat{H}_\theta$ such that $\hat{W}_\theta \equiv \exp(-i\hat{H}_\theta)$, where we assume that the time required for taking one step and $\hbar$ are both set to unity [63, 64]. It is well-known that the spectrum of this Hamiltonian has a band structure with a period of 2π, which arises from the discrete time-translation symmetry of the walk, i.e., the Hamiltonian is in fact a representative of a recurring single-step evolution.

The energy eigenvalues E here are called quasi-energies, similar to the quasi-momentum k showing up due to discrete spatial translation symmetry of $\hat{W}_\theta$ in the standard quantum walk by a unit lattice spacing. The standard walk Hamiltonian becomes diagonal in this quasi-momentum basis via the transformation $|c,k\rangle = \frac{1}{\sqrt{2\pi}}\sum_n \mathrm{e}^{-\mathrm{ikn}}|c,n\rangle$ with $k \in [-\pi,\pi]$ and one obtains the dispersion relation $\cos E(k) = \pm\cos\theta\cos k$, where k is in units of $\hbar$ over the lattice spacing.

We will study the non-Markovian behaviour from the point of view of the coin sub-system, which will be considered as an open system with the position space interacting with it as the environment [136]. Therefore, the time evolution of the coin density matrix will be investigated. Since the stationary states of the standard quantum walk are product states of the form $|E_k\rangle = |\chi_k\rangle \otimes |k\rangle$, the reduced pure coin density matrix can be written as $\rho_k^{\mathrm{coin}} = |\chi_k\rangle\langle\chi_k| = (I_2 + \vec{r}_k \cdot \sigma)/2$, where [64]

$$\vec{r}_k = \frac{1}{\sin E(k)}(\cos k \sin\theta, -\sin k \sin\theta, -\sin k \cos\theta). \tag{4.4}$$

4.2.2 Sublattice symmetry

Two quasi-energy bands associated with the coin states are symmetric about $E = 0$ and the band gap closes for $\theta = 0$ or π. Any pair of eigenstates with a quasi-energy difference of π can be associated with one another via the sublattice operator

$$\hat{S} = \hat{I}_2 \otimes \sum_n (-1)^n |n\rangle\langle n|, \tag{4.5}$$

which is both unitary and Hermitian, i.e., $\hat{S}^2 = \hat{I}_{2N}$ [158]. Thus, for each eigenstate $|E\rangle$ of $\hat{H}_\theta$ with quasi-energy E in a given band, there exists another eigenstate $\hat{S}|E\rangle$ with quasi-energy $E + \pi$ in the other band, which can actually be deduced directly using

(4.5),

$$\hat{S}\hat{W}_\theta\hat{S} = -\hat{W}_\theta \;\; \Rightarrow \;\; \hat{S}\hat{H}_\theta\hat{S} = \hat{H}_\theta + \pi. \tag{4.6}$$

The sublattice operator has two degenerate eigenvalues ± 1 such that eigenstates corresponding $+1$ (-1) parity, which we will denote by $|S_e\rangle$ ($|S_o\rangle$), occupy only even (odd) labelled sites in the position space. These eigenstates can also be written in terms of the symmetric (for $+1$) and anti-symmetric (for -1) superpositions of $|E\rangle$ and $\hat{S}|E\rangle$ such that

$$|S_{e,o}\rangle = |E\rangle \pm \hat{S}|E\rangle. \tag{4.7}$$

Note that the step operator $\hat{W}_\theta$ transforms $|S_e\rangle$ to $|S_o\rangle$, or vice versa, up to an overall phase of $\mathrm{e}^{-\mathrm{iE}}$. Therefore, if one initializes the walk with either of $|\Psi_0\rangle = |S_{e,o}\rangle$, the total state will oscillate from one to the other forever, i.e., step operator moves the state back and forth between two sublattices. It is worth mentioning here that this periodic oscillation with a period of 2 will play an important role in our discussion of non-Markovianity.

4.3 Quantum Walk with a Phase Impurity

We consider a modified version of the standard quantum walk such that whenever the walker passes through the origin $n=0$, it acquires a phase of $\mathrm{e}^{\mathrm{i}\phi}$ as illustrated in Fig. 4.1. This effect can be introduced to the step operator by rewriting it as $\hat{W}'_\theta = \hat{T}\hat{C}_\theta\hat{P} \equiv \mathrm{e}^{-\mathrm{i}\hat{\mathrm{H}}'_\theta}$ to include the phase operator

$$\hat{P} = \hat{I}_2 \otimes \sum_n \mathrm{e}^{\mathrm{i}\phi_\mathrm{n}}|n\rangle\langle n|, \tag{4.8}$$

where $\phi_n = \phi\,\delta_{n,0}$ and $\delta_{n,m}$ denotes the Kronecker delta function. This model was studied by Wojcik et al. and the bound eigenstates of the double step operator $\hat{W}'^2_\theta$ are obtained [141]. We will provide an alternative solution for the stationary bound states in this model for the single step operator $\hat{W}'_\theta$ using a transfer matrix approach [159]. We note that a double step operator would be useless in our case since it restricts the evolution to one of the sublattices, and hence, no oscillation takes place between $|S_{e,o}\rangle$ and $|S_{o,e}\rangle$ contrary to the discussion we will have, where these oscillations lie at the center of non-Markovian behaviour.

The phase operator $\hat{P}$ breaks the translation invariance of the step operator $\hat{W}'_\theta$ in the considered model. However, we can still employ the reflection symmetry which is

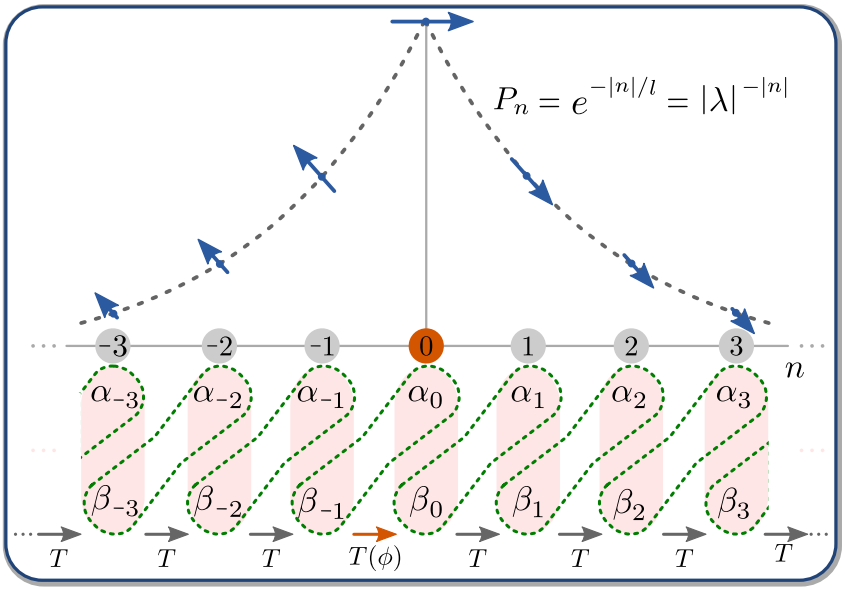

Figure 4.1 : Schematic representation of a bound state and its probability distribution over the position space. The walker acquires a phase $e^{i\phi}$ due to the impurity at the origin. As given in (4.11), the coefficients (α_n, β_{n-1}) are related to each other by transfer matrices T and $T(\phi)$ for $n \neq 0$ and $n = 0$, respectively. The localization length l is determined from eigenvalue λ of the transfer matrix T. Blue arrows represents the coin state in the phase space and their lengths are drawn proportional to P_n.

introduced by the reflection operator

$$\hat{R} = \sigma_x \otimes \sum_n |-n\rangle\langle n|, \tag{4.9}$$

in finding the stationary states of $\hat{H}'_\theta$ as follows. Similar to the sublattice operator, $\hat{R}$ also has the property $\hat{R}^2 = \hat{I}_{2N}$ and it possesses two degenerate eigenvalues ± 1. Also, by considering the commutation relations that $[\hat{R}, \hat{H}'_\theta] = 0 = [\hat{R}, \hat{S}]$, eigenstates of $\hat{H}'_\theta$ can be labelled by a definite $\pm$ parity, i.e. $\hat{R}|E^\pm\rangle = \pm|E^\pm\rangle$, and application of $\hat{S}$ does not change this parity and it yields the eigenstates with quasi-energies $E^\pm + \pi$ since the condition (4.6) is still valid for $\hat{W}'_\theta$. These energy eigenstates can be written in the component form

$$|E^\pm\rangle = \sum_n \alpha_n^\pm |\uparrow, n\rangle + \beta_n^\pm |\downarrow, n\rangle, \tag{4.10}$$

where the coefficients obey the constraint $\alpha_{-n}^\pm = \pm\beta_n^\pm$ as a direct consequence of the reflection symmetry. Thus, $|E^\pm\rangle$ can be constructed by knowing only half of their components. Also, by using $\hat{W}'_\theta|E^\pm\rangle = \exp(-iE^\pm)|E^\pm\rangle$, one can obtain the recursion relations between these coefficients and rearrange them in the following way

$$\begin{pmatrix} \alpha_{n+1}^\pm \\ \beta_n^\pm \end{pmatrix} = T(\phi_n) \begin{pmatrix} \alpha_n^\pm \\ \beta_{n-1}^\pm \end{pmatrix}. \tag{4.11}$$

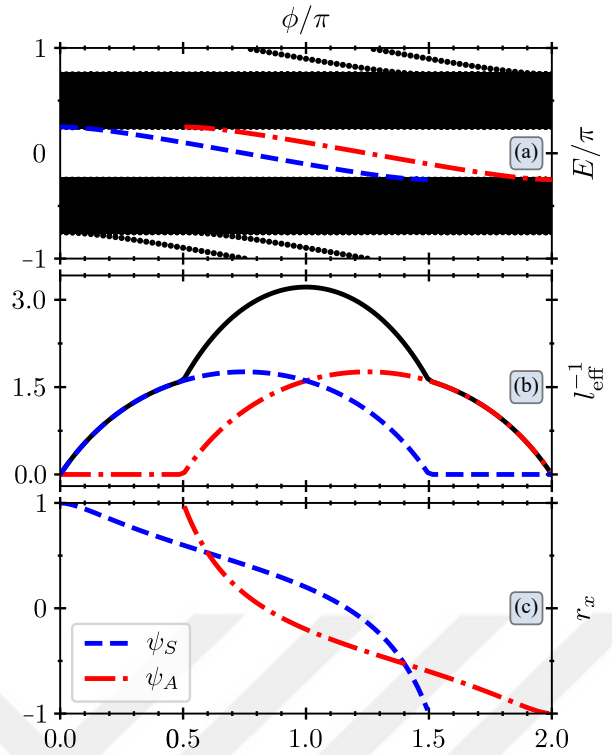

Figure 4.2 : (a) Energy band diagram of the walk ($\theta = \pi/4$) as a function of the phase parameter ϕ, where $\phi = 0$ corresponds to the standard quantum walk. The analytic result given in (4.16) is drawn for reflection symmetric (blue dashed) and anti-symmetric (red dot-dashed) bound state quasi-energy values, where the numerical values (black dots) are omitted since they exactly coincide with the analytic result. (b) Inverse localization length of reflection symmetric (blue dashed) and anti-symmetric (red dot-dashed) energy eigenstates and their sum as the effective inverse localization length (solid black) as a function of ϕ, which is used as a measure of localization. (c) Reduced coin density matrix parameter r_x for reflection symmetric (blue dashed) and anti-symmetric (red dot-dashed) bound states as a function of ϕ gives average value about which oscillations in the reduced density matrix take place.

Here, the matrix $T(\phi_n)$ is called the transfer matrix for site n and it connects the adjacent coefficients in (4.10) (See Fig. 4.1), which is given in general as

$$T(\phi_n) = \begin{pmatrix} e^{i(E^{\pm}+\phi_n)} \sec\theta & -i\tan\theta \\ i\tan\theta & e^{-i(E^{\pm}+\phi_n)} \sec\theta \end{pmatrix}, \tag{4.12}$$

with the inverse $T^{-1}(\phi_n) = \sigma_x T(\phi_n)\sigma_x$. Reflection symmetry implies $T(\phi_{-n}) = \sigma_x T^{-1}(\phi_n)\sigma_x = T(\phi_n)$ and thus $\phi_n = \phi_{-n}$. Since $\phi_n = \phi\,\delta_{n,0}$ in our model, we set $T(\phi_n = 0) = T$ for $n \neq 0$. Now, the problem of finding the stationary states is boiled down to determine a suitable pair $(\alpha_1^{\pm}, \beta_0^{\pm})^T$ in (4.10) satisfying the reflection property. We can look for stationary states whose coefficients as simultaneous eigenvectors of the transfer matrices must satisfy

$$T(\phi)\sigma_x \begin{pmatrix} \alpha_1^{\pm} \\ \beta_0^{\pm} \end{pmatrix} = \pm \begin{pmatrix} \alpha_1^{\pm} \\ \beta_0^{\pm} \end{pmatrix} \text{ and } T \begin{pmatrix} \alpha_n^{\pm} \\ \beta_{n-1}^{\pm} \end{pmatrix} = \lambda \begin{pmatrix} \alpha_n^{\pm} \\ \beta_{n-1}^{\pm} \end{pmatrix} \tag{4.13}$$

such that

$$\begin{pmatrix} \alpha_{n+1}^{\pm} \\ \beta_n^{\pm} \end{pmatrix} = \lambda^n \begin{pmatrix} \alpha_1^{\pm} \\ \beta_0^{\pm} \end{pmatrix}, \qquad n \geq 1. \tag{4.14}$$

In the infinite chain limit, vanishing boundary conditions impose that $|\lambda| < 1$ for bound states and matching the two forms

$$\begin{aligned} \begin{pmatrix} \alpha_1^{\pm} \\ \beta_0^{\pm} \end{pmatrix} &= C(E^{\pm}) \begin{pmatrix} \sin\theta \\ \sin(E^{\pm}) - i\sqrt{\sin^2\theta - \sin^2(E^{\pm})} \end{pmatrix}, \\ \begin{pmatrix} \alpha_1^{\pm} \\ \beta_0^{\pm} \end{pmatrix} &= C(E^{\pm}) \sin\theta \begin{pmatrix} e^{i(E^{\pm}+\phi)} \\ \pm e^{\pm i\theta} \end{pmatrix} \end{aligned} \tag{4.15}$$

gives the quasi-energy

$$E^{\pm} = \cot^{-1}\left(\pm \frac{1 - \sin(\theta \mp \phi)\sin\theta}{\sin\theta\cos(\theta \mp \phi)} \right), \tag{4.16}$$

provided that

$$\sin\left(E^{\pm} + \phi \mp \theta\right) = \pm \frac{\sqrt{\sin^2\theta - \sin^2 E^{\pm}}}{\sin\theta}. \tag{4.17}$$

The normalization constant is given by $|C(E^{\pm})|^2 = \left(1 - \lambda(E^{\pm})^2\right)/2$ with the transfer matrix eigenvalue

$$\lambda_{\pm} = \lambda(E^{\pm}) = \frac{1}{\cos\theta}\left(\cos(E^{\pm}) - \sqrt{\sin^2\theta - \sin^2(E^{\pm})} \right). \tag{4.18}$$

It is seen that $|\lambda_{\pm}| \leq 1$ provided that $|\sin E^{\pm}| \leq |\sin\theta|$. When a solution with definite parity and an eigenvalue $-\theta < E^{\pm} < \theta$ exists, then there is a sublattice symmetric solution, which has $\lambda_{\pm} \to -\lambda_{\pm}$ and $\begin{pmatrix} \alpha_1^{\pm} \\ \beta_0^{\pm} \end{pmatrix} \to \hat{S} \begin{pmatrix} \alpha_1^{\pm} \\ \beta_0^{\pm} \end{pmatrix}$, with the same parity and shifted eigenvalue $-\theta + \pi < E^{\pm} < \theta + \pi$. The combinations of the sublattice symmetric pairs of reflection symmetric states, for example, give $\left|S_{e,o}^{+}\right\rangle = |E^{+}\rangle \pm |E^{+} + \pi\rangle$ which are supported on even/odd sites. Similar combinations $\left|S_{e,o}^{-}\right\rangle$ exist for reflection anti-symmetric bound states.

The reflection symmetric bound states exist only in the interval $\phi \in (0, 2\pi - 2\theta)$ and the reflection anti-symmetric bound states exist for $\phi \in (2\theta, 2\pi)$. The quasi-energies are shown with blue dashed and red dot-dashed lines in the quasi-energy diagram as a function of ϕ in Fig. 4.2(a) for $\theta = \pi/4$, which corresponds to balanced walks. The numerical solution is performed for a large lattice with periodic boundary conditions and the results are indistinguishable on this scale from the quasi-energies of the bound states determined from the eigenvalues of the transfer matrix.

We would like to quantify the localization in our model as a function of the impurity phase ϕ. For this purpose one of the quantities we calculate is an effective inverse localization length ℓ_{eff}^{-1} which is the sum of the inverse localization lengths over all energy eigenstates. Since the localization length diverges for an extended state in the infinite chain limit, extended states' contribution to ℓ_{eff}^{-1} also vanishes in that limit and we are left with only the inverse localization lengths of the bound states given by the eigenvalues of the transfer matrix, i.e. $\ell^{-1} = \ln \lambda$. Therefore, the sum of ℓ^{-1} over all stationary states is determined by the number of bound states and their localization lengths. The total ℓ_{eff}^{-1} (solid black curve) is plotted in Fig. 4.2(b) as a function of ϕ, where the individual contributions of symmetric (blue dashed) and anti-symmetric (red dot-dashed) bound states are also shown. The localization length of a bound state is minimum when its quasienergy is at the center of the band gap (see (4.18)), so that the reflection symmetric and anti-symmetric bound states become maximally localized when $\phi = 3\pi/4$ and $\phi = 5\pi/4$, respectively. The total ℓ_{eff}^{-1} is symmetric about $\phi = \pi$ where it attains its maximum value. Although it monotonically decreases towards both sides of $\phi = \pi$, kinks in ℓ_{eff}^{-1} occur at $\phi = \pi/2$ ($\phi = 3\pi/2$) at the (dis)appearance of new bound states as ϕ increases from 0 to 2π.

Unlike the homogeneous quantum walk, in the presence of phase impurity the energy eigenstates become entangled in the composite coin-position space in this model and ρ^{coin} becomes a mixed state. Furthermore, the y- and z-components of the density matrix vector $\vec{r}$ become zero for all energy eigenstates (see (4.4) for the standard walk). Here, we note the x-components of the reflection symmetric and anti-symmetric bound states

$$r_{x,\pm} = \pm\frac{1}{2}\left[2\lambda_{\pm}\cos\left(E^{\pm} + \phi \mp \frac{\pi}{4}\right) + \left(1 - \lambda_{\pm}^{2}\right)\right]. \tag{4.19}$$

As ϕ changes, r_x changes from $+1$ to -1 for both the symmetric and anti-symmetric bound states over the regions of their existence as shown in Fig. 4.2(c). (Since the action of the unitary sublattice operator on the coin space is trivial, sublattice symmetric bound state give the same ρ^{coin}.) At $\phi \sim 0.6\pi$ and $\phi \sim 1.4\pi$, the difference in $r_{x,\pm}$ becomes zero, which means the two coin states become indistinguishable for bound states of either parity.

4.4 Dynamical Localization

We commence this section by presenting our results for time evolving states in balanced quantum walks ($\theta = \pi/4$) making connection to the stationary bound states obtained in the previous section. In general, the dynamical properties resulting from the evolution of the quantum walk depend on the initial state. We consider initial states such as $|\Psi_0\rangle = |\psi_c\rangle \otimes |0\rangle$ which are localized at the origin, for examining the effects due to the existence of bound states around the origin. Here, $|\psi_c\rangle$ is the initial coin state and the reflection symmetry of $|\Psi_0\rangle$ is defined by the symmetry of $|\psi_c\rangle$ under rotation by π about the x-direction. For our purposes, we choose to concentrate on the reflection symmetric and anti-symmetric initial states whose coin subsystems are the eigenstates of σ_x, i.e., the initial states $|\Psi_{\rm S}\rangle = \frac{1}{\sqrt{2}}[|\uparrow\rangle + |\downarrow\rangle] \otimes |0\rangle$ and $|\Psi_{\rm A}\rangle = \frac{1}{\sqrt{2}}[|\uparrow\rangle - |\downarrow\rangle] \otimes |0\rangle$, respectively. Time evolution starting from these states yields symmetric probability distributions about the origin independent of the presence of a phase impurity. For example, in case of $|\Psi_0\rangle \equiv |\Psi_{\rm A}\rangle$, Fig. 4.3(a) shows the probability distribution in position $P_n(t)$ at $t = 300$ for all ϕ values. The significance of the reflection anti-symmetric bound state for a given ϕ becomes clear when we compare the degree of localization and the overlap of the initial state with the corresponding bound states $|E^-\rangle$. For an arbitrary initial coin state $|\psi_c\rangle = \cos\frac{\gamma}{2}|\uparrow\rangle + e^{i\eta}\sin\frac{\gamma}{2}|\downarrow\rangle$, this overlap is given by

$$F^{\rm bound}_{\gamma,\eta} \sum_{E\in\{E_{\rm bound}\}} |\langle E|\Psi_t\rangle|^2 \frac{(2-\lambda_+^2-\lambda_-^2)-(\lambda_+^2-\lambda_-^2)\sin\gamma\cos\eta}{2} \tag{4.20}$$

For our selection of initial coins, (4.20) simplifies to $F^{\rm bound}_{\pm\pi/2,0} = 1-\lambda_\pm^2$. The localization region apparent in Fig. 4.3(a), when $\phi \in (\pi/2, 2\pi)$, is directly related with $F^{\rm bound}_{-\pi/2,0}$ shown in Fig. 4.3(b). The walker is most localized when the overlap becomes maximum at $\phi = 5\pi/4$. Similarly, in the interval $\phi \in (0, \pi/2)$ the overlap with the bound subspace is zero and the probability distribution has a dip around the initial site. Four representative probability distributions for different ϕ values are shown in detail in Fig. 4.3(c). For the standard quantum walk $\phi = 0$, the probability distribution is uniform in the middle region and there are two peaks near the edges which move in opposite directions with constant speed. For any ϕ, the resulting probability distribution spreads balistically in the position space, i.e., it's variance is proportional

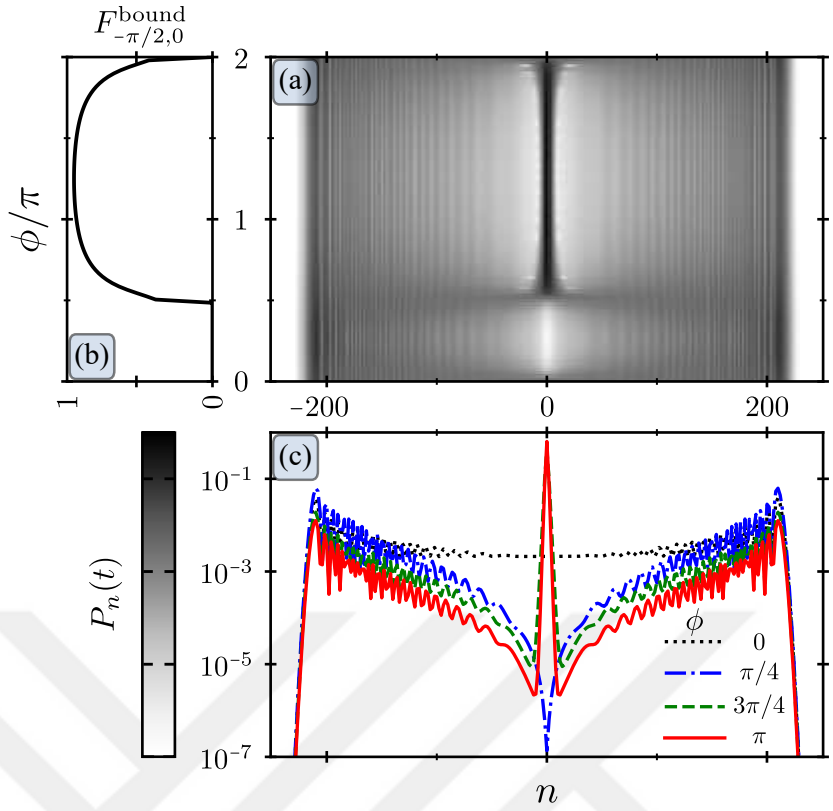

Figure 4.3 : (a) The probability distribution $P_n(t)$ of the walk after 300 steps for the reflection anti-symmetric initial state $|\Psi_A\rangle$ as a function of the impurity phase angle ϕ. (b-c) Depending on the overlap $F^{\text{bound}}_{-\pi/2,0}$ between $|\Psi_A\rangle$ and bound states, the probability distribution can have a peak or a dip at the starting site of the walker.

to t^2. However, the proportionality constants may vary depending on the amount of localization, and hence, on ϕ.

The average probability distribution of the walk $\langle P_n(t)\rangle$ is obtained by averaging $P_n(t)$ over all possible initial coin states. However, we observe that we get exactly the same result by only taking into account any pair of orthogonal coin states. This is due to the fact that the average probability distribution resulting from two walks starting with any two orthogonal coin states at the origin is equal to the one resulting from the evolution of a completely mixed coin state. (The resulting distribution is symmetric since the completely mixed coin state at the origin is reflection invariant.) Also, for the long-time limit, the bound states stay in the vicinity of the origin, whereas the extended states get spread over the infinite position space yielding probabilities going to zero. Based on these facts, we can obtain an analytic expression to estimate the long-time behaviour of $\langle P_n(t)\rangle$ by projecting the evolved state onto the bound subspace and averaging the

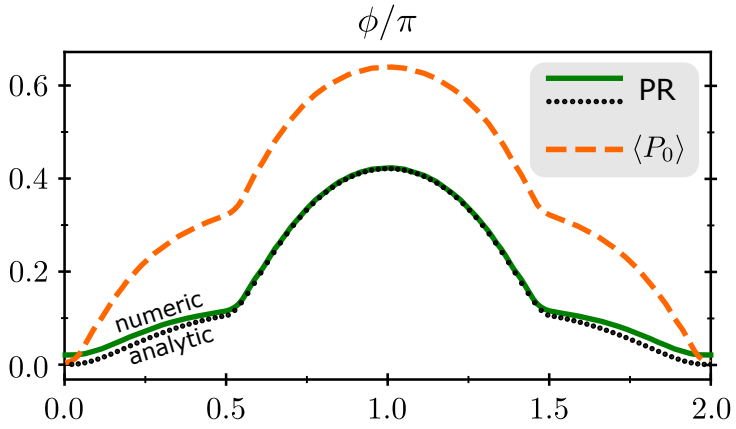

Figure 4.4 : The numerical results for the participation ratio (PR) and the average probability at the origin $\langle P_0 \rangle$ with respect to ϕ after 150 steps. The analytical prediction for PR (black dots) is also provided.

corresponding probabilities over two orthogonal initial states, such that

$$\langle P_0 \rangle = \frac{1}{2}\left[(1-\lambda_+^2)^2+(1-\lambda_-^2)^2\right] \text{ and} \tag{4.21}$$

$$\langle P_n \rangle = \frac{1}{4}[\lambda_+^{2|n|-2}(1+\lambda_+^2)(1-\lambda_+^2)^2\lambda_-^{2|n|-2}(1+\lambda_-^2)(1-\lambda_-^2)^2], \tag{4.22}$$

where $n \neq 0$ and non-zero probabilities appear for even (odd) sites only after even (odd) number of steps. To quantify the localization, we utilize the participation ratio of the averaged probability distribution, which is given by

$$\text{PR} = \sum_n \langle P_n(t) \rangle^2 . \tag{4.23}$$

For a uniform probability distribution over N sites, PR yields its minimum value $\sim N^{-1}$. At the other extreme of localization at one site, PR takes its maximum value of one. In Fig. 4.4, the numeric results for the PR (green solid curve) and $\langle P_0 \rangle$ (orange dashed curve) for 150 steps are represented. Both of them is calculated by using the average probability distribution $\langle P_n(t) \rangle$ which is averaged over a pair of orthogonal initial coin states as we mentioned before. We also provide the analytic prediction of PR (black dots) for the long-time behaviour using Eq. (4.22) and Eq. (4.23) which slightly differs from its numerical simulation, whereas we omitted that of $\langle P_0 \rangle$ for clarity since it exactly fits to the numerical data. First of all, both curves exhibit similar behaviour with respect to ϕ and $\langle P_0 \rangle$ pointing out that localization occurs around the impurity site. They get maximized at $\phi = \pi$ and vanish at the standard quantum walk limit $\phi = 0, 2\pi$. The kinks at $\phi = \pi/2, 3\pi/2$ are due to bound states appearing or disappearing in this model as discussed previously. This behaviour

matches exactly that of the effective localization length determined by the bound states in Fig. 4.2(b), which consequently shows that the localization properties of the walk in the long-time limit is determined by the number and character of the stationary bound states. The slight difference between the numerical and analytical results of PR stems from the finite number of time steps in the numerical simulation and the fact that contribution from the extended states is completely excluded in the analytical expression. As a consequence of this, the numerical data stays above the analytical prediction. For example, as we approach the standard walk case, the wavefunction for a finite-step walk stays relatively "localized" in comparison to that of the long-time case which spreads infinitely over the position space without any localization. Hence, the numerical prediction will become zero in the standard walk in this limit as well. The very good agreement between the numerical and analytical results in Fig. 4.4 implies that the effect of the extended states on the PR is negligible even after 150 steps.

4.5 Non-Markovianity

We now turn our attention to the non-Markovian behaviour of the dynamics of the coin for the quantum walk with a phase impurity. As mentioned before, we are interested in the effects of localized bound states and their symmetry on the degree of non-Markovianity of the reduced coin evolution. In order to quantify the amount of memory effects in the open system dynamics from different perspectives, we will comparatively study two well-established measures of quantum non-Markovianity that are based on the information flow dynamics between the coin and the spatial degrees of freedom.

Let us first briefly discuss how to characterize the non-Markovian nature of an open system evolution and identify the existence of possible memory effects in the dynamics. Assume that we have a quantum map $\Lambda(t,0)$, i.e., a completely positive trace preserving (CPTP) map describing the evolution of the open quantum system. The property of divisibility implies that divisible maps satisfy the decomposition rule $\Lambda(t,0) = \Lambda(t,s)\Lambda(s,0)$, where $\Lambda(t,s)$ is a CPTP map for all $s \leq t$. Markovian or so-called memoryless dynamical maps are recognized as the ones that satisfy this decomposition rule. On the other hand, when the divisibility rule is violated, i.e.,

when $\Lambda(t,s)$ is not a CPTP map or when it does not even exist, then the dynamical map Λ is said to be non-divisible and the evolution it describes non-Markovian. The concept of divisibility can also be discussed in the context of discrete dynamics, such as quantum walk, where $t,s \in \mathbb{N}$ [160].

4.5.1 Breuer-Laine-Piilo (BLP) measure

The first non-Markovianity measure that we utilize in our work is known as Breuer-Laine-Piilo (BLP) measure [132] which is based on the idea of distinguishability of two open system states under a given dynamical evolution. In this approach, the changes in the distinguishability between two arbitrary initial states of the open system during the dynamics are interpreted as the information flow between the open system and its environment. In particular, if distinguishability between the initial states decreases monotonically in time throughout the evolution, the dynamics is said to be Markovian, since in this case information flows from the open system to its environment in a monotonic fashion. However, if distinguishability temporarily increases during the dynamics, then this is understood as a back-flow of information from the environment to the open system giving rise to non-Markovian memory effects. The distinguishability of two systems can be quantified through trace distance between their density matrices ρ_1 and ρ_2 as

$$D(\rho_1,\rho_2)=\frac{1}{2}||\rho_1-\rho_2||_1=\frac{1}{2}\mathrm{Tr}\left[(\rho_1-\rho_2)^\dagger(\rho_1-\rho_2)\right]^{1/2} \tag{4.24}$$

which acquires its maximum value of one, when the states ρ_1 and ρ_2 are orthogonal. At this point, we should stress that since CPTP maps are contractions for the trace distance, BLP measure vanishes for divisible maps, resulting in a memoryless evolution. However, we also emphasize that it is possible for trace distance to monotonically decrease for certain non-divisible maps as well. Therefore, as is well known in the recent literature, even though widely used as a measure for non-Markovianity on its own, BLP measure is actually a witness for the non-divisibility of quantum dynamical maps. The BLP measure can be expressed in discrete time as [160]

$$\mathcal{N}=\max_{\rho_{1,2}}\sum_{t,\Delta D>0}\Delta D_t=\sum_t \Delta D_t\Theta(\Delta D_t), \tag{4.25}$$

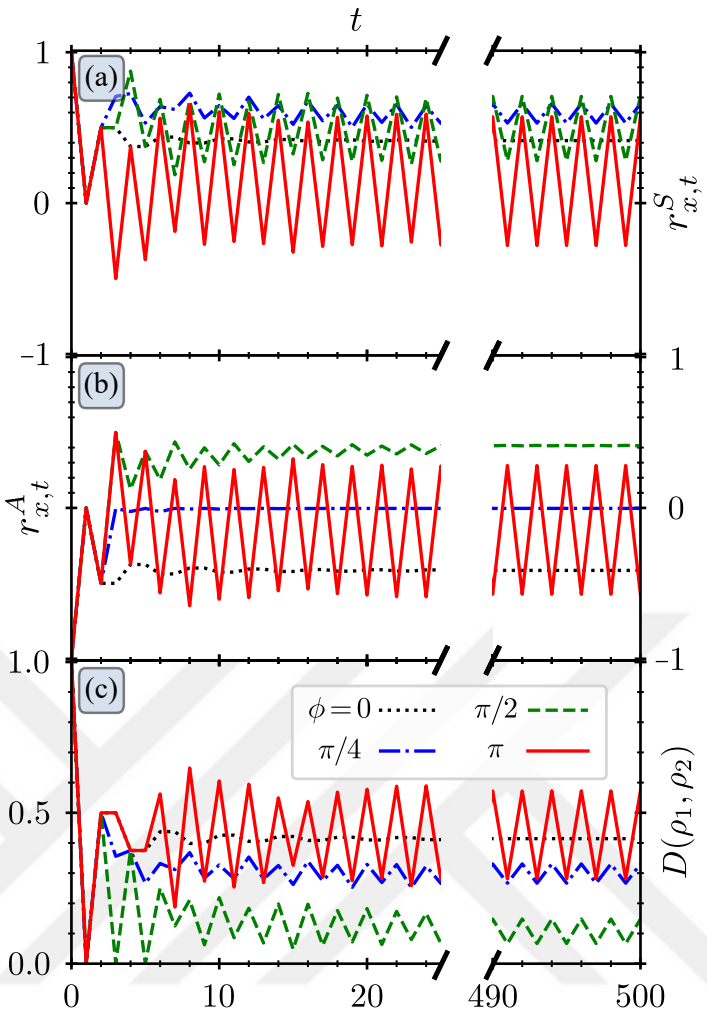

Figure 4.5 : Oscillations in the reduced coin density matrices starting from $|\Psi_S\rangle$ in (a) and from $|\Psi_A\rangle$ in (b) as a function of time for representative values of the phase parameter ϕ. The trace distance of these coin states $D(\rho_S,\rho_A) = |r_{x,A} - r_{x,S}|$ is shown in (c) and the oscillating behaviour gives rise to non-zero BLP measure.

where $\Theta(x)$ denotes the Heaviside step function,

$$\Delta D_t = D(\rho_{1,t},\rho_{2,t}) - D(\rho_{1,t-1},\rho_{2,t-1}). \tag{4.26}$$

and the maximization is carried out over all possible initial state pairs. It has been shown that the pair which maximizes the sum in Eq. (4.25) is a pair of orthogonal of states [161]. In our analysis, we study the reduced system dynamics of a pair of such initial states, namely, $|\psi_{S,A}\rangle$ introduced before, with opposite reflection symmetry, which will be later on revealed as the optimal initial state pair optimizing the BLP measure.

The time evolution of $\rho^{\text{coin}}_{S,A}$ is particularly easy to visualize because the parametrization $\rho^{\text{coin}}_t = (I + \vec{r}_t \cdot \vec{\sigma})/2$ has only one non-zero component, i.e. $r_{x,t}$, throughout the time

evolution which is shown in Fig. 4.5 for representative values of the phase ϕ. For $\phi = 0$, which gives the standart quantum walk, both $r^S_{x,t}$ (black dotted line in Fig. 4.5(a)) and $r^A_{x,t} = -r^S_{x,t}$ (black dotted line in Fig. 4.5(b)) undergo damped oscillations with a period of four steps as the steady-state is reached. Since the oscillations are out of phase for these orthogonal initial states, the trace distance between such states also oscillates in time with decreasing amplitude (black dotted line in Fig. 4.5(c)). Therefore, even though there is a back-flow of information from the environment to the open system in the standard walk, the damping in oscillations shows that information flow between the two subsystems reduces and eventually vanishes in time [136]. For non-zero values of ϕ, oscillations in the initial state component $r^{A(S)}_{x,t}$ arise depending on the overlap with the bound states. When $\phi = \pi/4$, the oscillations in $r^A_{x,t}$ die out very quickly, whereas oscillations with period two between sublattice symmetric pair of localized states survive for $r^S_{x,t}$ as shown by the blue dot-dashed line in Fig. 4.5(a)-(b). For $\phi = \pi/2$, similar oscillations exist, except they die out more slowly for $r^A_{x,t}$ which has a finite overlap with the emerging reflection anti-symmetric bound state whereas oscillations continue with higher amplitudes for $r^S_{x,t}$ since the reflection symmetric bound-state becomes more localized for this value of ϕ. At $\phi = \pi$ where bound states of both parities exist, oscillations in $r_{x,t}$ occur with higher amplitudes for both of the initial states in comparison with the other shown phase values.

Having obtained the time dependence of $\rho^{\text{coin}}_{S,A}$, we calculate the trace distance $D(\rho_S, \rho_A) = |r_{S,x} - r_{A,x}|$, and display our findings in Fig. 4.5(c), as a function of ϕ. In contrast to the standard quantum walk where the trace distance oscillations die out in time, we find that they survive for non-zero ϕ, as at least one of $r^{S,A}_{x,t}$ keeps oscillating in time. However, we should keep in mind that the value of the trace distance also depends on the mean values $\overline{r^{S,A}_{x,t}}$ about which oscillations take place. For example, when $\phi = \pi/2$ we get oscillations in $D(\rho_1, \rho_2)$ with smaller amplitudes than in $r^S_{x,t}$, which will be of importance in our later discussions.

As the persistent oscillations in trace distance play a crucial role for the evaluation of the BLP measure in our model, the oscillation means $\overline{r^{S,A}_{x,t}}$ and the oscillation amplitudes are plotted in Fig. 4.6(a). Comparison with Fig. 4.2(c) reveals that, as the overlap between one of the the initial states and the bound states increases, $\overline{r^{S,A}_{x,t}}$ converges to the r_x of the corresponding bound state and oscillations appear. For

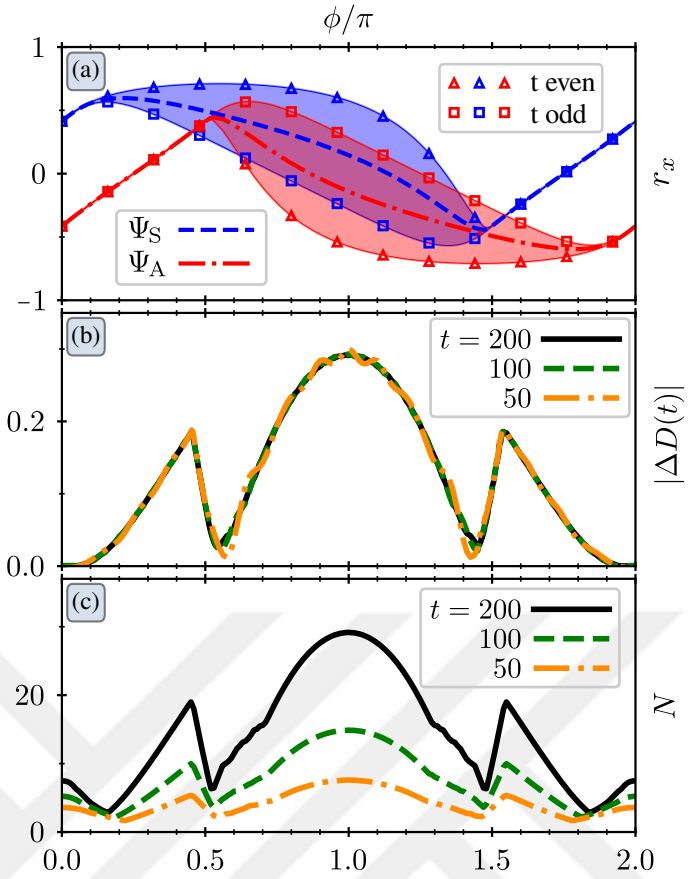

Figure 4.6 : (a) Long-time limit time average of the reduced coin density matrix parameter r_x for reflection symmetric ($|\Psi_S\rangle$) and anti-symmetric ($|\Psi_A\rangle$) initial states as a function of ϕ. (Time average is taken over 100 steps between $t = 400$ and $t = 500$.) Instantaneous values at even and odd time steps are shown by square and triangle markers, respectively. (b) Trace distance oscillation amplitudes between initial states $|\Psi_S\rangle$ and $|\Psi_A\rangle$ at different times show that they quickly converge to their long-time limit values for all ϕ. (c) BLP measure $\mathcal{N}$ (4.25) at three different times. The maximization is performed over all the initial coin states for quantum walks starting at the impurity site. The linear increase in time reflects trace distance oscillations with constant amplitude. (See (b).)

the interval $\phi \in (\pi/2, 3\pi/2)$, $\overline{r_{x,t}^{S,A}}$ becomes the same as r_x in the long time limit. The difference in $\overline{r_{x,t}^{S,A}}$ approaches to zero at $\phi \sim 0.6\pi$ and $\phi \sim 1.4\pi$, yielding very small values for the trace distance together with the fact that essentially one of $r_{x,t}^{S,A}$ oscillates about their common mean. For other values of ϕ, the trace distance is mainly determined by the oscillations in $r_{x,t}^{S,A}$. Since the period of the oscillations is two time steps due to the sublattice symmetry, the changes in trace distance can be obtained by subtracting the value at even time step from the neighbouring odd time step which is plotted in Fig. 4.6 (b) at three different times. These plots clearly demonstrate that the trace distance oscillations quickly converge to their long time limit. As the bound

states get more localized for certain ϕ values and also the overlap of the initial states with them increases, so do the amplitude of the oscillations in the trace distance.

To evaluate the BLP measure, we maximize the sum of the positive increases in trace distance over all possible orthogonal pairs of initial states starting at the impurity site which is shown in Fig. 4.6(c) as a function of ϕ for three increasing values of time. The result reveals that the pair $\left|\psi_{S,A}\right\rangle$ that we used for the preceeding analysis actually maximizes the sum in the BLP measure in the long-time limit. In contrast to the standard walk, the initial states maximizing BLP measure are equal superposition of symmetric and anti-symmetric states and these states do not change under other decoherence mechanisms [136]. Near $\phi = 0, \pi/2, 3\pi/2, 2\pi$, where bound states are weakly localized, we find that other orthogonal pairs actually maximize the BLP measure. However these regions get smaller as we consider longer time evolutions. The sudden drop in BLP at $\phi = \pi/2, 3\pi/2$ is related to the fact that oscillations take place about similar mean values. More importantly, we establish that the BLP measure of non-Markovianity increases with the emergence of bound states and reaches its maximum value at $\phi = \pi$ when the number and localization of bound states assumes their maximum, as demonstrated by the effective localization length in Fig. 4.2(b). The relation of non-Markovianity and localization is also apparent comparing the BLP curve with the average PR shown in Fig. 4.4, which is maximum at $\phi = \pi$.

4.5.2 Rivas-Huelga-Plenio (RHP) measure

Next, we consider Rivas-Huelga-Plenio (RHP) [131] measure of non-Markovianity, which is based on the dynamics of entanglement between the system of interest and an ancillary system. The ancillary system A is assumed to have no dynamics of its own and is completely isolated so that any initial entanglement between the system and the ancilla can be affected by the open system dynamics only. In fact, similar to the BLP measure, this measure is also a witness for the violation of the divisibility. Considering the fact that no entanglement measure E can increase under local CPTP maps, it is rather straightforward to observe that

$$E[(\Lambda(t,0)\otimes I)\rho_{\text{coin},A}] \leq E[(\Lambda(s,0)\otimes I)\rho_{\text{coin},A}] \tag{4.27}$$

for all times $0 \leq s \leq t$. Hence, any increase in the entanglement between the open system and its ancillary can be understood as a signature of non-Markovian memory

effects in the time evolution. In other words, while the entanglement contained in $\rho_{\text{coin},A}$ decreases monotonically for all Markovian processes, non-Markovian behaviour in the dynamics can be captured through the temporary increase of entanglement. In the same spirit of the BLP measure, one can then measure the degree of non-Markovianity using the following quantity:

$$\mathcal{I}^{(E)} = \max_{\rho_{CA}} \sum_{t,\Delta E_{\text{CA}}>0} \Delta E_{\text{CA},t} \tag{4.28}$$

where E_{CA} denotes the entanglement between the coin and a two level ancillary system. For any entanglement measure E_{CA}, the RHP measure is found by maximizing $\mathcal{I}^{(E)}$ over all initial reduced density matrices ρ_{CA} of the composite coin-ancilla system. In order to calculate this measure, we start the evolution from composite initial state $|\Phi^+\rangle|0\rangle = \frac{1}{\sqrt{2}}(|\leftarrow\rangle_C|\downarrow\rangle_A + |\rightarrow\rangle_C|\uparrow\rangle_A)|0\rangle$ and use concurrence [162] as the entanglement measure. It has been shown that when concurrence is used as entanglement measure, the optimum initial state maximizing the RHP measure is a Bell state, for a single qubit interacting with an environment [163].

Fig. 4.7(a) shows the variation of the concurrence in time which is calculated from the reduced coin-ancilla state after tracing out the spatial degrees of the walker during the evolution. For the standard quantum walk, the entanglement oscillations with period of four steps are damped and slowly die out with time. Therefore, the RHP measure accumulates a finite amount of non-Markovianity in the long time limit which is similar to the behaviour of the BLP measure for the standard walk. On the other hand, in contrast to the BLP measure, the nature of bound states emerging with non-zero phase ϕ plays a key role for the coin-ancilla entanglement. In the presence of reflection symmetric or anti-symmetric bound states only, the concurrence dies out very quickly. This is due to the fact that the symmetric and anti-symmetric states couple to different environmental degrees of freedom. For example, with only symmetric bound states present, the symmetric part of the coin-position state remains mostly localized in the vicinity of the impurity site whereas the anti-symmetric part moves away from the origin. Hence, the coin-ancilla entanglement is quickly destroyed upon tracing out the environmental degrees of position, as the coin-ancilla state becomes an incoherent mixture. An example of this situation is displayed in Fig. 4.7(a) for $\phi = \pi/3$. It is only when both reflection symmetric and anti-symmetric stationary states exist that some entanglement can survive which shows non-decaying oscillations. These oscillations

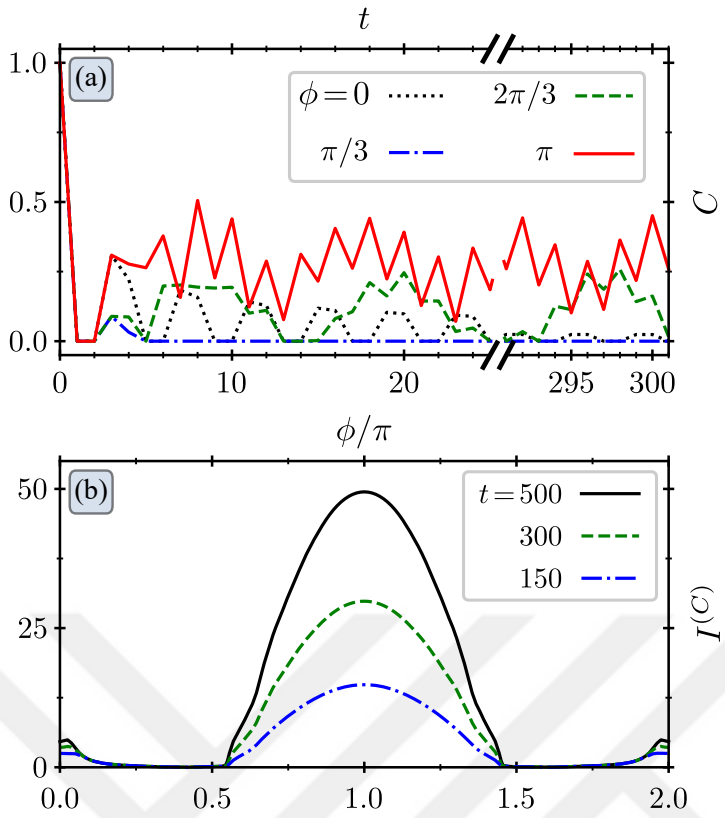

Figure 4.7 : (a) Concurrence between the coin and the ancilla qubit as a function of time for representative values of the phase parameter ϕ. When bound states with both positive and negative reflection parity exist, the concurrence shows oscillations. (See text for the involved frequencies.) (b) Concurrence based RHP measure as a function of ϕ at three different time steps showing linear increase with time for $\phi \in (\pi/2, 3\pi/2)$. RHP has a vanishing value when well-formed bound states of only positive or negative reflection parity exist.

are due to the finite dimension of the bound state subspace and the frequencies of concurrence oscillations can easily be obtained from the quasi-energy differences. Such a case is displayed in Fig. 4.7(a) for $\phi = \pi$ with two dominant periods. One period is of two steps due to the sublattice symmetric bound states with quasi-energy difference π and another one is approximately ten steps due to the quasi-energy difference of $\Delta E \approx 0.205\pi$ between reflection symmetric and anti-symmetric states. The latter dependence again shows the importance of bound states of both parities for the RHP measure. The energy difference ΔE does not change much as ϕ changes in the domain of four bound states unless one group of bound states is very weakly bound. (See Fig. 4.2)

Using the time evolution of the coin-ancilla entanglement as shown in Fig. 4.7(a), we evaluate the RHP measure for all values of the impurity phase ϕ. The results are

plotted in Fig. 4.7(b) for three increasing values of the final time. The amount of non-Markovianity measured by the RHP measure drastically depends on whether the reflection symmetric and anti-symmetric bound states are both supported for a given ϕ or not. In the interval $\phi \in (0, \pi/2)$ where only the symmetric bound states exist, the concurrence vanishes quickly in time since the coin-ancilla Bell state can only be supported if both symmetric and anti-symmetric bound states exist. Therefore, the coupling of the symmetric and anti-symmetric coin states to different environmental degrees of freedom completely destroys the Bell state of the coin-ancilla system and results in a vanishing value for the RHP measure. A similar situation occurs in the interval $\phi \in (3\pi/2, 2\pi)$ where only reflection anti-symmetric bound states exist and coin-ancilla entanglement is destroyed. In the interval $\phi \in (\pi/2, 3\pi/2)$ where bound states of both symmetries exist, the coin-ancilla entanglement is more robust and the RHP measure captures the non-Markovianity increasing linearly with t in the long time limit due to non-decaying oscillations in the coin-ancilla entanglement. In this ϕ interval, the RHP displays the same behaviour as seen for the BLP measure in Fig. 4.6(c).

4.6 Conclusion

We have provided a comprehensive and systematic analysis of non-Markovianity in a quantum walk model with a phase impurity in relation with the phenomenon of localization. At the heart of analysis lies the manifestation of bound states emerging due to the existence of the phase impurity at the starting site of the walker. We have first presented a technique to analytically obtain the bound states of the model making use of the transfer matrix method. These bound states emerge in one or two sublattice symmetric pairs possessing definite reflection symmetry. With this knowledge at hand, we have explored the localization properties of the walker in the position space. To this end, we have adopted two initial state independent quantities to measure the degree of localization, namely, the effective localization length for all eigenstates and an average participation ratio after time evolution over all initial states starting at the impurity site. Our analysis clearly demonstrates that the degree of localization of the walker is directly determined by the properties of the bound states.

More importantly, our main contribution in this work is the unveiling of an intrinsic relation between the emergence of bound states and the degree of non-Markovianity of the dynamics of the walker. In order to study non-Markovian behaviour in the time evolution of the walker, after tracing out the spatial degrees of freedom, we have utilized two distinct measures of quantum non-Markovianity, i.e., the BLP and the RHP measures based on the dynamics of trace distance and entanglement, respectively. These measures help us to understand the information flow between the principal coin system and the position system forming the environment from different perspectives. We show that, in the case of the existence of spatial decoherence in the form of a phase impurity, the BLP measure is optimized by the eigenstates of the coin operator for almost all values of the phase ϕ. Note that when one has decoherence in terms of broken links instead, the degree of decoherence does not change the optimal state maximizing the BLP measure [136]. Our investigation also proves that phase impurity amplifies the degree of non-Markovianity quantified by the BLP measure. The underlying reason behind this behaviour is the oscillations in the state of the coin which essentially takes place between the sublattice symmetric bound state components with a period of two steps. Then, in general, increasing overlap between the initial and the bound states implies a greater degree of non-Markovianity. However, also note that when the time average of the reduced coin states corresponding to two orthogonal initial states are close to each other, the BLP measure drops abruptly.

Next, we employed the RHP measure to analyze the degree of non-Markovianity in the dynamics of the walker. When the coin state is maximally entangled with an ancillary system initially, the amount of entanglement is known to oscillate in time for the standard walk. However, our examination demonstrates that, in case of the existence of a phase impurity, if the bound subspace supports only one type of reflection symmetric state, the coin-ancilla entanglement vanishes after a few time steps and the RHP measure becomes very small compared to the standard walk case. On the other hand, when both reflection symmetric and anti-symmetric bound states are present, the entanglement oscillations are persistent in time, leading to high values of RHP measure. Thus, while the RHP measure is generally in good agreement with the BLP measure when both even and odd parity bound states exist, the RHP measure fails to reliably detect the non-Markovian behaviour when only symmetric or anti-symmetric

bound states are present. Most importantly, as can be clearly seen from both measures, maximum non-Markovianity is reached where our localization measures determined by the bound states become also maximum. Relationship between non-Markovianity and localization have been discussed in random static disorder models [133, 137] where non-Markovianity increases with disorder. We observe more nuanced behaviour between bound states and non-Markovianity as discussed above.

We would like to indicate that the experimental realization of the model we presented here is quite feasible with today's technology. The time-multiplexing quantum walk employs laser light pulses going successively around a fiber loop where the position space is effectively encoded in the time domain from the point of view of the detectors [70]. The main advantage of this setup is it's scalability and it's long coherence times, i.e., it only requires a fixed number of optical elements to realize the quantum walk for relatively large number of steps. The recent developments in the setup allow deterministic out-coupling of the light pulses from any site by utilizing electro-optic modulators [164]. It is also possible to introduce arbitrary phases specific to any site by programming of the electro-optic modulators accordingly, which actually would allow the realization of the model we provided here [154, 165].

In the next chapter, we extend this quantum walk model to incorporate dynamical spin impurities coupled to the walker at each site. We analyze effects of these impurities on the localization and entanglement properties, as well as the effects of the walker on the spin dynamics.

5. QUANTUM WALK COUPLED TO A SPIN CHAIN[1]

In this chapter, we consider localization properties of a quantum walk coupled to a spin chain. In Sec. 5.1, we discuss different types of localization encountered in quantum systems and introduce a disorder-free quantum walk model. Sec. 5.2 and Sec. 5.3 are devoted to the exploration of our model in the context of disorder-free localization. We discuss the implications of the extensive number of local symmetries. We introduce the quantities we use to measure localization and entanglement in Sec. 5.4. In Sec. 5.5, we provide the quasi-energy spectrum as a function of the interaction parameter. We study the localization properties of the walker and related dynamics of the local spins in Sec. 5.6. We demonstrate the logarithmic growth of entanglement in time that arises due to an effective interaction between the spins induced by the walker. The equilibration of entanglement entropy for small system sizes and details of the matrix-product-state (MPS) calculations are also discussed in Sec. 5.7. We show the effects of a symmetry-breaking field in Sec. 5.8. In Sec. 5.9, we conclude by making connections to similarly behaving systems and possible extensions.

5.1 Introduction

By yielding insights into fundamental questions on thermalization of closed quantum systems, disorder and localization have earned themselves a central place in quantum physics. The corner stone of these topics is the phenomenon of Anderson localization [166], which in one-dimension produces localization of all single particle eigenstates for arbitrarily weak disorder. Due to these localized eigenstates, particles can not move through the system and thermalization is prevented. The absence of transport and thermalization has been found to be robust to interactions [167–171]. This many-body localization (MBL), which occurs at finite temperature in the presence of sufficiently strong disorder and interactions, is closely related to the subject of

[1]This chapter is based on the paper Danacı, B., Yalçınkaya, I., Çakmak, B., Karpat, G., Kelly, S. P., and Subaşı, A. L. (2021). Disorder-free localization in quantum walks. *Physical Review A*, *103*(2), 022416.

ergodicity-breaking due to the impossibility of thermalization for MBL systems. In fact, the presence of a MBL phase serves as an example of the violation of the eigenstate thermalization hypothesis [172]. Disentangled quantum liquids provide another example of non-thermalizing localization where a light species can localize with low entropy due to the coupling to a system of heavy particles [173, 174]. On the other hand, the manifestation of disorder-free localization (DFL) in quantum systems has been demonstrated more recently, where the system generates its own effective disorder dynamically in the absence of any external randomness [175]. Another example of DFL has been observed in a translationally invariant Ising-Kondo Lattice model, where Anderson localization occurs due to the conserved moments [176].

In this chapter we study DFL in a quantum walk model. For the particular quantum walk we consider a discrete-time walker coupled to on-site spin-half systems on a one-dimensional lattice such that the presence of the walker on a specific site coherently rotates the corresponding spin. Our examination of the considered system involves two parts. First, we consider the walker and investigate its spreading dynamics as it interacts with the spins. For weak coupling the probability distribution is only partially localized around the origin and still has ballistic tails spreading out linearly in time. As the coupling gets stronger, the walker becomes completely localized with no ballistic tails in the time evolution. This dynamical localization appears without breaking any translational or temporal symmetries.

In this sense, our model provides a simple manifestation of interaction-induced (disorder-free) localization [175]. We then turn our attention to the spin system and study its relaxation and entanglement dynamics. Similar to MBL, the local integrals of motion on the spin chain decohere and entangle due to emergent interactions between them. When the walker is localized, the emergent interaction decays exponentially and leads to sublinear growth in entanglement mimicking the effect in MBL systems. Interestingly, for our simulations at intermediate time scales, entanglement growth remains slow also in the seemingly delocalized regime due to the suppression of the ballistic tails and the low coupling.

5.2 Quantum Walk Interacting with On-site Local Spins

The discrete-time quantum walk was discussed in Sec. 4.2. In this chapter, we turn our attention to a quantum walker interacting with a chain of N spins which are permanently localized at the lattice sites and not directly coupled with each other. We denote the state of a single spin at site n by $|s_n\rangle$ where s_n will be either $\{0,1\}$ or $\{+,-\}$ referring to the eigenstates of $\hat{Z}$ or $\hat{X}$, respectively. The total Hilbert space is $\mathcal{H}_c \otimes \mathcal{H}_p \otimes \mathcal{H}_s$, and has size $2 \times N \times 2^N$ which scales exponentially in N. The spins' subspace $\mathcal{H}_s$ is spanned by $\{|\mathbf{s}\rangle\} \equiv \{|s_1 s_2 \dots s_N\rangle\}$ where $\mathbf{s}$ can have 2^N possible values corresponding to different spin configurations. We will employ the notation $\mathbf{s}_\mathrm{Z}$ and $\mathbf{s}_\mathrm{X}$ to refer to eigenbasis of $\hat{Z}$ and $\hat{X}$, respectively. The walker interacts with the spins such that its presence on any site n induces a rotation on the corresponding spin state $|s_n\rangle$ by an angle ϕ at each step, as shown in Fig. 5.1. Without loss of generality, we will consider rotations around the x-axis throughout the paper. The site dependent interaction operator in the whole Hilbert space of the system can accordingly be written as

$$\hat{M} = \sum_n \hat{I}_2 \otimes |n\rangle\langle n| \otimes \exp\left(-i\phi \hat{X}_n\right). \tag{5.1}$$

where ϕ is the rotation angle and the operator

$$\hat{X}_n = \hat{I}_2^{\otimes(n-1)} \otimes \hat{X} \otimes \hat{I}_2^{\otimes(N-n)} \tag{5.2}$$

acts on the spin at the n^{th} site. Thus, we introduce the single step operator to involve walker-spin interaction as $\hat{W}_M = \hat{T}\hat{C}\hat{M}$ where both $\hat{T}$ and $\hat{C}$ are now naturally extended with $\hat{I}_{2^N}$ for consistency. Like the coin-state dependent translation operator entangling the coin and position degrees of freedom [177, 178], the position-state dependent spin interaction operator entangles the walker and spins as well. Therefore, the total state of the system at time t,

$$|\Psi_t\rangle = \sum_{c,n,\mathbf{s}} a_{c,n,\mathbf{s}}(t)|c,n,\mathbf{s}\rangle, \tag{5.3}$$

is a superposition of both coin, position and spin state degrees of freedom.

In general, even after starting with a product state at $t = 0$, it is impossible to factorize any degree of freedom completely at later times. It is worthy to note that the model we consider here is simpler in terms of its construction compared to the other similar

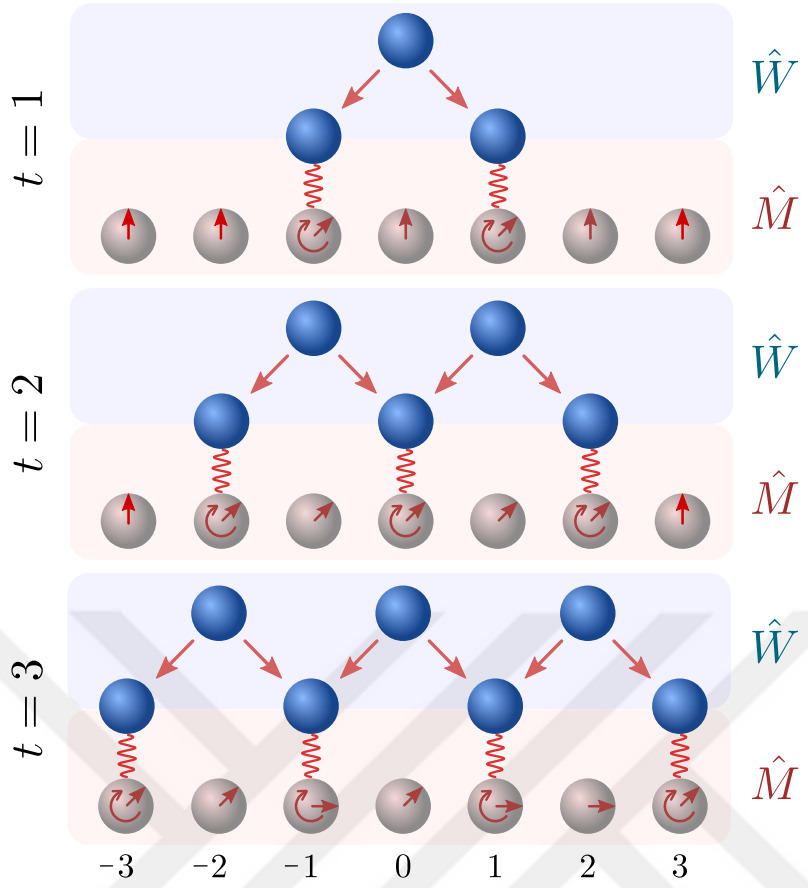

Figure 5.1 : Schematic representation of the first 3 steps of the quantum walk model employed in this chapter. The quantum walker (blue-dark balls) interacts with the spin chain (gray-light balls) in each step such that the spin rotates by an angle ϕ when the walker is on that site and has no dynamics otherwise. The starting point of the walk is indicated by 0 and a balanced walk is depicted.

models since we consider a one-dimensional position space and the spins have no direct action on the walker [179–181]. The relationship we introduce with Eq. (5.1) is analogous to that of the coin and position degrees of freedom in the conventional quantum walk. Here, we apply a rotation to the local spins depending on the walker's position. Unlike spin-spin interactions such as spin exchange, this interaction does not depend on the coin degree of freedom.

5.3 Disorder Free Localization

In the quantum walk $\hat{W}_M$, the local spins have N conserved quantities as can be seen by noting that the step operator

$$\hat{W}_M = \sum_{c,n} |c\rangle\langle c| e^{-i\theta\hat{X}} \otimes |n+(-1)^c\rangle\langle n| \otimes e^{-i\phi\hat{X}_n} \tag{5.4}$$

is invariant under spin flips, i.e., $[\hat{X}_n, \hat{W}_M] = 0$ for all n, where we extend $\hat{X}_n \to \hat{I}_{2N} \otimes \hat{X}_n$, yielding N conserved quantities in total. These extensive number of conserved local quantities in the model act as hidden disorder and the quantum walker evolving with $\hat{W}_M$ localizes dynamically similar to other DFL mechanisms [175]. This is clearly seen when looking at the simultaneous eigenstates of both $\hat{X}_n$ and $\hat{W}_M$ which are formed within the subspace spanned by $\{|c, n, \mathbf{s}_\mathrm{X}\rangle\}$ with $\mathbf{s}_\mathrm{X}$ fixed. This basis block diagonalizes $\hat{W}_M$ such that each $2N \times 2N$ block is labeled by one of 2^N possible spin configurations $\mathbf{s}_\mathrm{X}$, which can be written as

$$\langle \mathbf{s}'_\mathrm{X} | \hat{W}_M | \mathbf{s}_\mathrm{X} \rangle = \begin{cases} \hat{W}_{\mathbf{s}_\mathrm{X}}, & \text{if } \mathbf{s}_\mathrm{X} = \mathbf{s}'_\mathrm{X} \\ 0, & \text{otherwise} \end{cases}. \tag{5.5}$$

The quantum walk $\hat{W}_M$ can therefore be viewed as a superposition of walkers evolving in a set of disordered landscapes under $\hat{W}_{\mathbf{s}_\mathrm{X}} = \hat{T}\hat{C}\hat{D}_{\mathbf{s}_\mathrm{X}}$ with the disorder operator $\hat{D}_{\mathbf{s}_\mathrm{X}} \equiv \sum_n \hat{I}_2 \otimes |n\rangle \langle n| e^{i\phi s_n}$ and s_n are the elements of the set $\mathbf{s}_\mathrm{X}$ [2]. Therefore, for a single spin configuration $\mathbf{s}_\mathrm{X}$, the state of the quantum walk at time t can be written in terms of the eigenstates of $\hat{W}_{\mathbf{s}_\mathrm{X}}$ such as

$$|\Psi_t\rangle = \sum_m^{2N} a_{m,\mathbf{s}_\mathrm{X}}(t) |\psi_{m,\mathbf{s}_\mathrm{X}}\rangle \otimes |\mathbf{s}_\mathrm{X}\rangle, \tag{5.6}$$

where $|\psi_{m,\mathbf{s}_\mathrm{X}}\rangle$ is the m^{th} eigenstate with amplitude $a_{m,\mathbf{s}_\mathrm{X}}(t)$. For example, the two completely $\hat{X}$-polarized spin configurations, where all s_n are either $+$ or $-$, yield the standard quantum walk with all of its eigenstates $|\psi_{m,\mathbf{s}_\mathrm{X}}\rangle$ extended [44]. On the other hand, the existence of a single spin-flip disorder leads some localized eigenstates $|\psi_{m,\mathbf{s}_\mathrm{X}}\rangle$ around this impurity [141, 142]. In general, when the distribution of s_n are disordered, the eigenstates can become localized [166]. For the dynamics to be localized, the delocalized eigenstates should not effectively contribute to the dynamics, which depends on the choice of the initial state.

We now elaborate on the calculation of the localization dynamics and its connection with the initial state. We consider local spin initial states that are polarized in $\hat{Z}$, e.g. $\mathbf{s}_\mathrm{Z} = (00\ldots0)$, which is an equal weight superposition of all $|\mathbf{s}_\mathrm{X}\rangle$ eigenstates. Thus, the

[2] Even though the diagonalization problem of $\hat{W}_M$ can be broken down to those of $\hat{W}_{\mathbf{s}_\mathrm{X}}$, the number of the small size problems grows exponentially with the system size ($\sim 2^N$) in general. We note that the one-dimensional geometry together with local couplings allows simulations of large system sizes by employing an MPS ansatz where we represent the Hilbert space with a six dimensional local basis. (See Sec. 5.7 for details.)

evolution occurs independently in all spin sectors $\{\mathbf{s}_\mathrm{X}\}$ so that

$$|\Psi_t\rangle = \hat{W}_M^t|\Psi_0\rangle = \frac{1}{2^{N/2}}\sum_{\mathbf{s}_\mathrm{X}}\left\{\hat{W}_{\mathbf{s}_\mathrm{X}}^t|\psi_0\rangle\otimes|\mathbf{s}_\mathrm{X}\rangle\right\}. \tag{5.7}$$

Noting that the projection operator $\hat{P}_n = I_2\otimes|n\rangle\langle n|\otimes I_{2^N}$ does not mix the different spin states, the probability distribution is equivalently given by a disorder average of the disordered walker $\hat{W}_{\mathbf{s}_\mathrm{X}}$ as

$$P_n(t) = \frac{1}{2^N}\sum_{c,\mathbf{s}_\mathrm{X}}\left|\langle c,n|W_{\mathbf{s}_\mathrm{X}}^t|\psi_0\rangle\right|^2. \tag{5.8}$$

The probability $P_n(t)$ becomes an average over the binary distribution of local phases $e^{\pm i\phi}$. Hence, if walks under $\hat{W}_{\mathbf{s}_\mathrm{X}}$ are localized on average, the dynamics will be too. We obtain the probability distribution of the quantum walker by employing a numerically exact MPS ansatz which evaluates Eq. (5.6) by truncating the state for a given precision in all spin configurations (see Sec. 5.7 for details). Performing the averaging in Eq.(5.8) for the walker through the total quantum evolution is technically equivalent to the proposition by Paredes et al. [182]. In that context simulating a quantum system with classical random variables is accomplished by exploiting quantum parallelism using an auxiliary quantum system. The auxiliary system which corresponds to the local spins in our model does not have self-dynamics.

Having shown that the computational complexity of numerically calculating $P_n(t)$ for the unitary $\hat{W}_M$ can be reduced to that of $\hat{W}_{\mathbf{s}_\mathrm{X}}$, we also obtain the walker's probability distribution by random sampling via Eq. (5.8). Statistically, the finite number of random spin configuration samples are most likely to be chosen among the vicinity of zero total X-polarization. The agreement between our sampling and MPS results confirms that those configurations are the ones that contribute to the dynamics significantly as we present in Sec. 5.6.

Having reduced the problem to that of a disordered walker, we emphasize that quantum walks are known to exhibit Anderson localization in the presence of position-dependent static disorder (time-independent), which has been demonstrated analytically [139, 140, 183], numerically [184, 185], and experimentally [154, 186]. We show that when ϕ is sufficiently large, similar to one-dimensional Hamiltonian models with disorder the probability distribution around the origin stays exponentially localized showing the striking signature of Anderson localization [166]. For finite

system sizes, the transition between spreading and localized regimes has also been shown [154]. Finally, we note that the parameter ϕ in the unitary evolution related to disorder in our model yields dynamical localization, but should not be directly associated with the random potential of Hamiltonian models.

5.4 Figures of Merit

To quantify the localization of the quantum walker, we will employ two measures derived from the probability distribution of the quantum walker, namely, the variance

$$\sigma_t^2 = \sum_n n^2 P_n(t) \tag{5.9}$$

and the normalized Inverse Participation Ratio

$$\widehat{\mathrm{IPR}} = \left(N \sum_{n=1}^{N} P_n^2 \right)^{-1} . \tag{5.10}$$

The variance of the probability distribution is a well-known measure for classifying the spreading rate of the quantum walker. While a ballistic spread as in the standard quantum walk case gives a quadratic growth in the variance $\left(\sigma_t^2 \sim t^2\right)$, a classical random walk is diffusive with a variance that increases linearly $\left(\sigma_t^2 \sim t\right)$ with respect to the step number. Apart from these, a localized probability distribution yields either a constant or a fluctuating variance which has no overall increase in time.

Similar to the participation ratio described in Sec. 4.4 (see Eq. (4.23)), the inverse participation ratio, estimates the average number of sites where the quantum walker is spread over uniformly. We employ the inverse participation ratio which is normalized over the size of the lattice N as given in Eq. 5.10. Therefore, $\widehat{\mathrm{IPR}} \to 1$ if the walker is spread over the position space uniformly and $\widehat{\mathrm{IPR}} \to 0$ if the walker is localized over a single site, as $N \to \infty$.

After we discuss the localization properties of the quantum walker, we will turn our attention to the spin chain itself and examine the entanglement entropy between its bipartite subdivisions for investigating further properties of DFL. Let A and B represent subsystems forming the two halves of the total system. [3] The reduced density matrix of

[3] In addition to the local spins found in each partition, we split the position and coin degrees of freedom of the walker to encompass the sites corresponding to partitions A and B, separately. Therefore, we also consider a vacuum state representing the absence of the walker at the given partition (please also

system A is obtained by tracing over system B as $\rho_A(t) = \mathrm{tr}_B |\Psi_t\rangle\langle\Psi_t|$ where $|\Psi_t\rangle$ is the total state of $(A+B)$ given in Eq. (5.6). Since $|\Psi_t\rangle$ is a pure state by assumption, we can employ the von Neumann entropy $S(\rho_A) = -\mathrm{tr}\,[\rho_A \log \rho_A]$ to measure the entanglement between system A and B. Calculation of the von Neumann entropy as a function of t and walker-spin interaction parameter ϕ is a difficult problem to handle due to large Hilbert space in question. Nevertheless, MPS ansatz provides an easier way of calculation as we discuss in Sec. 5.7.

5.5 Energy Spectrum

We start by discussing the quasi-energy spectrum of the step operator $\hat{W}_M$ (the eigenvalues of $\hat{H}_{\text{eff}}$) as a function of ϕ as shown in Fig. 5.2 for a system size of $N = 18$. The surface plot has quasi-energy E on the vertical axis and each eigenstate is colored with its IPR value. At $\phi = 0$ the system has a 2^{18}-fold degenerate disorder free quantum walk spectrum consisting of two bands. The bands are separated by two band gaps with width $2\theta = \pi/2$ and all states are delocalized for the quantum walker indicated by the light color map. As the coupling is turned on, localized states indicated by darker colors appear first at the edges of the two bands whereas delocalized states are mostly in the middle of the bands. At $\phi = \pi/4$ band gaps are closed and almost all eigenstates are localized for $\phi > \pi/4$. One cannot directly identify a mobility edge due to the fact that quasi-energies from different spin sectors get also shifted depending on the ϕ value. For example, the $s_n = -$ and $+$ (for all n) spin sectors always have delocalized states, however their quasi-energies are shifted by $\pm\phi$ with respect to the standard walk spectrum causing the band gap to close at $\phi = \theta = \pi/4$. These shifts explain delocalized states (indicated by light colors) in the spectrum seen for $\phi > \pi/4$ and are also the cause of the upward and downward moving branches for localized states. Fig. 5.2 therefore visualizes the single-particle localization as it appears in combination from the different spin sectors $\mathbf{s}_X$. As discussed in Sec. 5.3, the localized eigenstates are responsible for the emergent localization which is presented in the following section.

---

see the local bases for the MPS representation in the Sec. 5.7). The Hilbert space of a partition consists of the tensor product of all the spin states in that partition and all the states of the walker in that partition including its vacuum state. For $N = N_A + N_B$, the number of degrees of freedom in partition A is given by $(2N_A+1)2^{N_A}$. If the walker state is also traced out, then the spin partition has 2^{N_A} states.

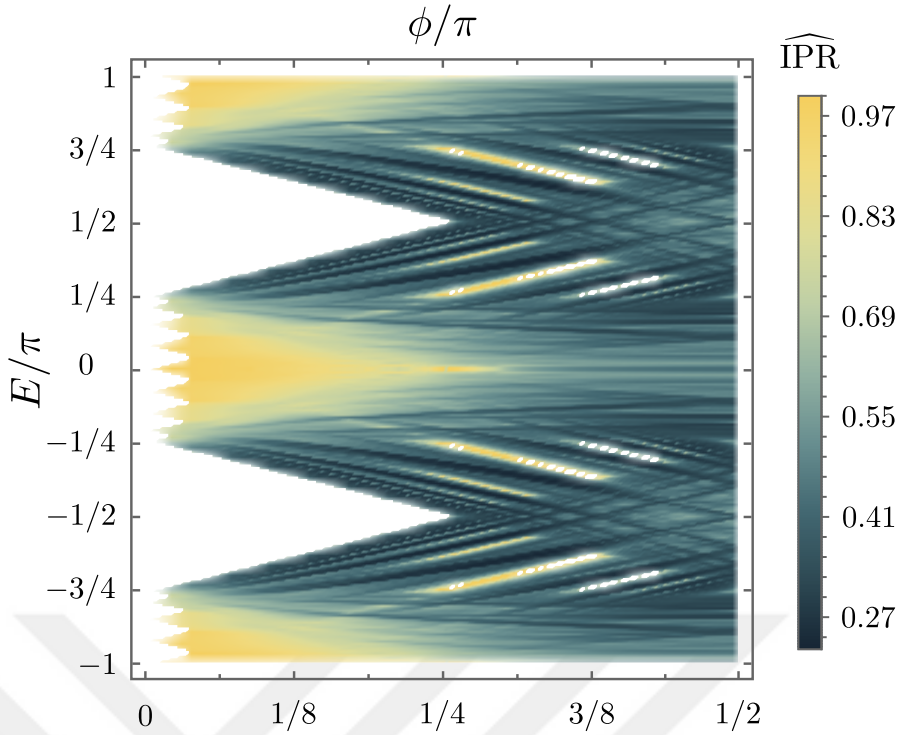

Figure 5.2 : Quasi-energy E spectrum and the inverse participation ratio ($\widehat{\mathrm{IPR}}$) of the corresponding eigenstates with respect to the interaction parameter ϕ for the quantum walker stepping with $\hat{W}_M$. For a given E, the inverse participation values are averaged over degenerate cases and normalized by the number of spins $N = 18$. After the rotation angle $\phi = \pi/4$, the band gaps close and the quasi-energy eigenstates become localized.

5.6 Localization, Entanglement and Decoherence

In this section, we consider the dynamical properties of the quantum walker which is initially localized at $n = 0$. The initial spin state is chosen to be a product of $\hat{Z}$-polarized local spins $|\mathbf{s}_z\rangle$ such that

$$|\Psi_0\rangle = |\chi_0\rangle \otimes |n = 0\rangle \otimes |0\rangle^{\otimes N} \tag{5.11}$$

with the coin state $|\chi_0\rangle = 2^{-1/2}(|0\rangle + |1\rangle)$ yielding a symmetric distribution around the origin as mentioned in Sec. 4.4. The initial spin state $|\mathbf{s}_z\rangle \equiv |0\rangle^{\otimes N}$ is translationally invariant. This choice does not restrict the applicability of our results for any $|\mathbf{s}_z\rangle$ as discussed in Sec. 5.3.

Here we present the results calculated with the random sampling method mentioned in Sec. 5.3. We find that an average over a few thousand samples are in perfect agreement with MPS calculation results, which we performed up to $t = 100$. With 4000 $\mathbf{s}_x$ samples, the quantum walker's probability distribution in position space after $t = 400$ time steps is shown in Fig. 5.3(a) for increasing values of the interaction

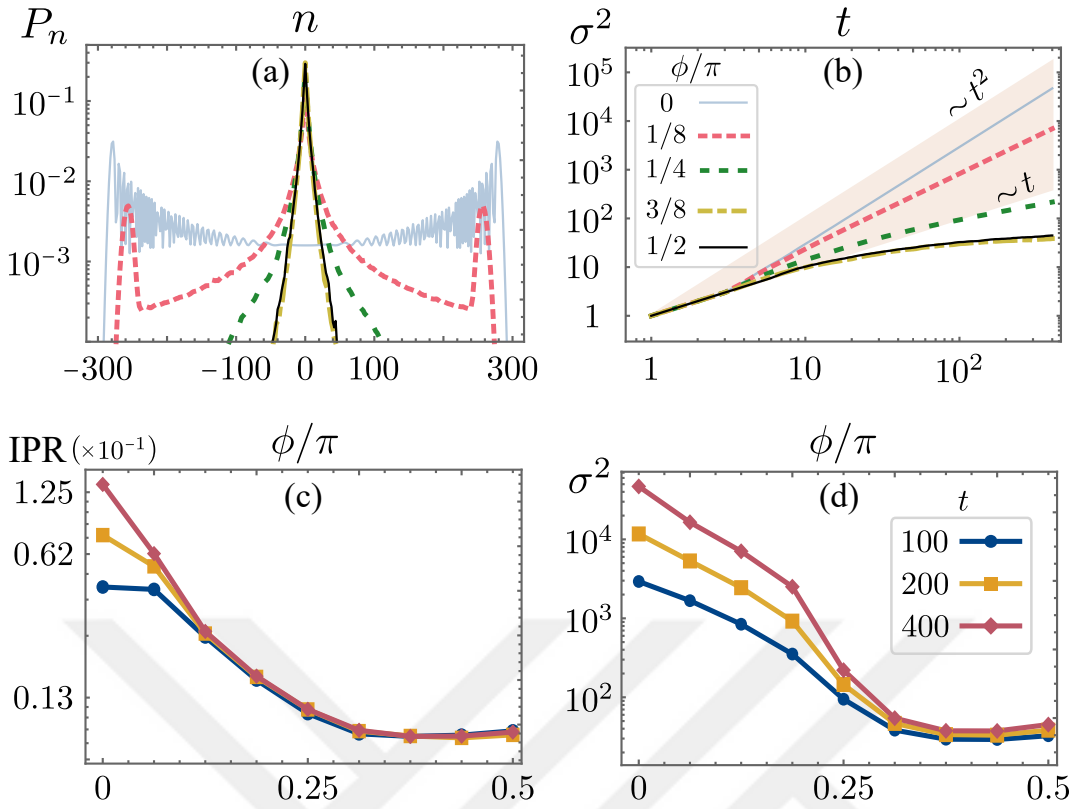

Figure 5.3 : Probability distribution of the walk in the position space after 400 steps (a) and its variance in position space as a function of step number (b), for the initial state $|\Psi_0\rangle$. Inverse participation ratio (IPR) (c) and variance (d) are shown as a function of the spin rotation angle ϕ, at different time steps. IPR is normalized by the lattice size $N = 801$. The walker is exponentially localized for $\phi > \pi/4$.

parameter ϕ. The disorder free standard quantum walk ($\phi = 0$) displays ballistic peaks and the variance of the probability distribution increases as $\sigma^2 \sim t^2$ which gives a slope of two on the log-log plot shown in Fig. 5.3(b). As the coupling to the spins is turned on ($\phi \neq 0$), the quantum walker remains partially localized near the $n = 0$ with less pronounced side peaks. Note that the interference effects leading to oscillations in the probability of the standard walk are wiped out for $\phi > 0$ as seen in Fig. 5.3(a). This is due to decoherence effects induced by the spin environment. For $\phi = \pi/8$, the spread of the ballistic tails decreases as can be seen from the reduced slope of σ^2. Furthermore, at the critical value $\phi = \pi/4$, the tails become completely suppressed and σ^2 displays a near diffusive ($\sigma^2 \sim t$) behavior. The shaded triangle in Fig. 5.3(b) highlights the range between the ballistic spreading and the diffusive limit with its upper and lower edges, respectively. The walker remains exponentially localized for $\phi > \pi/4$ with a localization length of $\lambda \sim 1.6$ which we calculate by fitting $\exp(-2|n|/\lambda)$ to the probability distribution P_n. Note that the localization length

is on the order of the lattice spacing. In this regime, the spread of the quantum walker is sub-diffusive and the variance approaches a constant value as t increases.

The change in the probability distribution as a function of ϕ shows the crossover from ballistic spreading to a complete localization in our disorder free model. Fig. 5.3(c) and Fig. 5.3(d) show the inverse participation ratio and the variance as a function of ϕ for different step numbers, respectively. These plots indicate that regardless of how many steps were taken, spreading of quantum walker is small and it remains constant for $\phi > \pi/4$. The gradual decrease in IPR and σ^2 as ϕ goes from 0 to $\pi/4$ results from the suppression of the side peaks and their decreasing spreading rate, respectively.

The step operator $\hat{W}_M$ creates entanglement between the position, coin, and spin degrees of freedom which can be quantified by the von Neumann entropy of subsystems as we mentioned in Sec. 5.4. We calculate this entanglement entropy S of one parition by spatially dividing the degrees of freedom in half. This can easily be accessed via the singular values in the MPS simulations (see Sec. 5.7) and is plotted as a function of time in Fig. 5.4(a) for different values of the coupling ϕ. Even though the growth is slower for partially localized cases ($\phi < \pi/4$), the entanglement shows sublinear growth starting with the second decade of the time evolution for all non-zero values of ϕ. (For the standard quantum walk at $\phi = 0$ the entanglement saturates at $\log_2 2 = 1$ (horizontal blue line) with the initial state spreading equally into the left and rights half of the system.) The sublinear growth happens faster with increasing ϕ as seen in Fig. 5.4(b) for three different times and S does not change significantly after $\phi \geq \pi/4$ once the system is completely localized. We emphasize that the behavior of S can be observed in other localized systems such as MBL and DFL. Here, the sublinear growth is also related to the walker's Hilbert space being small and the generation of entanglement in the spin chain has to occur via interactions with the small Hilbert space of the walker. The long-time behavior of S is therefore similar for all ϕ even when the walker is partially localized for $\phi < \pi/4$. We present a more detailed analysis of the entanglement spread on the lattice as a function of time in Sec. 5.7.

Finally, we consider the spin sub-system results for which MPS calculations are again required. The $\hat{X}_n$ expectation values of local spins remain zero throughout the evolution as they constitute the conserved quantities in the model. The y-polarization also vanishes for the initial state $|\psi_0\rangle$ since the spins are polarized in z-direction. During

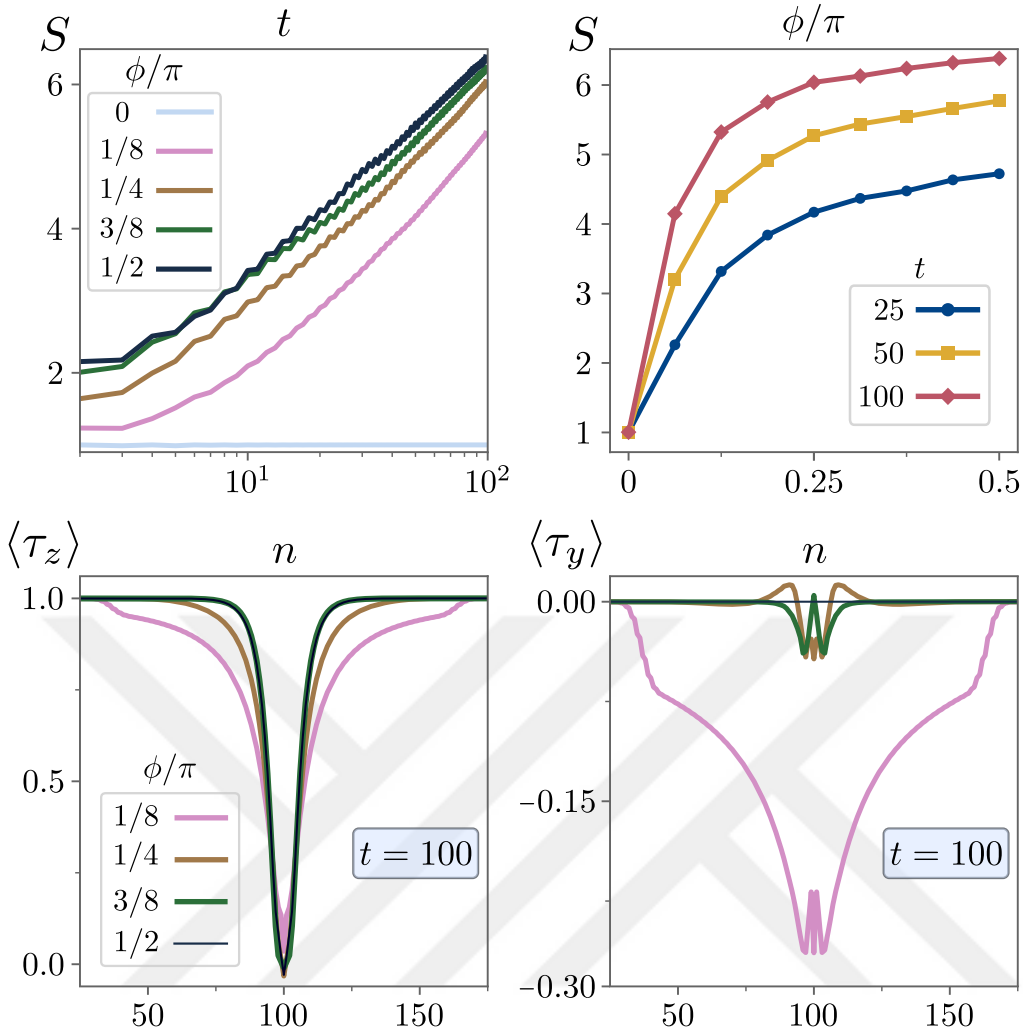

Figure 5.4 : Entanglement entropy between two halves of the chain as a function of time (a) and as a function of the angle ϕ at different time steps (b). Spin expectations along z- (c) and y-axes (d).

the evolution, the spin expectation values decohere because of the interaction with the walker. Therefore, the spatial localization in $\langle\hat{Z}_n\rangle$ appears with a similar structure to that of the walker and is shown in Fig. 5.4(c) at $t = 100$. The expectation values $\langle\hat{Y}_n\rangle$ in Fig. 5.4(d) similarly show the spreading of the side peaks for $\phi = \pi/8$ and the spin textures remain localized for $\phi \geq \pi/4$. We note that differently from the localization of the walker's probability distribution, the spin textures show a dependence on the initial coin state $|\chi_0\rangle$. An imbalance in the weights of $|s_n = \pm\rangle$ states changes the symmetric $\langle\hat{Z}_n\rangle$ distribution and the phase difference effects the $\langle\hat{Y}_n\rangle$ distribution.

5.7 Matrix Product States Representation of Quantum Walk

As explained in chapter 2, the general form of a matrix product state can be written as [10]

$$|\Psi\rangle = \sum_{\mathbf{q}} \mathrm{Tr}\left[A^{q_1} \ldots A^{q_N}\right] |\mathbf{q}\rangle \tag{5.12}$$

where q_n are the local degrees of freedom and $|\mathbf{q}\rangle \equiv |q_1, \ldots, q_N\rangle$ form a basis for the Hilbert space.

In contrast to the conventional MPS algorithms where a given Hamiltonian is exponentiated to obtain the evolution operator, the unitary evolution operator is defined in the discrete-time quantum walk. Therefore, we do not need a Suzuki-Trotter expansion for numerical MPS simulations. The implementation below is numerically exact for the precision determined by the truncation tolerance.

For a single spinless particle moving on a lattice, a straightforward MPS representation is to associate a basis composed of two states for each lattice site. These states correspond to the vacuum and particle (being present on the site) states. (Note that this is not the most efficient representation because the MPS ansatz spans a 2^N dimensional physical Hilbert space including the no particle vacuum state as well as many-particle states with a maximum of one particle per site.) For a quantum walk, the local basis can be extended to include the coin degrees of freedom such that

$$\begin{aligned} |q_n = 0\rangle &\leftrightarrow |\text{vacuum}, n\rangle, \\ |q_n = 1\rangle &\leftrightarrow |c = 0, n\rangle, \\ |q_n = 2\rangle &\leftrightarrow |c = 1, n\rangle \end{aligned} \tag{5.13}$$

forming a three-dimensional basis and $|c, n\rangle$ are walker states defined in Sec. 4.2.

The unitary walk operator $\hat{W}$ consists of the successive application of the coin $\hat{C}$ and shift $\hat{T}$ operators. With the above identification of the local basis, $\hat{C}$ can be implemented as

$$\mathbf{I}_1 \oplus \exp\left(-i\theta\mathbf{X}\right) \leftrightarrow \hat{C} \tag{5.14}$$

where the matrix representation on the left is contracted with the physical index q_n of the local tensors at each site n.

The conditional shift operator $\hat{T}$ can be broken into the left $\hat{T}_{\mathrm{L}} = \sum_n |c=1,n\rangle\langle c=1,n+1|$ and the right $\hat{T}_{\mathrm{R}} = \sum_n |c=0,n+1\rangle\langle c=0,n|$ shift operators, which can be implemented by the two-site application of the following matrices

$$\begin{pmatrix} 1 & 0 & 0 \\ 0 & 0 & 0 \\ 0 & 0 & 1 \end{pmatrix}_n \otimes \begin{pmatrix} 1 & 0 & 0 \\ 0 & 1 & 0 \\ 0 & 0 & 1 \end{pmatrix}_{n+1} + \begin{pmatrix} 0 & 1 & 0 \\ 0 & 0 & 0 \\ 0 & 0 & 0 \end{pmatrix}_n \otimes \begin{pmatrix} 0 & 0 & 0 \\ 1 & 0 & 0 \\ 0 & 0 & 0 \end{pmatrix}_{n+1} \leftrightarrow \hat{T}_{\mathrm{R}} \tag{5.15}$$

$$\begin{pmatrix} 1 & 0 & 0 \\ 0 & 1 & 0 \\ 0 & 0 & 1 \end{pmatrix}_{n-1} \otimes \begin{pmatrix} 1 & 0 & 0 \\ 0 & 1 & 0 \\ 0 & 0 & 0 \end{pmatrix}_n + \begin{pmatrix} 0 & 0 & 0 \\ 0 & 0 & 0 \\ 1 & 0 & 0 \end{pmatrix}_{n-1} \otimes \begin{pmatrix} 0 & 0 & 1 \\ 0 & 0 & 0 \\ 0 & 0 & 0 \end{pmatrix}_n \leftrightarrow \hat{T}_{\mathrm{L}} \tag{5.16}$$

which are contracted with physical indices of sites n and $n+1$. Since $\hat{T}_{\mathrm{L}}$ and $\hat{T}_{\mathrm{R}}$ act on different coin states, they commute with each other. Therefore, the order of their application does not matter. However, for both of them, the even- and odd-bond hopping terms do not commute with each other. To avoid commutation errors, when sweeping over consecutive lattice bonds from left to right, $\hat{T}_{\mathrm{L}}$ can be applied. Similarly, when the sweep direction is switched $\hat{T}_{\mathrm{R}}$ can be applied from right to left. [4]

The local spins can be included by extending the local basis as a direct product with that of the local spin $|s_n\rangle$ giving a $3\times 2 = 6$ dimensional local Hilbert space. (For a single walker, the bond arrangement is such that non-zero amplitudes only appear for states with $q_n = 0$ for all n except one.) Finally, the matrix-product-operator for the interaction $\hat{M}$ can be implemented with the following matrix

$$[\mathbf{1}_1 \oplus \mathbf{0}_2] \otimes \mathbf{I}_2 + [\mathbf{0}_1 \oplus \mathbf{I}_2] \otimes \exp(-i\phi\mathbf{X}) \leftrightarrow \hat{M}, \tag{5.17}$$

which is again to be applied at every site n to the tensor $A^{q_n s_n}_{b_{n-1},b_n}$ with bond indices b_{n-1} and b_n to the left and right, respectively. In fact, the combination $\hat{C}\hat{M}$ can be performed together. Each step of the time evolution $\hat{W}_M = \hat{T}\hat{C}\hat{M}$ is composed of consecutive application of the on-site coin and interaction operators and a single sweep of the right and left translation operators.

To compute the spin expectations, we extend the Pauli operators to include the coin space. For instance, Pauli X operator, $\hat{X}$, is replaced with

$$[\mathbf{I}_1 \oplus \mathbf{I}_2] \otimes \mathbf{X} \leftrightarrow \hat{X}_n, \tag{5.18}$$

[4] Note that in Suzuki-Trotter expansion, the error due to the non-commuting terms in the Hamiltonian scales as a power of the time-step, where the power is determined by the order of expansion (See Sec. 2.4). Therefore, time-step should be small to reduce the error, which increases simulation time in general. Here, the size of the time-step does not have an effect on the error.

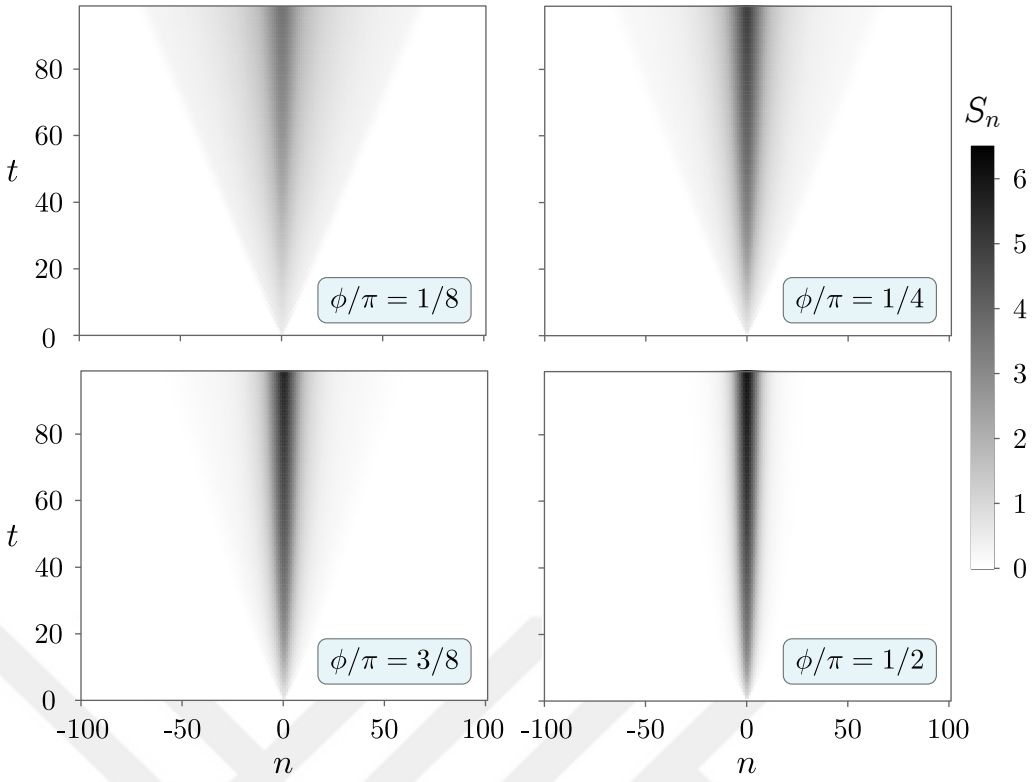

Figure 5.5 : Entanglement entropy between bi-partite partitions of the chain at the n^{th} site, S_n, as a function of time.

If the state is in canonical form with respect to site n, then computing the expectation $\langle \hat{X}_n \rangle$ reduces to the contraction of the above operator with the local tensor and its Hermitian conjugate, i.e.,

$$\langle \hat{X}_n \rangle = \sum_{\substack{q_n s_n, q'_n s'_n, \\ b_n, b_{n-1}}} \left(A^{q'_n s'_n}_{b_{n-1}, b_n} \right)^* [[\mathbf{I}_1 \oplus \mathbf{I}_2] \otimes \mathbf{X}]_{q'_n s'_n, q_n s_n} A^{q_n s_n}_{b_{n-1}, b_n}. \tag{5.19}$$

We perform a numerically exact time evolution employing the above ansatz up to $t = 100$ time steps. In our simulations, we choose the truncation tolerance as $\delta = 10^{-15}$. The maximum bond dimension at the end of the simulations becomes $D \sim 900$ for the bond in the middle of the chain where the quantum walker starts at $t = 0$. As seen from Eq. (2.3), bond dimension and entanglement entropy are directly related. In Fig. 5.5, we show how the von Neuman entropy between partitions separated at the n^{th} site, S_n, changes along the chain as a function of time. Since the local spins do not interact directly, the spread of the entanglement entropy is mediated by the walker. For $\phi < \pi/4$, ballistic spread of the walker causes spread of the entanglement with constant speed as well, whereas partial localization of the walker yields a slower entanglement spread near the origin. As the interaction strength ϕ increases further, ballistic spread

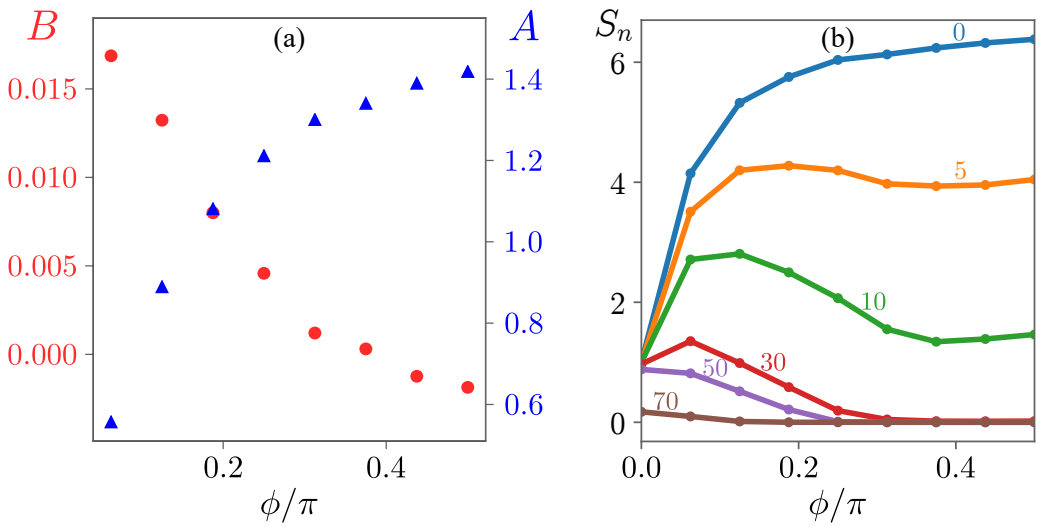

Figure 5.6 : (a) The logarithmic, A, and the linear, B, contributions to the growth of the entanglement entropy, S (see Eq.(5.20)). (b) Entanglement entropy between bi-partite partitions of the chain at the n^{th} site, S_n, as a function of the angle ϕ (b) after 100 time steps.

of the entanglement is suppressed and the entanglement entropy grows sub-linearly in time. For a quantitative analysis, we tested a fitting function for time dependence of $S(t)$ to be a combination of logarithmic and linear functions of time, so that

$$S(t) = A\log t + Bt. \tag{5.20}$$

In Fig. 5.6 (a), we show how the coefficients A and B change with the interaction strength, ϕ. The contribution of the logarithmic growth, A, increases with ϕ, whereas the linear contribution, B, decreases. Therefore, as the walker gets more localized, the sub-linear growth of the entanglement prevails. In Fig. 5.6 (b), we show how S_n varies with ϕ for different partitionings of the spin chain at $t = 100$. The result for the partitioning at the origin (site $n = 0$) is shown in Fig. 5.4(b), as well. When the chain is split in the middle, S_n monotonically increases with increasing ϕ. For $n \neq 0$, S_n depends on the localization of the quantum walker. Near the origin, S_n is generally higher in the regime where the walker is partially localized, whereas it converges to its minimum value when the walker is exponentially localized.

We also note that for finite system calculations the entanglement entropy saturates at values that scale with the size of the system which implies a volume law for the model. The saturation of $S(t)$ is shown in Fig. 5.7(a) for different values of ϕ and a system with $N = 15$. For this system size, the saturation takes $t \sim 10^2 - 10^3$ depending on the localization of the walker. The strongly localized ($\phi > \pi/4$) systems saturate faster

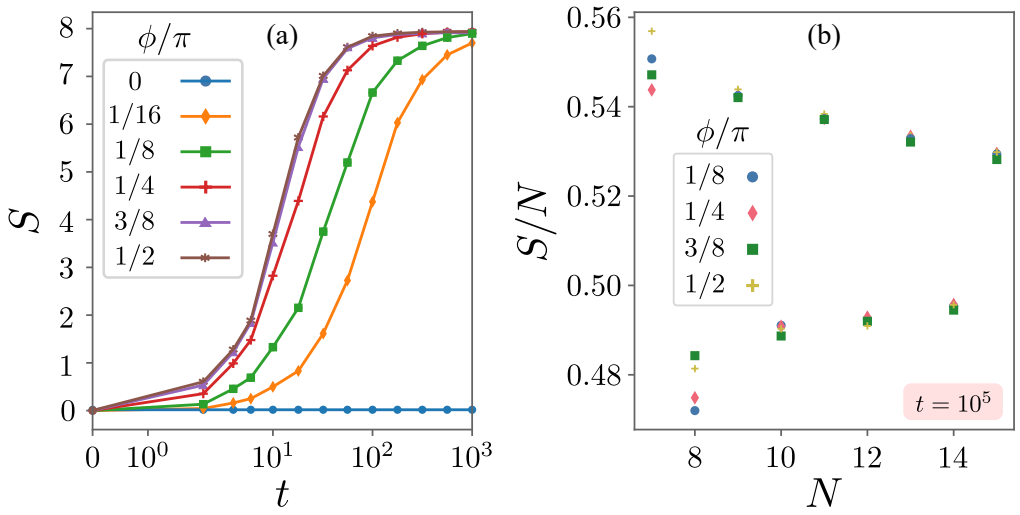

Figure 5.7 : (a) Entanglement entropy as a function of time for a lattice with $N = 15$ for different values of ϕ. (Partitioning of the system is done in half, i.e. $7+8 = 15$, and only spins on the left are traced out for these calculations.) For $\phi > \pi/4$, S grows as $\sim \log t$ in the second decade of the evolution before the systems eventually thermalize. (b) Entanglement entropy per site S/N as a function of system size N after thermalization at $t = 10^5$ approaches a constant indicating a volume law.

than partially localized ($\phi < \pi/4$) ones but the saturation value is determined by the system size. The scaling of the long-time value of S with N is shown in Fig. 5.7(b) where the entropy per sites converges to a constant value.

5.8 Effect of a Symmetry Breaking Field

Disorder-free localization is strongly related to the extensive number of conserved quantities [175]. In this section, we observe the effect of a symmetry breaking field, which we take as a uniform field along the z-direction. We apply a field operator

$$F = \prod_n e^{-i\phi' \hat{Z}_n} \tag{5.21}$$

at every time step and consider an evolution of 40 steps from the same initial state as in the main text. We concentrate on two interaction angles. At $\phi = \pi/8$ (Fig. 5.8 upper panel), localization is partial and the tails at the two ends persist. When a small field such as $\phi' = \pi/100$ is present, the localization around the initial state decreases substantially, but the tails are not affected too much (Fig. 5.8a). As we increase ϕ' further, the distribution becomes more uniform around the initial site and it drops around the tails, as well. Due to the diminishing of the localization with the uniform field, for the first 30 time steps variance is higher compared to the $\phi' = 0$ case and it is approximately the same for both field angles. However, for $\phi' = 2\pi/100$,

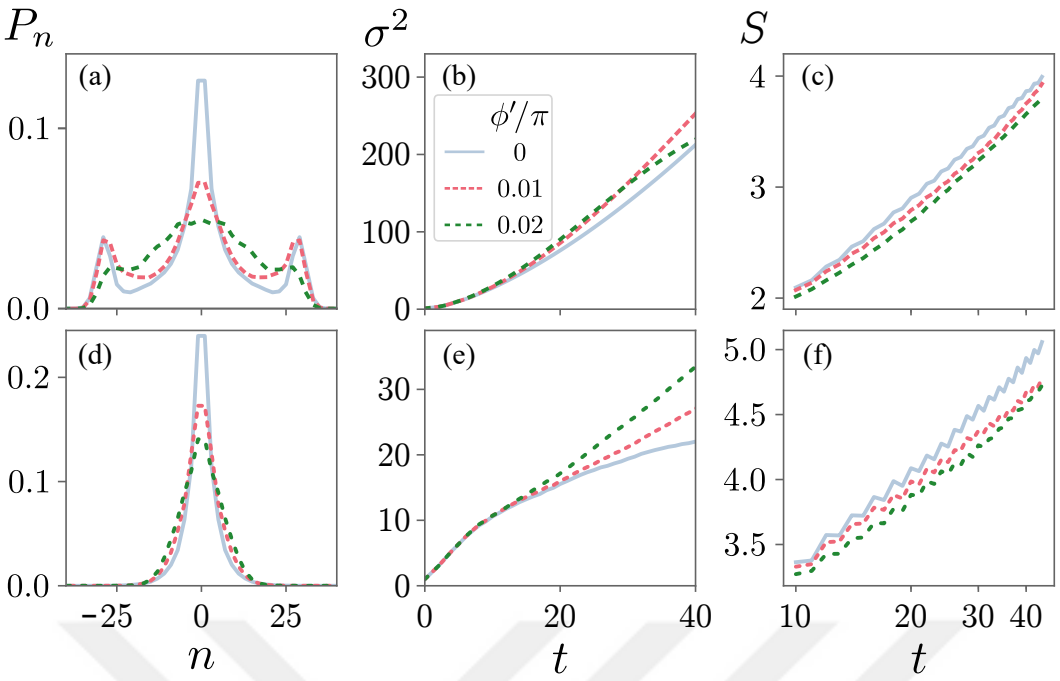

Figure 5.8 : Effect of the symmetry breaking field in Eq. (5.21) for the interaction angles $\phi = \pi/8$ (upper panel) and $\phi = 3\pi/8$ (lower panel). (a) and (d) show the probability distribution. Time behavior of the variance in position space is shown in (b) and (e). Time behavior of the entanglement entropy is shown in (c) and (f).

the probabilities around the tails also drop yielding a slower spread and, therefore, a lower variance (Fig. 5.8b) which is similar to a diffusive behavior. We now look at an angle for which the walker is completely localized (Fig. 5.8 lower panel). At $\phi = \pi/8$, the effect of the symmetry breaking field on the localization is lessened compared to the previous example. Though localization is diminished, it still persists for both field angles (Fig. 5.8d). As the field strength increases, time behavior of the variance becomes similar to classical diffusion, where variance increases linearly in time (Fig. 5.8e). For both interaction angles, the symmetry breaking field does not change the sublinear growth of the entanglement entropy (Fig. 5.8(c) and (f)).

5.9 Discussion and Conclusion

We have studied disorder-free localization of a quantum walker coupled to local spins on a one-dimensional lattice. Similar to models of quantum walks on graphs coupled to spins living on nodes [179] or links [181], the local spins in our model live on lattice sites and do not act on the coin. The Hamiltonian and the initial spin state we have chosen are translationally invariant, yet localization occurs merely due to the interactions between the walker and the local spins. Therefore, our model exhibits

a discrete-time version of the DFL introduced recently [175] in a periodically driven system. One of the advantages of our model is the presence of the extensive number of conserved moments which provides a computationally easier method to analyze the spread of the walk. Due to the conserved quantities, the evolution problem reduces to that of a disordered walk. Since we chose the initial state to be a superposition of all possible spin disorder configurations, the spatial probability of the walker can be obtained through an ensemble averaging over all possible spin configurations.

We have observed two regimes of localization depending on the strength of the interaction between the walker and the local spins. For weak coupling, similar to the mobility edges found in three-dimensional Anderson localization [187] and many-body localized systems under weak disorder [169], the localized states are concentrated near the band edges of the spectrum. As a result, the walker gets partially localized around the origin and the ballistic tails are suppressed. The oscillations in the probability distribution become smooth due to the decoherence effects with the spin environment. As the interaction strength increases, the band gap gets smaller and the eigenstates become more localized. As the coupling increases, the band gap closes and the ballistic tails disappear with the walker being completely localized. The localization length is reduced down to the order of the lattice spacing and does not vary appreciably as a function of the interaction strength above the critical value. General wisdom is that one-dimensional systems exhibit Anderson localization under continuous-time evolution for arbitrarily small disorder. Exceptional cases usually possess correlated disorder or long-range interactions. The emergent disorder in our model is uncorrelated disorder. The motion of the quantum walker and the interaction between the walker and the local spins are short ranged. Therefore, with our intermediate time and corresponding system size simulations we cannot rule out the possibility of finite size effects. On the other hand, in contrast to the Hamiltonian models, the discrete-time dynamics here is given by a unitary step operator. There are also suggested models of many-body localization where stroboscopic dynamics such as driving by an external light may cause delocalization [188–191].

We think that the apparent transition around $\phi = \pi/4$ in our model can also be related to the natural length scale in the model which is the lattice spacing. A possible explanation of the results for $\phi < \pi/4$ could be that the Anderson localization length

is larger or comparable to our system size, thus the finite size effect mentioned above would be relevant. For $\phi > \pi/4$, the conclusion is that the Anderson localization length becomes comparable to the lattice spacing. Therefore, the change of the localization length with ϕ could be the reason behind the different behaviour. This is in agreement with the sharp features in the quasi-energy spectrum in the sense that for $\phi > \pi/4$ there is no band gap and we find localized states for almost all quasi-energy values.

We have tested robustness of the quantum walker's localization by applying uniform field to the local spins. When the field is along x-direction, the spatial probability distribution is not affected, since the local integrals of motion are conserved. However, when we add a symmetry breaking field, i.e. along z-direction, the results resemble those of a classical random walk (see Sec. 5.8). The persistence of localization and the sublinear growth of entanglement entropy is likely to be related to the phenomenon of prethermalization explored in integrable models [192–196].

We have introduced a straightforward implementation of the MPS ansatz on the lattice which is essential to study the spin dynamics and the entanglement entropy of different subdivisions of the spin chain. The discrete-time unitary evolution can be implemented without any formal approximations. Our results show that the growth of the entanglement entropy depends on the interaction strength. In the intermediate time scale of our simulations, we observed that for small interaction strengths, the partial localization of the walker yields linear spread of the entanglement towards edges combined with sublinear spread around the origin. As the interaction gets stronger, linear spread is suppressed while the sublinear spread prevails and causes the growth rate of the entanglement to increase. For strong coupling no ballitic spread is observed and the growth rate saturates when the localization length becomes comparable to the lattice spacing. The sublinear suppression of the entanglement growth is similar to some of the DFL and MBL systems previously studied in the literature.

Our work connects quantum walk models as examples of periodically driven systems to the recent studies on disorder-free localizationand related areas. The use of MPS and tensor network states in general can lead to further investigations of quantum walks interacting with local degrees of freedom. A natural extension of our study would be to consider a quantum walk on a higher dimensionsional spin environment where a transition to classical random walk and a diffusive spread is expected. Furthermore,

the fate of localization in two and three dimensional spin environments can be studied. It would also be interesting to analyze the connection between localization and non-Markovianity in similar models.

Our sampling results are experimentally feasible with current experimental technology. The electro-optical modulators (EOMs) presented in the time-multiplexing quantum walk scheme make it possible to introduce position-dependent random phases for the walker [70, 154, 164, 165, 197]. EOMs affect the light pulses (walker) going through a fiber loop in the time domain representing the position space. Therefore, appropriate programming for EOMs may allow the realization of any binary disordered landscape presented in our model, and the localization results could be obtained by averaging over different realizations.

6. CONCLUSION

In the scope of this thesis, we have developed a numerical library employing MPS formalism to study one-dimensioal coupled cavity arrays and quantum walks with impurities. We have shown that our MPS library is applicable to both systems. We have also studied different aspects of these systems such as bound state formation, dynamical localization, entanglement growth and non-Markovianity.

We have simulated photon dynamics in a coupled cavity array interacting with a TLS in different coupling regimes. In the strong coupling regime where RWA is applicable, the problem can be solved using exact diagonalization. In this regime, the results we obtained from MPS simulations were in complete agreement with the exact diagonalization results, exhibiting the very well-known exponential decay of the TLS from its excited state and the unbounded expansion of all the emitted photons.

As the coupling strength increases RWA breaks down due to the photon cloud bounded to the TLS. For the intermediate coupling strengths, which can be called "perturbative coupling regime", RWA coupling regime is still applicable after a basis transformation called polaron transformation is applied to the Hamiltonian. In this new basis the TLS and the photonic modes in its vicinity are in an entangled state which captures most of the interaction between the TLS and the photons in the perturbative regime. We have shown that both the MPS simulations and RWA with polaron transformation yield the same decay of the TLS which has a slower rate compared to the results obtained from RWA without polaron transformation and converges to the same non-zero value. The slow decay rate is due to the decrease in the effective coupling in the polaron basis. The non-zero value of the excited states population in the long time limit is the sign of the photon cloud permanently bounded to the TLS. On the other hand, when we examined the photon profiles after the time evolution, we observed that the photon numbers in the vicinity of the TLS are non-zero only for the results obtained from the MPS, whereas the photon profiles obtained from RWA with and without the polaron transform are exactly the same. This shows that the restrictions imposed by the RWA,

i.e. elimination of the terms which project to the multiple excitation subspaces in the Hamiltonian, causes the polaron transformation fail to capture the effect of the bound state in the photon profile. As the coupling strength is increased beyond the perturbative regime, the difference of the MPS results become more prominent. The photon numbers near the TLS become higher on a broader area and the excited state's population converges to a slightly higher value compared to the results obtained from RWA with polaron transformation.

Discrete-time quantum walks with different impurity models have been widely studied in the literature [145, 147, 148, 198]. In this thesis we have studied two types of impurity models. Firstly, we considered a discrete-time quantum walk with a phase impurity. We mainly focused on the relationship between the bound states, dynamical localization and non-Markovianity effects in this model. The bound states of this walk have been obtained previously [141]. We have proposed an alternative method employing transfer matrices. We have compared the bound state and dynamical localization studying two quantities which are independent of the initial state; the effective localization length averaged over all eigenstates and an average participation ratio resulting from the time evolution for all initial state starting from the impurity site. Both quantities increase as the phase increases and the amount of increase changes abruptly when the number bound states jumps from two to four. This shows that the localization and number of bound states determine the dynamical localization of the evolved system.

In order to study non-Markovianity in this model, we have used the BLP and RHP measures. These quantities aim to measure the information flowing back to a system from its environment. Our analysis showed that the properties of the bound states, play an important role in non-Markovianity. When both reflection symmetric and anti-symmetric bound state pairs are present both measures increase with the phase and become maximum when the effective localization length of the eigenstates is maximum. Despite this similarity, when there is only one pair of bound states, the non-Markovianity measures yield completely different results. In this case, the BLP measure increases with the increasing phsae, until it abruptly drops when new bound state pair emerges. On the other hand, the RHP measure becomes very small, when there is only one type of bound state symmetry.

The second quantum walk model we have studied is a quantum walk coupled to a spin chain. We have analyzed localization of a quantum walker on a disorder-free spin chain. Although both the Hamiltonian and the initial spin state are translationally invariant, the interaction between the walker and local spins yields to dynamical localization of the walker. We have used two different methods to study the spatial probability distribution. The extensive number of conserved quantities made it possible to take an ensamble average over a random sampling of spin configurations. We also used an MPS algorithm for comparison and found that both methods yield the same results. We have observed two regimes of localization depending on the interaction strength. Below a critical interaction value, the energy spectrum is gapped and only some of the eigenstates are localized. Therefore, the walker gets partially localized in our intermediate time simulations. On the other hand, the band gap closes above the critical value and the walker becomes exponentially localized. The MPS algorithm also enabled us to study dynamics of the spin chain and the entanglement entropy. Similar to the MBL systems and other DFL models, the entanglement entropy grows sublinearly in time.

REFERENCES

[1] **Hartmann, M.J.**, **Brandao, F.G. and Plenio, M.B.** (2008). Quantum many-body phenomena in coupled cavity arrays, *Laser & Photonics Reviews*, *2*(6), 527–556.

[2] **Verstraete, F.**, **Murg, V. and Cirac, J.I.** (2008). Matrix product states, projected entangled pair states, and variational renormalization group methods for quantum spin systems, *Advances in Physics*, *57*(2), 143–224.

[3] **Orús, R.** (2014). A practical introduction to tensor networks: Matrix product states and projected entangled pair states, *Annals of Physics*, *349*, 117–158.

[4] **Eisert, J.**, **Cramer, M. and Plenio, M.B.** (2010). Colloquium: Area laws for the entanglement entropy, *Reviews of Modern Physics*, *82*(1), 277.

[5] **Klümper, A.**, **Schadschneider, A. and Zittartz, J.** (1993). Matrix product ground states for one-dimensional spin-1 quantum antiferromagnets, *EPL (Europhysics Letters)*, *24*(4), 293.

[6] **Lange, C.**, **Klümper, A. and Zittartz, J.** (1994). Exact groundstates for antiferromagnetic spin-one chains with nearest and next-nearest neighbour interactions, *Zeitschrift für Physik B Condensed Matter*, *96*(2), 267–270.

[7] **Östlund, S. and Rommer, S.** (1995). Thermodynamic limit of density matrix renormalization, *Physical review letters*, *75*(19), 3537.

[8] **Rommer, S. and Östlund, S.** (1997). Class of ansatz wave functions for one-dimensional spin systems and their relation to the density matrix renormalization group, *Physical review b*, *55*(4), 2164.

[9] **Perez-Garcia, D.**, **Verstraete, F.**, **Wolf, M.M. and Cirac, J.I.** (2006). Matrix product state representations, *arXiv preprint quant-ph/0608197*.

[10] **Schollwöck, U.** (2011). The density-matrix renormalization group in the age of matrix product states, *Annals of physics*, *326*(1), 96–192.

[11] **Breuer, H.P. and Petruccione, F.** (2002). *The Theory of Open Quantum Systems*, Oxford University Press.

[12] **Karski, M.**, **Förster, L.**, **Choi, J.M.**, **Steffen, A.**, **Alt, W.**, **Meschede, D. and Widera, A.** (2009). Quantum Walk in Position Space with Single Optically Trapped Atoms, *Science*, *325*(5937), 174–177.

[13] **Schmitz, H.**, **Matjeschk, R.**, **Schneider, C.**, **Glueckert, J.**, **Enderlein, M.**, **Huber, T. and Schaetz, T.** (2009). Quantum Walk of a Trapped Ion in Phase Space, *Phys. Rev. Lett.*, *103*, 090504.

[14] **Zähringer, F.**, **Kirchmair, G.**, **Gerritsma, R.**, **Solano, E.**, **Blatt, R. and Roos, C.F.** (2010). Realization of a Quantum Walk with One and Two Trapped Ions, *Phys. Rev. Lett.*, *104*, 100503.

[15] **Bakr, W.S.**, **Gillen, J.I.**, **Peng, A.**, **Fölling, S. and Greiner, M.** (2009). A quantum gas microscope for detecting single atoms in a Hubbard-regime optical lattice, *Nature*, *462*(7269), 74–77.

[16] **Preiss, P.M.**, **Ma, R.**, **Tai, M.E.**, **Lukin, A.**, **Rispoli, M.**, **Zupancic, P.**, **Lahini, Y.**, **Islam, R. and Greiner, M.** (2015). Strongly correlated quantum walks in optical lattices, *Science*, *347*(6227), 1229–1233.

[17] **Sherson, J.F.**, **Weitenberg, C.**, **Endres, M.**, **Cheneau, M.**, **Bloch, I. and Kuhr, S.** (2010). Single-atom-resolved fluorescence imaging of an atomic Mott insulator, *Nature*, *467*(7311), 68–72.

[18] **Chandrashekar, C. and Busch, T.** (2015). Localized quantum walks as secured quantum memory, *EPL (Europhysics Letters)*, *110*(1), 10005.

[19] **Guillet, S.**, **Roget, M.**, **Arrighi, P. and Di Molfetta, G.** (2019). The Grover search as a naturally occurring phenomenon, *arXiv preprint arXiv:1908.11213*.

[20] **Leggett, A.J.**, **Chakravarty, S.**, **Dorsey, A.T.**, **Fisher, M.P.**, **Garg, A. and Zwerger, W.** (1987). Dynamics of the dissipative two-state system, *Reviews of Modern Physics*, *59*(1), 1.

[21] **Ingold, G.L.**, (2002). Path integrals and their application to dissipative quantum systems, Coherent Evolution in Noisy Environments, Springer, pp.1–53.

[22] **Hinds, E.** (1994). Perturbative cavity quantum electrodynamics, *Cavity Quantum Electrodynamics*, 1–56.

[23] **Kimble, H.** (1994). *Advances in Atomic, Molecular, and Optical Physics, Supplement 2: Cavity Quantum Electrodynamics*, Academic Press, Boston.

[24] **Kimble, H.J.** (1998). Strong interactions of single atoms and photons in cavity QED, *Physica Scripta*, *1998*(T76), 127.

[25] **Wallraff, A.**, **Schuster, D.I.**, **Blais, A.**, **Frunzio, L.**, **Huang, R.S. and Majer, J… Schoelkopf, R.J.** (2004). Strong coupling of a single photon to a superconducting qubit using circuit quantum electrodynamics, *Nature*, *431*(7005), 162–167.

[26] **Raimond, J.M. and Haroche, S.** (2006). Exploring the quantum, *Oxford University Press*, *82*, 86.

[27] **Haroche, S.** (2013). Nobel Lecture: Controlling photons in a box and exploring the quantum to classical boundary, *Reviews of Modern Physics*, *85*(3), 1083.

[28] **Reiserer, A. and Rempe, G.** (2015). Cavity-based quantum networks with single atoms and optical photons, *Reviews of Modern Physics*, *87*(4), 1379.

[29] **Calajó, G.**, **Ciccarello, F.**, **Chang, D. and Rabl, P.** (2016). Atom-field dressed states in slow-light waveguide QED, *Phys. Rev. A*, *93*, 033833.

[30] **Fang, Y.L.L. and Baranger, H.U.** (2015). Waveguide QED: Power spectra and correlations of two photons scattered off multiple distant qubits and a mirror, *Phys. Rev. A*, *91*, 053845.

[31] **Paulisch, V.**, **Kimble, H. and González-Tudela, A.** (2016). Universal quantum computation in waveguide QED using decoherence free subspaces, *New Journal of Physics*, *18*(4), 043041.

[32] **Lodahl, P.**, **Mahmoodian, S. and Stobbe, S.** (2015). Interfacing single photons and single quantum dots with photonic nanostructures, *Reviews of Modern Physics*, *87*(2), 347.

[33] **Solano, P.**, **Grover, J.A.**, **Hoffman, J.E.**, **Ravets, S.**, **Fatemi, F.K.**, **Orozco, L.A. and Rolston, S.L.**, (2017). Optical nanofibers: a new platform for quantum optics, Advances In Atomic, Molecular, and Optical Physics, volume 66, Elsevier, pp.439–505.

[34] **Niemczyk, T.**, **Deppe, F.**, **Huebl, H.**, **Menzel, E.**, **Hocke, F.**, **Schwarz, MJ... Gross, R.** (2010). Circuit quantum electrodynamics in the ultrastrong-coupling regime, *Nature Physics*, *6*(10), 772.

[35] **Forn-Díaz, P.**, **Lisenfeld, J.**, **Marcos, D.**, **García-Ripoll, J.J.**, **Solano, E.**, **Harmans, C. and Mooij, J.** (2010). Observation of the Bloch-Siegert shift in a qubit-oscillator system in the ultrastrong coupling regime, *Physical review letters*, *105*(23), 237001.

[36] **Bourassa, J.**, **Gambetta, J.M.**, **Abdumalikov Jr, A.A.**, **Astafiev, O.**, **Nakamura, Y. and Blais, A.** (2009). Ultrastrong coupling regime of cavity QED with phase-biased flux qubits, *Physical Review A*, *80*(3), 032109.

[37] **Ciuti, C.**, **Bastard, G. and Carusotto, I.** (2005). Quantum vacuum properties of the intersubband cavity polariton field, *Physical Review B*, *72*(11), 115303.

[38] **Günter, G.**, **Anappara, A.A.**, **Hees, J.**, **Sell, A.**, **Biasiol, G.**, **Sorba, L... Huber, R.** (2009). Sub-cycle switch-on of ultrastrong light–matter interaction, *Nature*, *458*(7235), 178.

[39] **Anappara, A.A.**, **De Liberato, S.**, **Tredicucci, A.**, **Ciuti, C.**, **Biasiol, G.**, **Sorba, L. and Beltram, F.** (2009). Signatures of the ultrastrong light-matter coupling regime, *Physical Review B*, *79*(20), 201303.

[40] **Geiser, M.**, **Castellano, F.**, **Scalari, G.**, **Beck, M.**, **Nevou, L. and Faist, J.** (2012). Ultrastrong coupling regime and plasmon polaritons in parabolic semiconductor quantum wells, *Physical Review Letters*, *108*(10), 106402.

[41] **Forn-Díaz, P.**, **García-Ripoll, J.J.**, **Peropadre, B.**, **Orgiazzi, J.L.**, **Yurtalan, M.**, **Belyansky, R... Lupascu, A.** (2017). Ultrastrong coupling of a single artificial atom to an electromagnetic continuum in the nonperturbative regime, *Nature Physics*, *13*(1), 39.

[42] **Yoshihara, F.**, **Fuse, T.**, **Ashhab, S.**, **Kakuyanagi, K.**, **Saito, S. and Semba, K.** (2017). Superconducting qubit–oscillator circuit beyond the ultrastrong-coupling regime, *Nature Physics*, *13*(1), 44.

[43] **Schoelkopf, R. and Girvin, S.** (2008). Wiring up quantum systems, *Nature*, *451*(7179), 664–669.

[44] **Aharonov, Y.**, **Davidovich, L. and Zagury, N.** (1993). Quantum random walks, *Phys. Rev. A*, *48*, 1687–1690.

[45] **Venegas-Andraca, S.E.** (2012). Quantum walks: a comprehensive review, *Quantum Inf. Process.*, *11*(5), 1015–1106.

[46] **Kempe, J.** (2003). Quantum random walks: An introductory overview, *Contemp. Phys.*, *44*(4), 307–327.

[47] **Ambainis, A.** (2003). Quantum walks and their algorithmic applications, *Int. J. Quantum Inf.*, *01*(04), 507–518.

[48] **Shenvi, N.**, **Kempe, J. and Whaley, K.B.** (2003). Quantum random-walk search algorithm, *Physical Review A*, *67*(5), 052307.

[49] **Childs, A.M. and Goldstone, J.** (2004). Spatial search by quantum walk, *Physical Review A*, *70*(2), 022314.

[50] **Ambainis, A.**, **Kempe, J. and Rivosh, A.** (2004). Coins make quantum walks faster, *arXiv preprint quant-ph/0402107*.

[51] **Abal, G.**, **Donangelo, R.**, **Marquezino, F.L. and Portugal, R.** (2010). Spatial search in a honeycomb network, *arXiv preprint arXiv:1001.1139*.

[52] **Paparo, G.D. and Martin-Delgado, M.** (2012). Google in a quantum network, *Scientific reports*, *2*, 444.

[53] **Paparo, G.D.**, **Müller, M.**, **Comellas, F. and Martin-Delgado, M.A.** (2013). Quantum google in a complex network, *Scientific reports*, *3*, 2773.

[54] **Paparo, G.D.**, **Müller, M.**, **Comellas, F. and Martin-Delgado, M.A.** (2014). Quantum google algorithm, *The European Physical Journal Plus*, *129*(7), 150.

[55] **Lovett, N.B.**, **Cooper, S.**, **Everitt, M.**, **Trevers, M. and Kendon, V.** (2010). Universal quantum computation using the discrete-time quantum walk, *Phys. Rev. A*, *81*, 042330.

[56] **Buerschaper, O. and Burnett, K.** Stroboscopic quantum walks, `arXiv: quant-ph/0406039v2`.

[57] **Oka, T.**, **Konno, N.**, **Arita, R. and Aoki, H.** (2005). Breakdown of an Electric-Field Driven System: A Mapping to a Quantum Walk, *Phys. Rev. Lett.*, *94*, 100602.

[58] **Kurzyński, P. and Wójcik, A.** (2011). Discrete-time quantum walk approach to state transfer, *Phys. Rev. A*, *83*, 062315.

[59] **Zhan, X.**, **Qin, H.**, **Bian, Z.h.**, **Li, J. and Xue, P.** (2014). Perfect state transfer and efficient quantum routing: A discrete-time quantum-walk approach, *Phys. Rev. A*, *90*, 012331.

[60] **Yalçınkaya, İ. and Gedik, Z.** (2015). Qubit state transfer via discrete-time quantum walks, *J. Phys. A*, *48*(22), 225302.

[61] **Štefaňák, M. and Skoupý, S.** (2016). Perfect state transfer by means of discrete-time quantum walk search algorithms on highly symmetric graphs, *Phys. Rev. A*, *94*, 022301.

[62] **Štefaňák, M. and Skoupý, S.** (2017). Perfect state transfer by means of discrete-time quantum walk on complete bipartite graphs, *Quantum Inf. Process.*, *16*(3), 72.

[63] **Kitagawa, T.**, **Rudner, M.S.**, **Berg, E. and Demler, E.** (2010). Exploring topological phases with quantum walks, *Phys. Rev. A*, *82*, 033429.

[64] **Kitagawa, T.** (2012). Topological phenomena in quantum walks: elementary introduction to the physics of topological phases, *Quantum Inf. Process.*, *11*(5), 1107–1148.

[65] **Cedzich, C.**, **Grünbaum, F.A.**, **Stahl, C.**, **Velázquez, L.**, **Werner, A.H. and Werner, R.F.** (2016). Bulk-edge correspondence of one-dimensional quantum walks, *J. Phys A: Math. Theor.*, *49*(21), 21LT01.

[66] **Cedzich, C.**, **Geib, T.**, **Grünbaum, F.A.**, **Stahl, C.**, **Velázquez, L.**, **Werner, A.H. and Werner, R.F.** (2018). The Topological Classification of One-Dimensional Symmetric Quantum Walks, *Ann. Henri Poincaré*, *19*(2), 325–383.

[67] **Cedzich, C.**, **Geib, T.**, **Stahl, C.**, **Velázquez, L.**, **Werner, A.H. and Werner, R.F.** (2018). Complete homotopy invariants for translation invariant symmetric quantum walks on a chain, *Quantum*, *2*, 95.

[68] **Du, J.**, **Li, H.**, **Xu, X.**, **Shi, M.**, **Wu, J.**, **Zhou, X. and Han, R.** (2003). Experimental implementation of the quantum random-walk algorithm, *Physical Review A*, *67*(4), 042316.

[69] **Ryan, C.A.**, **Laforest, M.**, **Boileau, J.C. and Laflamme, R.** (2005). Experimental implementation of a discrete-time quantum random walk on an NMR quantum-information processor, *Physical Review A*, *72*(6), 062317.

[70] **Schreiber, A.**, **Cassemiro, K.N.**, **Potoček, V.**, **Gábris, A.**, **Mosley, P.J.**, **Andersson, E... Silberhorn, C.** (2010). Photons Walking the Line: A Quantum Walk with Adjustable Coin Operations, *Phys. Rev. Lett.*, *104*, 050502.

[71] **Broome, M.A.**, **Fedrizzi, A.**, **Lanyon, B.P.**, **Kassal, I.**, **Aspuru-Guzik, A. and White, A.G.** (2010). Discrete single-photon quantum walks with tunable decoherence, *Physical review letters*, *104*(15), 153602.

[72] **Perets, H.B.**, **Lahini, Y.**, **Pozzi, F.**, **Sorel, M.**, **Morandotti, R. and Silberberg, Y.** (2008). Realization of Quantum Walks with Negligible Decoherence in Waveguide Lattices, *Phys. Rev. Lett.*, *100*, 170506.

[73] **Danacı, B. and García-Ripoll, J.J.**, (2019), SeeMPS, `https://github.com/juanjosegarciaripoll/seemps`, [Online; accessed 10-March-2019].

[74] **Stewart, G.W.** (1993). On the early history of the singular value decomposition, *SIAM review*, *35*(4), 551–566.

[75] **Vidal, G.** (2003). Efficient Classical Simulation of Slightly Entangled Quantum Computations, *Phys. Rev. Lett.*, *91*, 147902.

[76] **Vidal, G.** (2004). Efficient Simulation of One-Dimensional Quantum Many-Body Systems, *Phys. Rev. Lett.*, *93*, 040502.

[77] **Suzuki, M.** (1990). Fractal decomposition of exponential operators with applications to many-body theories and Monte Carlo simulations, *Physics Letters A*, *146*(6), 319–323.

[78] **Suzuki, M.** (1991). General theory of fractal path integrals with applications to many-body theories and statistical physics, *Journal of Mathematical Physics*, *32*(2), 400–407.

[79] **Yahiaoui, R.**, **Chase, Z.A.**, **Kyaw, C.**, **Tay, F.**, **Baydin, A.**, **Noe II, G. T... Searles, T.A.** (2021). Tunable Plasmonic Ultrastrong Coupling: Emulating Dicke Physics at Room Temperature, *arXiv preprint arXiv:2108.02494*.

[80] **Solano, E.** (2011). The dialogue between quantum light and matter, *Physics*, *4*, 68.

[81] **Sánchez-Burillo, E.**, **Zueco, D.**, **Garcia-Ripoll, J. and Martin-Moreno, L.** (2014). Scattering in the ultrastrong regime: nonlinear optics with one photon, *Physical review letters*, *113*(26), 263604.

[82] **Scully, M.O. and Zubairy, M.S.** (1997). *Quantum optics*, Cambridge university press.

[83] **Cohen-Tannoudji, C.**, **Dupont-Roc, J. and Grynberg, G.** (1998). *Atom-photon interactions: basic processes and applications*.

[84] **Silbey, R. and Harris, R.A.** (1984). Variational calculation of the dynamics of a two level system interacting with a bath, *The Journal of chemical physics*, *80*(6), 2615–2617.

[85] **Harris, R.A. and Silbey, R.** (1985). Variational calculation of the tunneling system interacting with a heat bath. II. Dynamics of an asymmetric tunneling system, *The Journal of chemical physics*, *83*(3), 1069–1074.

[86] **Fevens, T. and Jiang, H.** (1999). Absorbing boundary conditions for the Schrödinger equation, *SIAM Journal on Scientific Computing*, *21*(1), 255–282.

[87] **Selstø, S. and Kvaal, S.** (2010). Absorbing boundary conditions for dynamical many-body quantum systems, *Journal of Physics B: Atomic, Molecular and Optical Physics*, *43*(6), 065004.

[88] **Gonoskov, A. and Gonoskov, I.** (2006). Suppression of reflection from the grid boundary in solving the time-dependent Schroedinger equation by split-step technique with fast Fourier transform, *arXiv preprint physics/0607120*.

[89] **Ishizaki, A. and Fleming, G.R.** (2009). On the adequacy of the Redfield equation and related approaches to the study of quantum dynamics in electronic energy transfer, *The Journal of chemical physics*, *130*(23), 234110.

[90] **Pachón, L.A. and Brumer, P.** (2012). Computational methodologies and physical insights into electronic energy transfer in photosynthetic light-harvesting complexes, *Physical Chemistry Chemical Physics*, *14*(29), 10094–10108.

[91] **Carmichael, H.J.** (2013). *Statistical methods in quantum optics 1: master equations and Fokker-Planck equations*, Springer Science & Business Media.

[92] **Weiss, U.** (2012). *Quantum dissipative systems*, volume 13, World scientific.

[93] **Cao, J.** (2000). Effects of bath relaxation on dissipative two-state dynamics, *The Journal of Chemical Physics*, *112*(15), 6719–6724.

[94] **Chin, A.W.**, **Prior, J.**, **Huelga, S.F. and Plenio, M.B.** (2011). Generalized polaron ansatz for the ground state of the sub-ohmic spin-boson model: An analytic theory of the localization transition, *Physical review letters*, *107*(16), 160601.

[95] **Tong, Q.J.**, **An, J.H.**, **Luo, H.G. and Oh, C.** (2011). Quantum phase transition in the delocalized regime of the spin-boson model, *Physical Review B*, *84*(17), 174301.

[96] **Xu, D. and Schulten, K.** (1994). Coupling of protein motion to electron transfer in a photosynthetic reaction center: investigating the low temperature behavior in the framework of the spin—boson model, *Chemical physics*, *182*(2-3), 91–117.

[97] **Lemmer, A.**, **Cormick, C.**, **Tamascelli, D.**, **Schaetz, T.**, **Huelga, S.F. and Plenio, M.B.** (2018). A trapped-ion simulator for spin-boson models with structured environments, *New Journal of Physics*, *20*(7), 073002.

[98] **Stefanou, N. and Modinos, A.** (1998). Impurity bands in photonic insulators, *Physical Review B*, *57*(19), 12127.

[99] **Yariv, A.**, **Xu, Y.**, **Lee, R.K. and Scherer, A.** (1999). Coupled-resonator optical waveguide:? a proposal and analysis, *Optics letters*, *24*(11), 711–713.

[100] **Rabi, I.** (1936). On the process of space quantization, *Physical Review*, *49*(4), 324.

[101] **Rabi, I.I.** (1937). Space quantization in a gyrating magnetic field, *Physical Review*, *51*(8), 652.

[102] **Astafiev, O.**, **Zagoskin, A.M.**, **Abdumalikov, A.A.**, **Pashkin, Y.A.**, **Yamamoto, T.**, **Inomata, K... Tsai, J.S.** (2010). Resonance Fluorescence of a Single Artificial Atom, *Science*, *327*(5967), 840–843.

[103] **Hoi, I.C.**, **Wilson, C.M.**, **Johansson, G.**, **Palomaki, T.**, **Peropadre, B. and Delsing, P.** (2011). Demonstration of a Single-Photon Router in the Microwave Regime, *Phys. Rev. Lett.*, *107*, 073601.

[104] **Yanik, M.F.**, **Fan, S.**, **Soljačić, M. and Joannopoulos, J.D.** (2003). All-optical transistor action with bistable switching in a photonic crystal cross-waveguide geometry, *Opt. Lett.*, *28*(24), 2506–2508.

[105] **Chang, D.E.**, **Sørensen, A.S.**, **Demler, E.A. and Lukin, M.D.** (2007). A single-photon transistor using nanoscale surface plasmons, *Nature physics*, *3*(11), 807–812.

[106] **Zhou, L.**, **Dong, H.**, **Liu, Y.x.**, **Sun, C.P. and Nori, F.** (2008). Quantum supercavity with atomic mirrors, *Phys. Rev. A*, *78*, 063827.

[107] **Zhou, L.**, **Yang, L.P.**, **Li, Y. and Sun, C.P.** (2013). Quantum Routing of Single Photons with a Cyclic Three-Level System, *Phys. Rev. Lett.*, *111*, 103604.

[108] **Rephaeli, E. and Fan, S.** (2012). Stimulated Emission from a Single Excited Atom in a Waveguide, *Phys. Rev. Lett.*, *108*, 143602.

[109] **Martín-Cano, D.**, **González-Tudela, A.**, **Martín-Moreno, L.**, **García-Vidal, F.J.**, **Tejedor, C. and Moreno, E.** (2011). Dissipation-driven generation of two-qubit entanglement mediated by plasmonic waveguides, *Phys. Rev. B*, *84*, 235306.

[110] **Romero, G.**, **García-Ripoll, J.J. and Solano, E.** (2009). Microwave Photon Detector in Circuit QED, *Phys. Rev. Lett.*, *102*, 173602.

[111] **Jaynes, E.T. and Cummings, F.W.** (1963). Comparison of quantum and semiclassical radiation theories with application to the beam maser, *Proceedings of the IEEE*, *51*(1), 89–109.

[112] **Kosloff, R. and Kosloff, D.** (1986). Absorbing boundaries for wave propagation problems, *Journal of Computational Physics*, *63*(2), 363–376.

[113] **González-Tudela, A. and Cirac, J.I.** (2017). Markovian and non-Markovian dynamics of quantum emitters coupled to two-dimensional structured reservoirs, *Physical Review A*, *96*(4), 043811.

[114] **Pascazio, S.** (2014). All you ever wanted to know about the quantum Zeno effect in 70 minutes, *Open Systems & Information Dynamics*, *21*(01n02), 1440007.

[115] **Nakazato, H.**, **Namiki, M. and Pascazio, S.** (1996). Temporal behavior of quantum mechanical systems, *International Journal of Modern Physics B*, *10*(03), 247–295.

[116] **Facchi, P. and Pascazio, S.** (2001). *Progress in Optics*, volume 42, Elsevier: Amsterdam.

[117] **Facchi, P. and Pascazio, S.** (2008). Quantum Zeno dynamics: mathematical and physical aspects, *Journal of Physics A: Mathematical and Theoretical*, *41*(49), 493001.

[118] **Xu, D. and Cao, J.** (2016). Non-canonical distribution and non-equilibrium transport beyond weak system-bath coupling regime: A polaron transformation approach, *Frontiers of Physics*, *11*(4), 110308.

[119] **Devreese, J.T.** (1996). Polarons, *Encycl. Appl. Phys.*, *14*(cond-mat/0004497), 383–409.

[120] **Lee, T.D.**, **Low, F.E. and Pines, D.** (1953). The Motion of Slow Electrons in a Polar Crystal, *Phys. Rev.*, *90*, 297–302.

[121] **Shi, T.**, **Demler, E. and Cirac, J.I.** (2018). Variational study of fermionic and bosonic systems with non-Gaussian states: Theory and applications, *Annals of Physics*, *390*, 245–302.

[122] **Gerry, C.**, **Knight, P. and Knight, P.L.** (2005). *Introductory quantum optics*, Cambridge university press.

[123] **Nazir, A.**, **McCutcheon, D.P. and Chin, A.W.** (2012). Ground state and dynamics of the biased dissipative two-state system: Beyond variational polaron theory, *Physical Review B*, *85*(22), 224301.

[124] **Díaz-Camacho, G.**, **Bermudez, A. and García-Ripoll, J.J.** (2016). Dynamical polaron Ansatz: A theoretical tool for the ultrastrong-coupling regime of circuit QED, *Physical Review A*, *93*(4), 043843.

[125] **Shi, T.**, **Chang, Y. and García-Ripoll, J.J.** (2018). Ultrastrong Coupling Few-Photon Scattering Theory, *Phys. Rev. Lett.*, *120*, 153602.

[126] **Rivas, A.**, **Huelga, S.F. and Plenio, M.B.** (2014). Quantum non-Markovianity: characterization, quantification and detection, *Rep. Prog. Phys.*, *77*(9), 094001.

[127] **Breuer, H.P.**, **Laine, E.M.**, **Piilo, J. and Vacchini, B.** (2016). Colloquium: Non-Markovian dynamics in open quantum systems, *Rev. Mod. Phys.*, *88*, 021002.

[128] **Fanchini, F.F.**, **Karpat, G.**, **Çakmak, B.**, **Castelano, L.K.**, **Aguilar, G.H.**, **Farías, O. J... de Oliveira, M.C.** (2014). Non-Markovianity through Accessible Information, *Phys. Rev. Lett.*, *112*, 210402.

[129] **Lu, X.M.**, **Wang, X. and Sun, C.P.** (2010). Quantum Fisher information flow and non-Markovian processes of open systems, *Phys. Rev. A*, *82*, 042103.

[130] **Luo, S.**, **Fu, S. and Song, H.** (2012). Quantifying non-Markovianity via correlations, *Phys. Rev. A*, *86*, 044101.

[131] **Rivas, A.**, **Huelga, S.F. and Plenio, M.B.** (2010). Entanglement and Non-Markovianity of Quantum Evolutions, *Phys. Rev. Lett.*, *105*, 050403.

[132] **Breuer, H.P.**, **Laine, E.M. and Piilo, J.** (2009). Measure for the Degree of Non-Markovian Behavior of Quantum Processes in Open Systems, *Phys. Rev. Lett.*, *103*, 210401.

[133] **Lorenzo, S.**, **Lombardo, F.**, **Ciccarello, F. and Palma, G.M.** (2017). Quantum non-Markovianity induced by Anderson localization, *Scientific reports*, *7*, 42729.

[134] **Cosco, F. and Maniscalco, S.** (2018). Memory effects in a quasiperiodic Fermi lattice, *Physical Review A*, *98*(5), 053608.

[135] **Cosco, F.**, **Borrelli, M.**, **Mendoza-Arenas, J.J.**, **Plastina, F.**, **Jaksch, D. and Maniscalco, S.** (2018). Bose-Hubbard lattice as a controllable environment for open quantum systems, *Physical Review A*, *97*(4), 040101.

[136] **Hinarejos, M.**, **Di Franco, C.**, **Romanelli, A. and Pérez, A.** (2014). Chirality asymptotic behavior and non-Markovianity in quantum walks on a line, *Phys. Rev. A*, *89*, 052330.

[137] **Kumar, N.P.**, **Banerjee, S. and Chandrashekar, C.** (2018). Enhanced non-Markovian behavior in quantum walks with Markovian disorder, *Sci. Rep.*, *8*(1), 8801.

[138] **Ahlbrecht, A.**, **Vogts, H.**, **Werner, A.H. and Werner, R.F.** (2011). Asymptotic evolution of quantum walks with random coin, *J. Math. Phys.*, *52*(4), 042201.

[139] **Ahlbrecht, A.**, **Scholz, V.B. and Werner, A.H.** (2011). Disordered quantum walks in one lattice dimension, *J. Math. Phys.*, *52*(10), 102201.

[140] **Hamza, E.**, **Joye, A. and Stolz, G.** (2009). Dynamical localization for unitary Anderson models, *Mathematical Physics, Analysis and Geometry*, *12*(4), 381.

[141] **Wójcik, A.**, **Łuczak, T.**, **Kurzyński, P.**, **Grudka, A.**, **Gdala, T. and Bednarska-Bzdęga, M.** (2012). Trapping a particle of a quantum walk on the line, *Phys. Rev. A*, *85*(1), 012329.

[142] **Danacı, B.**, **Karpat, G.**, **Yalçınkaya, İ. and Subaşı, A.** (2019). Non-Markovianity and bound states in quantum walks with a phase impurity, *Journal of Physics A: Mathematical and Theoretical*, *52*(22), 225302.

[143] **Törmä, P.**, **Jex, I. and Schleich, W.P.** (2002). Localization and diffusion in Ising-type quantum networks, *Phys. Rev. A*, *65*, 052110.

[144] **Mackay, T.D.**, **Bartlett, S.D.**, **Stephenson, L.T. and Sanders, B.C.** (2002). Quantum walks in higher dimensions, *Journal of Physics A: Mathematical and General*, *35*(12), 2745–2753.

[145] **Brun, T.A.**, **Carteret, H.A. and Ambainis, A.** (2003). Quantum random walks with decoherent coins, *Phys. Rev. A*, *67*, 032304.

[146] **Brun, T.A.**, **Carteret, H.A. and Ambainis, A.** (2003). Quantum to Classical Transition for Random Walks, *Phys. Rev. Lett.*, *91*, 130602.

[147] **Annabestani, M.**, **Akhtarshenas, S.J. and Abolhassani, M.R.** (2010). Decoherence in a one-dimensional quantum walk, *Phys. Rev. A*, *81*, 032321.

[148] **Romanelli, A.**, **Siri, R.**, **Abal, G.**, **Auyuanet, A. and Donangelo, R.** (2005). Decoherence in the quantum walk on the line, *Physica A*, *347*, 137 – 152.

[149] **Singh, S. and Chandrashekar, C.M.** (2020). Quantum interference and coherence in one-dimensional disordered and localized quantum walk, *arXiv preprint arXiv:1711.06217v3*.

[150] **Chandrashekar, C.M.**, **Srikanth, R. and Banerjee, S.** (2007). Symmetries and noise in quantum walk, *Phys. Rev. A*, *76*, 022316.

[151] **Yin, Y.**, **Katsanos, D.E. and Evangelou, S.N.** (2008). Quantum walks on a random environment, *Phys. Rev. A*, *77*, 022302.

[152] **Chandrashekar, C.M.** (2011). Disordered-quantum-walk-induced localization of a Bose-Einstein condensate, *Phys. Rev. A*, *83*, 022320.

[153] **Chandrashekar, C.** (2012). Disorder induced localization and enhancement of entanglement in one- and two-dimensional quantum walks, *arXiv preprint arXiv:1212.5984*.

[154] **Schreiber, A.**, **Cassemiro, K.N.**, **Potoček, V.**, **Gábris, A.**, **Jex, I. and Silberhorn, C.** (2011). Decoherence and Disorder in Quantum Walks: From Ballistic Spread to Localization, *Phys. Rev. Lett.*, *106*, 180403.

[155] **Prokof'ev, N. and Stamp, P.** (2006). Decoherence and quantum walks: Anomalous diffusion and ballistic tails, *Physical Review A*, *74*(2), 020102.

[156] **Carlström, J.**, **Prokof'ev, N. and Svistunov, B.** (2016). Quantum Walk in Degenerate Spin Environments, *Phys. Rev. Lett.*, *116*, 247202.

[157] **Tregenna, B.**, **Flanagan, W.**, **Maile, R. and Kendon, V.** (2003). Controlling discrete quantum walks: coins and initial states, *New J. Phys.*, *5*, 83–83.

[158] **Asbóth, J.K.** (2012). Symmetries, topological phases, and bound states in the one-dimensional quantum walk, *Phys. Rev. B*, *86*(19), 195414.

[159] **Zhao, Q. and Gong, J.** (2015). From disordered quantum walk to physics of off-diagonal disorder, *Phys. Rev. B*, *92*(21), 214205.

[160] **Luoma, K. and Piilo, J.** (2016). Discrete dynamics and non-Markovianity, *J. Phys. B*, *49*(12), 125501.

[161] **Wißmann, S.**, **Karlsson, A.**, **Laine, E.M.**, **Piilo, J. and Breuer, H.P.** (2012). Optimal state pairs for non-Markovian quantum dynamics, *Phys. Rev. A*, *86*, 062108.

[162] **Wootters, W.K.** (1998). Entanglement of Formation of an Arbitrary State of Two Qubits, *Phys. Rev. Lett.*, *80*, 2245–2248.

[163] **Neto, A.C.**, **Karpat, G. and Fanchini, F.F.** (2016). Inequivalence of correlation-based measures of non-Markovianity, *Phys. Rev. A*, *94*, 032105.

[164] **Nitsche, T.**, **Barkhofen, S.**, **Kruse, R.**, **Sansoni, L.**, **Štefaňák, M.**, **Gábris, A... Silberhorn, C.** (2018). Probing measurement-induced effects in quantum walks via recurrence, *Sci. Adv.*, *4*, 6.

[165] **Nitsche, T.**, **Elster, F.**, **Novotný, J.**, **Gábris, A.**, **Jex, I.**, **Barkhofen, S. and Silberhorn, C.** (2016). Quantum walks with dynamical control: graph engineering, initial state preparation and state transfer, *New J. Phys.*, *18*(6), 063017.

[166] **Anderson, P.W.** (1958). Absence of Diffusion in Certain Random Lattices, *Phys. Rev.*, *109*, 1492–1505.

[167] **Altman, E. and Vosk, R.** (2015). Universal Dynamics and Renormalization in Many-Body-Localized Systems, *Annual Review of Condensed Matter Physics*, *6*(1), 383–409.

[168] **Nandkishore, R. and Huse, D.A.** (2015). Many-Body Localization and Thermalization in Quantum Statistical Mechanics, *Annual Review of Condensed Matter Physics*, *6*(1), 15–38.

[169] **Abanin, D.A. and Papić, Z.** (2017). Recent progress in many-body localization, *Annalen der Physik*, *529*(7), 1700169.

[170] **Alet, F. and Laflorencie, N.** (2018). Many-body localization: An introduction and selected topics, *Comptes Rendus Physique*, *19*(6), 498–525.

[171] **Abanin, D.A.**, **Altman, E.**, **Bloch, I. and Serbyn, M.** (2019). Colloquium: Many-body localization, thermalization, and entanglement, *Rev. Mod. Phys.*, *91*, 021001.

[172] **Deutsch, J.M.** (2018). Eigenstate thermalization hypothesis, *Reports on Progress in Physics*, *81*(8), 082001.

[173] **Grover, T. and Fisher, M.P.A.** (2014). Quantum disentangled liquids, *Journal of Statistical Mechanics: Theory and Experiment*, *2014*(10), P10010.

[174] **Smith, A.**, **Knolle, J.**, **Moessner, R. and Kovrizhin, D.L.** (2017). Absence of Ergodicity without Quenched Disorder: From Quantum Disentangled Liquids to Many-Body Localization, *Phys. Rev. Lett.*, *119*, 176601.

[175] **Smith, A.**, **Knolle, J.**, **Kovrizhin, D.L. and Moessner, R.** (2017). Disorder-free localization, *Physical review letters*, *118*(26), 266601.

[176] **Yang, W.W.**, **Zhang, L.**, **Guo, X.M. and Zhong, Y.** (2020). Hidden Anderson Localization in Disorder-Free Ising-Kondo Lattice, *Chinese Physics B*.

[177] **Carneiro, I.**, **Loo, M.**, **Xu, X.**, **Girerd, M.**, **Kendon, V. and Knight, P.L.** (2005). Entanglement in coined quantum walks on regular graphs, *New J. Phys.*, *7*(1), 156.

[178] **Abal, G.**, **Siri, R.**, **Romanelli, A. and Donangelo, R.** (2006). Quantum walk on the line: Entanglement and nonlocal initial conditions, *Phys. Rev. A*, *73*, 042302.

[179] **Camilleri, E.**, **Rohde, P.P. and Twamley, J.** (2014). Quantum walks with tuneable self-avoidance in one dimension, *Scientific reports*, *4*(1), 1–7.

[180] **Verga, A.D.** (2019). Interacting quantum walk on a graph, *Phys. Rev. E*, *99*, 012127.

[181] **Sellapillay, K. and Verga, A.D.** (2020). Quantum walk on a graph of spins: magnetism and entanglement, *arXiv preprint arXiv:2006.14883*.

[182] **Paredes, B.**, **Verstraete, F. and Cirac, J.I.** (2005). Exploiting quantum parallelism to simulate quantum random many-body systems, *Phys. Rev. Lett.*, *95*(14), 140501.

[183] **Joye, A. and Merkli, M.** (2010). Dynamical localization of quantum walks in random environments, *J. Stat. Phys.*, *140*(6), 1025–1053.

[184] **De Nicola, F.**, **Sansoni, L.**, **Crespi, A.**, **Ramponi, R.**, **Osellame, R.**, **Giovannetti, V... Sciarrino, F.** (2014). Quantum simulation of bosonic-fermionic noninteracting particles in disordered systems via a quantum walk, *Phys. Rev. A*, *89*, 032322.

[185] **Pankov, A.V.**, **Vatnik, I.D.**, **Churkin, D.V. and Derevyanko, S.A.** (2019). Anderson localization in synthetic photonic lattice with random coupling, *Optics express*, *27*(4), 4424–4434.

[186] **Crespi, A.**, **Osellame, R.**, **Ramponi, R.**, **Giovannetti, V.**, **Fazio, R.**, **Sansoni, L... Mataloni, P.** (2013). Anderson localization of entangled photons in an integrated quantum walk, *Nature Photonics*, *7*(4), 322–328.

[187] **Semeghini, G.**, **Landini, M.**, **Castilho, P.**, **Roy, S.**, **Spagnolli, G.**, **Trenkwalder, A.**, **Fattori, M.**, **Inguscio, M. and Modugno, G.** (2015). Measurement of the mobility edge for 3D Anderson localization, *Nature Physics*, *11*(7), 554–559.

[188] **Bordia, P.**, **Lüschen, H.**, **Schneider, U.**, **Knap, M. and Bloch, I.** (2017). Periodically driving a many-body localized quantum system, *Nature Physics*, *13*(5), 460–464.

[189] **Lenarčič, Z.**, **Altman, E. and Rosch, A.** (2018). Activating many-body localization in solids by driving with light, *Physical Review Letters*, *121*(26), 267603.

[190] **Ray, S.**, **Sinha, S. and Sengupta, K.** (2018). Signature of chaos and delocalization in a periodically driven many-body system: An out-of-time-order-correlation study, *Physical Review A*, *98*(5).

[191] **Ray, S.**, **Ghosh, A. and Sinha, S.** (2018). Drive-induced delocalization in the Aubry-André model, *Physical Review E*, *97*(1).

[192] **Berges, J.**, **Borsányi, S. and Wetterich, C.** (2004). Prethermalization, *Phys. Rev. Lett.*, *93*(14), 142002.

[193] **Gring, M.**, **Kuhnert, M.**, **Langen, T.**, **Kitagawa, T.**, **Rauer, B.**, **Schreitl, M... Schmiedmayer, J.** (2012). Relaxation and Prethermalization in an Isolated Quantum System, *Science*, *337*(6100), 1318–1322.

[194] **Kollar, M.**, **Wolf, F.A. and Eckstein, M.** (2011). Generalized Gibbs Ensemble Prediction of Prethermalization Plateaus and Their Relation to Nonthermal Steady States in Integrable Systems, *Phys. Rev. B*, *84*(5), 054304.

[195] **Mallayya, K.**, **Rigol, M. and De Roeck, W.** (2019). Prethermalization and Thermalization in Isolated Quantum Systems, *Phys. Rev. X*, *9*(2), 021027, 1810.12320.

[196] **Mori, T.**, **Ikeda, T.N.**, **Kaminishi, E. and Ueda, M.** (2018). Thermalization and Prethermalization in Isolated Quantum Systems: A Theoretical Overview, *J. Phys. B: At. Mol. Opt. Phys.*, *51*(11), 112001, 1712.08790.

[197] **Elster, F.**, **Barkhofen, S.**, **Nitsche, T.**, **Novotný, J.**, **Gábris, A.**, **Jex, I. and Silberhorn, C.** (2015). Quantum Walk Coherences on a Dynamical Percolation Graph, *Sci. Rep.*, *5*, 13495.

[198] **Kendon, V.** (2007). Decoherence in quantum walks–a review, *Math. Struct. Comp. Sci.*, *17*(6), 1169–1220.

CURRICULUM VITAE

Name Surname: Burçin Danacı

EDUCATION:

- **B.Sc.:** February 2012, İstanbul Technical University, Faculty of Science and Letters, Department of Physics Engineering
- **M.Sc.:** June 2014, İstanbul Technical University, Faculty of Science and Letters, Department of Physics Engineering
- **PhD:** February 2021, İstanbul Technical University, Faculty of Science and Letters, Department of Physics Engineering

PROFESSIONAL EXPERIENCE AND REWARDS:

- 2013 - 2020 Research and Teaching Assistant in Department of Physics Engineering, İstanbul Technical University.
- 2018 - 2019 The Scientific and Technological Research Council of Turkey (TUBITAK) 2214A Program, Consejo Superior de Investigaciones Científicas, Madrid, Spain, Quantum Information and Foundations Group

PUBLICATIONS AND PRESENTATIONS ON THE THESIS:

- **Danacı, B.**, Yalçınkaya, I., Çakmak, B., Karpat, G., Kelly, S. P., Subaşı, A. L., 2021. Disorder-free localization in quantum walks. *Physical Review A*, 103(2), 022416.
- **Danacı, B.**, Karpat, G., Yalçınkaya, İ., Subaşı, A. L., 2019. Non-Markovianity and bound states in quantum walks with a phase impurity, *Journal of Physics A: Mathematical and Theoretical*, 52.22, 225302.
- **Danacı, B.**, Karpat, G., Yalçınkaya, İ. and Subaşı, A. L. (2018) "The effects of localized bound states on non-Markovianity of a quantum walk with a phase impurity" 25. İstatistik Fizik Günleri, Izmir Institute of Technology, Turkey
- **Danacı, B.**, and Subaşı, A. L. (2017) "Comparison of non-Markovianity measures in a quantum walk coupled to memory qubits" Workshop on Quantum Science and Quantum Technologies, ICTP, Trieste, Italy
- **Danacı, B.**, and Subaşı, A. L. (2017). "Scattering of a quantum walker from a chaın of memory qubits." Joint IMPRS Workshop on Condensed Matter, Quantum Technology and Quantum Materials, Max Planck Institute for the Physics of Complex Systems, Germany

- **Danacı, B.**, and Subaşı, A. L. (2017). "Spread and Localization Properties of a One-Dimensional Quantum Walk with Memory." KOBIT 1 - Kuantum Optiği ve Bilisim Toplantısı, Izmir Institute of Technology, Turkey

- **Danacı, B.**, and Subaşı, A. L. (2016). "Spread and Entanglement in a One-Dimensional Self-Avoiding Quantum Walk." Workshop of Quantum Simulation and Quantum Walks, Faculty of Nuclear Sciences and Physical Engineering Czech Technical University in Prague, Czech Rebpublic

- **Danacı, B.**, and Subaşı, A. L. (2015). "Few Photon Dynamics in Coupled Cavity Arrays." Workshop on Photonics : Fundamentals Applications, ICTP – Eurasian Centre for Advanced Research (ICTP-ECAR), İzmir, Turkey

OTHER PUBLICATIONS AND PRESENTATIONS:

- **Danacı, B.**, Erzan, A., 2016. Metanetworks of artificially evolved regulatory networks, *Journal of Statistical Mechanics: Theory and Experiment*, 2016.4, 043501.

- **Danacı, B.**, Anıl, M. A., Erzan, A., 2014. Motif statistics of artificially evolved and biological networks. *Physical Review E*, 89(6), 062719.

- **Danacı, B.**, Anıl, M.A. and Erzan, A. (2014) "From dynamics to topology on regulatory Boolean networks " XXXIV Dynamics Days Europe , University of Bayreuth, Germany

- **Danacı, B.**, and Erzan, A. (2014) "Metanetworks of artificially evolved regulatory networks" International Conference on Mathematical Modeling in Physical Sciences, Madrid, Spain

- **Danacı, B.**, and Erzan, A. (2014). "Model Regulatory Networks Form Metanetworks in Genotype and Phenotype Spaces." Conference of the Middle European Cooperation in Statistical Pysics, Coventry, England

- **Danacı, B.**, Anıl, M.A. and Erzan, A. (2013). "Motif Statistics Of Artificially Evolved And Biological Networks." European Conferance on Complex Systems, Barcelona, Spain

- Anıl, M.A. **Danacı, B.**, and Erzan, A. (2012). "Motif Statistics and Dynamics on Boolean Networks." Third International Workshop on Statistical Mechanics and Dynamical Systems, Institute of Theoretical and Applied Physics, Turunc/Marmaris, Turkey

- Hundur, Y., **Danacı, B.**, 2012. Thermal effects on nickel. In *AIP Conference Proceedings* (Vol. 1479, No. 1, pp. 1814-1816). American Institute of Physics.